

# 修士学位論文

Development of tunable single particle  
detection system for an improved measurement of  
proton-to-antiproton charge-to-mass ratio

(陽子-反陽子質量電荷比の測定精度向上のための  
単一粒子検出システム開発)

平成 28 年度

広域科学専攻 相関基礎科学系

学籍番号 31-156928

田中陶冶



# Abstract

The Baryon Antibaryon Symmetry Experiment (BASE) collaboration aims to perform stringent tests of the combined charge, parity and time reversal symmetry (CPT symmetry) by comparing the fundamental properties of protons and antiprotons, such as charge-to-mass ratios and magnetic moments, with high precision. To realize such measurements, an advanced Penning trap system is used. This enables us trapping of single protons and antiprotons in a stable potential. Moreover, highly-sensitive superconducting detection systems allow to measure image currents on the order of fA, which is induced by an oscillation of the single trapped particle. By using these developed devices, the BASE collaboration achieved the most precise measurement of the proton  $g$ -factor with a relative precision of 3.3 parts per billion (p.p.b.) [25] and a comparison of the proton-to-antiproton charge-to-mass ratio with 69 parts per trillion (p.p.t.) [13]. In order to achieve an even higher precision for the charge-to-mass ratio measurement, it requires a development which contributes to the reduction of systematic uncertainties. In this thesis, the development of a tunable single particle axial detection system is presented. By this development, it is expected that the systematic uncertainties arose from our previous charge-to-mass ratio measurement will be reduced significantly, as a consequence increases the final precision.

# Table of contents

<b>Chapter 1</b>	<b>Introduction</b>	<b>1</b>
1.1	Background of testing CPT symmetry . . . . .	1
1.2	Outline of this thesis . . . . .	4
<b>Chapter 2</b>	<b>Experimental method</b>	<b>5</b>
2.1	Penning trap . . . . .	6
2.2	The Penning trap potential in ideal geometry . . . . .	8
2.3	Image current detection . . . . .	11
<b>Chapter 3</b>	<b>Experimental setup of BASE</b>	<b>20</b>
3.1	AD beamline . . . . .	20
3.2	Overview of the BASE apparatus . . . . .	21
3.3	The Penning trap assembly . . . . .	22
<b>Chapter 4</b>	<b>Axial frequency tuning</b>	<b>25</b>
4.1	Concept of the charge-to-mass ratio measurement . . . . .	25
4.2	Tunable axial detection system . . . . .	31
<b>Chapter 5</b>	<b>The principles of the axial detection system</b>	<b>34</b>
5.1	Resonator . . . . .	34
5.2	Amplifier . . . . .	38
5.3	Varactor system . . . . .	44
<b>Chapter 6</b>	<b>Evaluation of the tunable axial detection system</b>	<b>47</b>
6.1	Setup for the cryogenic test . . . . .	47
6.2	Resonator test . . . . .	48
6.3	Varactor test . . . . .	53
6.4	Amplifier test . . . . .	59

---

6.5	Test of the the axial detection system . . . . .	66
<b>Chapter 7</b>	<b>Conclusions and overview</b>	<b>74</b>
<b>Bibliography</b>		<b>76</b>

# List of figure

1.1	Measurement status of the CPT symmetry test . . . . .	3
2.1	Cut veiw of the cylindrical Penning trap . . . . .	6
2.2	Cyclotron frequency in the Penning trap . . . . .	7
2.3	The trap potential by the five electrodes . . . . .	10
2.4	Image current detection system . . . . .	11
2.5	Equivalent circuit of the trapped particle of the detection system . . . . .	13
2.6	Dip of the antiproton axial frequency by the detection system . . . . .	14
2.7	Schematic of the sideband coupling method in the Penning trap . . . . .	15
2.8	Schematic of the magnetic bottle . . . . .	17
2.9	Illustration of the continuous Stern-Gerlach effect . . . . .	18
3.1	Top view of Antimatter Decelerator facility . . . . .	20
3.2	Overview of the BASE experimental zone . . . . .	21
3.3	Penning trap assembly at BASE . . . . .	22
3.4	3D model and the picture of the Penning trap assembly . . . . .	24
4.1	Penning trap setup for the charge-to-mass ratio . . . . .	26
4.2	Measurement cycle of the charge-to-mass ratio measurement . . . . .	27
4.3	The geometry of the cylindrical trap . . . . .	28
4.4	Trap potential difference of antiproton and $H^-$ ion . . . . .	30
4.5	Tunable axial detection system . . . . .	32
4.6	The principle of the varactor . . . . .	32
5.1	Scematic of the trap can . . . . .	35
5.2	Schematic of the amplifier . . . . .	36
5.3	Equivalent circuit of the resonator . . . . .	37

5.4	The schematic of dual-gate FET . . . . .	39
5.5	The schematic of dual-gate FET with disconnected and shorted gates. . . . .	40
5.6	Schematic of common-source circuit and source-follower circuit . . . . .	40
5.7	Source-follower circuit with a signal applied to the output . . . . .	42
5.8	Circuit board of the amplifier . . . . .	43
5.9	Equivalent circuit of the resonator with the amplifier . . . . .	44
5.10	Varactor circuit board . . . . .	45
5.11	Circuit of the tunable axial detection system . . . . .	45
6.1	Picture of the cryogenic test setup . . . . .	48
6.2	Test setup for the resonator . . . . .	49
6.3	Equivalent circuit of the resonator test . . . . .	51
6.4	The principle of the $Q$ -value increasing by installing the dummy trap . . . . .	52
6.5	The varactor testing system . . . . .	53
6.6	Resonance frequency shift by the varactor . . . . .	54
6.7	Effective parallel resistance shift by the varactor circuit . . . . .	56
6.8	Resonance frequency shift by the varactor tested with the dummy trap . . . . .	58
6.9	$Q$ -value and the effective parallel resistance shift by the varactor tested with the resonator and the dummy trap . . . . .	59
6.10	Schematic of disconnected and shorted dual-gate FET circuit . . . . .	60
6.11	Gain test of the amplifier . . . . .	61
6.12	Equivalent input noise test setup of the amplifier . . . . .	62
6.13	Equivalent input noise measurement results of the NE25139 and 3SK164 amplifier .	63
6.14	Noise spectral power density and the noise fitting of the NE25139 and 3SK164 amplifier . . . . .	65
6.15	Circuit of the tunable axial detection system . . . . .	66
6.16	Signal-to-noise ratio measurement setup of the detection system . . . . .	67
6.17	Resonance shift by adjusting the gate voltage of the amplifier . . . . .	68
6.18	The $Q$ -value and the effective parallel resistance results of the amplifier test in the axial detection system . . . . .	69
6.19	Equivalent input noise of the amplifier as a function of gate voltage . . . . .	70
6.20	Resonance shift by adjusting the gate voltage of the amplifier . . . . .	70
6.21	Resonance frequency shift by the varactor tuning at the axial detection system . .	72
6.22	$Q$ -value and the effective parallel resistance shift by the varactor tested with the resonator and the dummy trap . . . . .	73

# List of table

6.1	Resonance test of the resonator . . . . .	50
6.2	Test of the resonator with dummy trap . . . . .	51
6.3	Resonance shift results of varactor testing . . . . .	55
6.4	results of varactor testing . . . . .	57
6.5	Parameter of the adjustment voltage for the amplifier . . . . .	60
6.6	The optimum gain of the amplifiers . . . . .	61
6.7	Results of Gain and equivalent input noise measurement of NE25139 and 3SK164 amplifier . . . . .	63
6.8	The fitting results of the equivalent input noise measurement . . . . .	65
6.9	Tuning parameter for the amplifier for the whole setup . . . . .	66

# Chapter 1

## Introduction

Antimatter, a pair of the matter with identical mass and lifetime but reversed charge and magnetic moment, has been predicted by P.A.M. Dirac in 1928 [1]. Based on the properties of the relativistic quantum field theory, there is a fundamental symmetry between matters and antimatters under the combination of the charge conjugation (C), parity transformation (P) and time reversal (T), which is called the CPT symmetry. However, according to cosmological observations, matters are dominant in our universe, compared to antimatters [2]. The motivation of the experimentalist is to solve this conflict between particle physics and cosmology by a high precision measurement of the matter's and antimatter's fundamental properties. If any difference in any value is observed, this will be a clear evidence of the CPT violation. On the other hand, if the measurement shows that the values are identical in a certain precision, this information will provide a limitation to the theories which allow the CPT violation. Therefore, a comparison of the matter's and antimatter's fundamental properties by a high precision measurement is necessary to perform a stringent test of the CPT symmetry.

### 1.1 Background of testing CPT symmetry

The status of different CPT tests is shown in Figure 1.1. The highest precision of the CPT test is the mass measurement of kaons by comparing the decay channels of the neutral mesons  $K_0/\bar{K}_0$  to charged and neutral pions. Thereby, the relative mass difference is constrained to be less than  $10^{-18}$  [3] [4]. In the lepton sector, electrons and positrons are measured by using Penning traps with high precision. By applying the continuous Stern-Gerlach effect for the non-destructive detection of single particle spin states in the Penning trap, the  $g$ -factors of the electron and positron are measured with precision better than 4 parts per billion (p.p.b.), and the comparisons of their  $g$ -factors were within  $\delta g/g \sim 2 \times 10^{-12}$  uncertainty [5] [6]. Another CPT test for leptons is the muon

$g - 2$  measurement, which is comparing the  $g - 2$  of  $\mu^+$  and  $\mu^-$  in a storage ring with a fractional precision of  $3.7 \times 10^{-9}$  confirming CPT invariance [7] [8]. However the muon  $g$ -factors deviate by 3.6 standard deviations from the prediction of the Standard Model, which has been interpreted to be caused by coupling to dark gauge bosons [9] [10]. Currently, efforts are in progress to repeat these measurements with higher precision to resolve or confirm this deviation [11] [12].

However, only few tests of CPT symmetry exists in the baryon sector. The most precise CPT test in the baryon sector is the charge-to-mass ratio comparison of protons and antiprotons [13] [14]. The charge-to-mass ratio measurement was performed by the TRAP collaboration at CERN low-energy antiproton ring (LEAR) by comparing the cyclotron frequencies of the proton and the antiproton  $\nu_{c,p}/\nu_{c,\bar{p}}$  [15]. Later, a negatively charged hydrogen ions  $H^-$  were used for the proxy of protons, which allows to increase the relative precision of the cyclotron frequency ratio [14] [16] [17]. Also hydrogen-to-antihydrogen CPT tests are targeted by several collaborations at the antiproton decelerator (AD) [18]. For hydrogen, the 1S-2S transition frequency was measured with a relative uncertainty of  $4.2 \times 10^{-15}$  by using a cold beam of hydrogen atoms [19]. The first measurement of the 1S-2S transition of antihydrogen was recently carried out by the ALPHA collaboration by using the magnetic gradient trap [20]. Another subject to test the CPT symmetry of hydrogen and antihydrogen is the comparison of the ground-state hyperfine-splitting (GS-HFS) of them. The hydrogen GS-HFS has been measured with a fractional precision of 0.7 p.p.t. by using maser [21]. In case of antihydrogen, the ALPHA collaboration observed the hyperfine transition using appearance mode annihilation spectroscopy in a magnetic gradient trap [22]. In parallel, the ASACUSA collaboration reported on the first production of a beam of antihydrogen atoms by using a cusp trap [23].

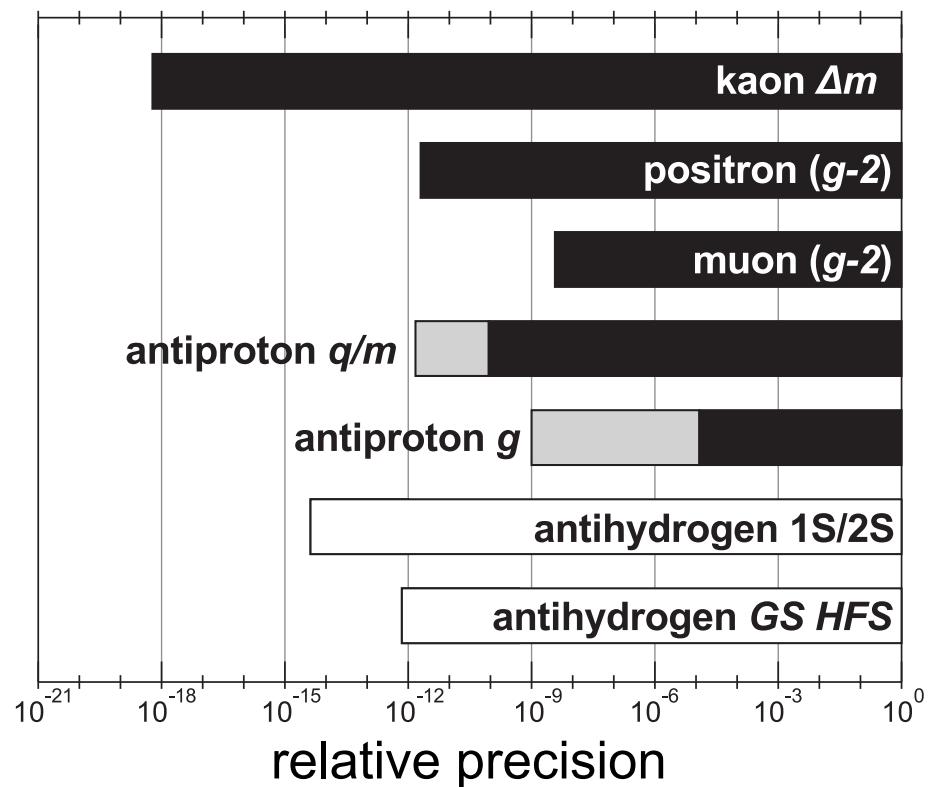


Figure 1.1 The measurement status of the relative precision achieved in different CPT tests. The black part corresponds to the results of the previous measurement, grey part corresponds to the precision which BASE is aiming, and the white part is the precision which is planned for future. The schematic is cited from [26].

The main motivation of the BASE collaboration is to perform a stringent test of CPT symmetry by comparing the fundamental properties of proton and antiproton. Recently we succeeded to measure proton-to-antiproton charge-to-mass ratio in 69 parts per trillion (p.p.t.) agreement [13]. As the cyclotron motion frequency is defined as

$$\nu_c = \frac{1}{2\pi} \frac{q}{m} B \quad (1.1)$$

where  $m$  is the mass,  $q$  is the charge and  $B$  is the magnetic field. The charge-to-mass ratios of the proton-to-antiproton are indirectly extracted by comparing the  $\text{H}^-$  ion and antiproton cyclotron frequencies as

$$\frac{\nu_{c,\bar{p}}}{\nu_{c,\text{H}^-}} = \frac{(q/m)_{\bar{p}}}{(q/m)_{\text{H}^-}}. \quad (1.2)$$

This equation is based on the assumption that the magnetic field is identical. Regarding to the proton  $g$ -factor measurement, we achieved to measure it by using the double Penning-trap technique [24] with an unprecedented precision of 3.3 p.p.b.. [25]. An improved measurement of the antiproton

magnetic moment is in progress. The  $g$ -factor is a dimensionless constant value related to the magnetic moment. The magnetic moment of the proton/antiproton is defined as

$$\mu_{p/\bar{p}} = \pm \frac{g_{p/\bar{p}}}{2} \mu_N, \quad (1.3)$$

where  $\mu_N = q_p \hbar / 2m_p$  is the nuclear magneton. As the Larmor precession frequency of the particle is defined as

$$\nu_L = \frac{g}{2} \frac{1}{2\pi} \frac{q}{m} B. \quad (1.4)$$

From Eq.(1.1) and (1.4), the  $g$ -factor can be expressed as

$$\frac{g}{2} = \frac{\nu_L}{\nu_c}, \quad (1.5)$$

assuming that  $\nu_c$  and  $\nu_L$  are measured at the same magnetic field  $B$ . This principle is the application of previous researches of the electron/positron  $g-2$  measurement [6] [27] [28] to the proton/antiproton. Therefore, the charge-to-mass ratio and the  $g$ -factor can be directly extracted from measurements of two eigenfrequencies.

## 1.2 Outline of this thesis

As the charge-to-mass ratios and the  $g$ -factors are measured by the cyclotron frequency and the Larmor frequency, the final precision is strongly correlated to the precision of the frequency measurements. To realize the high precision eigenfrequency measurement, a stable potential in the Penning trap and highly-sensitive detection systems are necessary. In this thesis, the development of a tunable axial detection system to improve the charge-to-mass ratio measurement is discussed. This new detection system has improved in a way that it has a higher sensitivity, and moreover the resonance frequency is tunable, which allows to measure the charge-to-mass ratio of the  $H^-$  ion and the antiproton in the identical potential.

The outline of my thesis is as follows. In Chapter 2, the principles of the Penning trap and the image current detection are explained. In Chapter 3, the experimental setup of the BASE experiment are explained. In Chapter 4 the details and the problems of the previous charge-to-mass ratio measurement are explained. In Chapter 5 the mechanism about the tunable axial detection system and the optimizations are explained, and in Chapter 6 the evaluation of each part of the tunable axial detection system is discussed. In Chapter 7, a summary of the results is presented.

## Chapter 2

# Experimental method

The BASE collaboration is located at Mainz University, Germany and CERN AD, Switzerland. At Mainz University, the experimental methods to measure  $g$ -factors are developed with protons which are then applied to the antiproton experiment at CERN. Moreover, at CERN we have possibilities to measure the proton-to-antiproton charge-to-mass ratio. To achieve a direct measurement of the proton's and antiproton's fundamental properties with high precision, cryogenic Penning traps are used. This method is suitable for charged and long life time particles such as protons and antiprotons. The Penning trap is composed of a superposition of an electric quadrupole potential and a strong homogeneous magnetic field. Under such a potential configuration, the single charged particles are trapped and the eigenfrequencies of the charged particle can be extracted non-destructively by using superconducting detection systems. By measuring the cyclotron frequency ( $\nu_c$ ) and the Larmor frequency ( $\nu_L$ ), the charge-to-mass ratio and the  $g$ -factor are accessible. To realize the high precision measurement of these frequencies, it is of utmost importance to develop a well designed Penning trap as well as highly-sensitive single particle detection systems are of utmost importance. In the framework of this thesis, the antiproton experiments are focused, which I was participating for my master thesis.

## 2.1 Penning trap

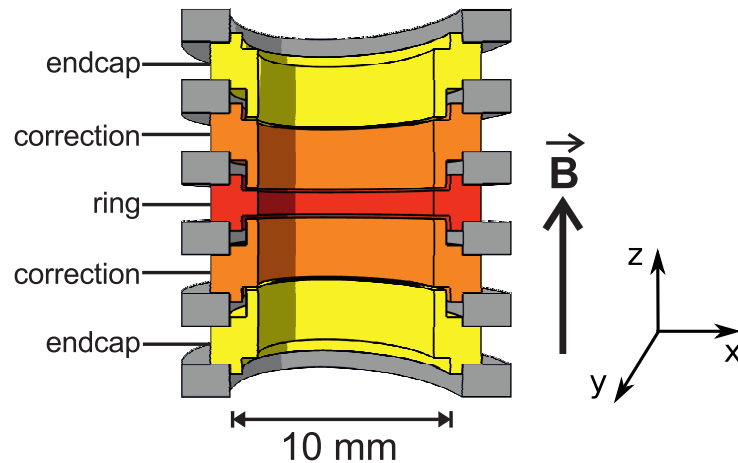


Figure 2.1 The cut view of the cylindrical Penning trap with five electrodes. A ring electrode (red), two correlation electrodes (orange) and two endcap electrodes (yellow) are shown. Each electrodes are spaced by sapphire rings (gray) with an identical inner distance. By adjusting the voltage to each electrodes and adding a strong magnetic field in the axial direction, the particle is trapped in both radial and axial directions. Cited from [26]

The cylindrical Penning trap consists of a central ring electrode, two adjacent correction electrodes and two endcap electrodes. Figure 2.1 shows the cut view of the cylindrical Penning trap. This forms an electric quadrupole potential for confining the charged particle along the axial direction  $z$  (refer to Figure 2.1):

$$\Phi(\rho, z) = V_R C_2 (z^2 - \rho^2/2) \quad (2.1)$$

where  $C_2$  is the potential coefficient. The ring voltage  $V_R$  denotes the potential difference between the ring electrode and the endcap electrode. This hyperbolic electrostatic potential in Eq. (2.1) confines the axial motion of the particle, however the particle is not bounded radially. Therefore, a strong magnetic field  $\vec{B}$  in the axial direction by a superconducting magnet is superimposed to confine the charged particle also in the radial direction. In these field configurations, the charged particle is confined in both radial ( $\rho$ -axis) and axial ( $z$ -axis) position. The trajectory of this trapped particle is described by a superposition of three independent eigenmotions [30] (see Figure 2.2).

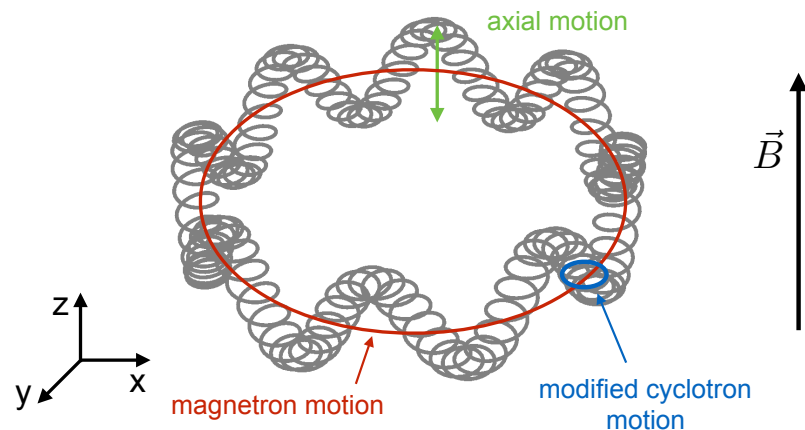


Figure 2.2 The Schematic of the particle's modified motion inside the Penning trap, by the electric quadrupole potential and magnetic field. This motion is the superposition of three eigenmotions, the axial motion (green), the modified cyclotron motion (blue), and the magnetron motion (red). See the text for details.

The axial frequency  $\nu_z$  of the particle is derived from the harmonic oscillation in the hyperbolic potential Eq.(2.1) as

$$\nu_z = \frac{1}{2\pi} \sqrt{2C_2 V_R \frac{q}{m}}. \quad (2.2)$$

In the BASE apparatus, the axial frequency of protons and antiprotons is in the range of 540 kHz to 680 kHz [26]. By the radial component of the electrostatic potential together with the magnetic field  $\vec{B}$ , two additional eigenfrequencies in the radial direction, the modified cyclotron frequency and the magnetron frequency are arose. The modified cyclotron motion is the form of the cyclotron motion being affected by the radial component of the electric quadrupole potential. The magnetron motion is caused by a drift of the cross static field  $\vec{E} \times \vec{B}$ . The respective eigenfrequencies  $\nu_+$  and  $\nu_-$  are given by:

$$\nu_{\pm} = \frac{1}{2}(\nu_c \pm \sqrt{\nu_c^2 - 2\nu_z^2}). \quad (2.3)$$

The magnetron frequency can be expressed as an independent value to the physical properties of the trapped particle by the first order approximation as,

$$\nu_- = \frac{1}{2}(\nu_c - \sqrt{\nu_c^2 - 2\nu_z^2}) \simeq \frac{\nu_z^2}{2\nu_c} = \frac{1}{2\pi} \frac{C_2 V_0}{|\vec{B}|} \quad (2.4)$$

These three eigenfrequencies are related to the the free cyclotron frequency  $\nu_c$  via the invariance theorem [39] as:

$$\nu_c^2 = \nu_+^2 + \nu_-^2 + \nu_z^2. \quad (2.5)$$

Therefore the free cyclotron frequency can be calculated from the high precision measurement of the three eigenfrequencies. One specific property of this important "invariance relation" is, that it is robust with respect to typical first order trap errors. Especially, the theorem is valid for any misalignment or tilt between the magnetic axis. Typical Penning traps used in precision measurement are operated with a hierarchy

$$\nu_+ \gg \nu_z \gg \nu_- . \quad (2.6)$$

In the BASE experiment,  $\nu_+$  is mainly defined by the magnetic field  $B_0 = 1.945$  T and the value is 29.65 MHz and  $\nu_-$  is typically at 7 kHz [26].

## 2.2 The Penning trap potential in ideal geometry

In this section, the Penning trap potential in ideal geometry is explained. The electric quadrupole potential Eq.(2.1) is derived from the Laplace equation  $\nabla^2\Phi = 0$  in cylindrical coordinate system as

$$\nabla^2\Phi(\rho, \varphi, z) = \frac{\partial^2\Phi}{\partial\rho^2} + \frac{1}{\rho} \frac{\partial\Phi}{\partial\rho} + \frac{1}{\rho^2} \frac{\partial^2\Phi}{\partial\varphi^2} + \frac{\partial^2\Phi}{\partial z^2} = 0. \quad (2.7)$$

By the cylindrical geometry, the variable  $\varphi$  vanishes and the partial differential becomes  $\frac{\partial\Phi}{\partial\varphi} = 0$ . The potential can be described by separating the variable using the ansatz  $\Phi(\rho, z) = P(\rho)Z(z)$ . Therefore, Eq.(2.7) becomes

$$\frac{1}{P} \frac{\partial^2 P}{\partial\rho^2} + \frac{1}{\rho P} \frac{\partial P}{\partial\rho} + \frac{1}{Z} \frac{\partial^2 Z}{\partial z^2} = 0. \quad (2.8)$$

As the two endcap electrodes are grounded, this provides the boundary condition of  $Z(0) = Z(\Lambda) = 0$ , where  $\Lambda$  is the trap length. By this,  $Z(z)$  can be described by trigonometric function as

$$Z(z) = A_n \sin k_n z \quad (k_n = \frac{n\pi}{\Lambda}, n \in \mathbb{N}) \quad (2.9)$$

where  $\Lambda$  is the trap length and  $A_n$  is the coefficient. From Eq.(2.9) and defining  $\xi = k_n\rho$ , Eq.(2.8) becomes

$$\xi^2 \frac{\partial^2 P}{\partial\xi^2} + \xi \frac{\partial P}{\partial\xi} - \xi^2 P = 0. \quad (2.10)$$

From this partial differential equation,  $P(\rho)$  can be described by modified Bessel functions of first kind. Combining to Eq.(2.9), the solution of the trap potential is

$$\Phi = \sum_{n=1}^{\infty} I_0(k_n\rho) A_n \sin k_n z \quad (2.11)$$

where  $I_0(k_n\rho)$  is the modified Bessel function of the first kind.

The setup of the Penning trap is as follows.

- Formed by five electrodes - ring electrode at the center, two correction electrodes adjacent to it and two endcap electrode at both ends
- Both endcap electrodes are grounded
- The correction electrode is to tune the harmonicity of the electrostatic potential.
- Each electrodes are spaced by sapphire rings to fix the inner distance of the electrode to  $d = 0.14$  mm

The electrode geometry is carefully selected in orthogonal and compensated design [30]. "Orthogonal" means that the resonance frequency of the particle is independent to the voltage applied to the correction electrode, and "compensated" means that the first higher order corrections  $C_4$  and  $C_6$  of the multipolar potential expansions  $V(0, z) = V_3 \sum_j C_2 j z^{2j}$  can be tuned to zero simultaneously [51]. The details of the design of the BASE-CERN trap stack are described in [37].

By considering the boundary condition of the Penning trap, The coefficient  $A_n$  in Eq.(2.11) can be calculated. First multiply with  $\sin(k_n z)$  to apply the orthogonality of the trigonometric functions as

$$\frac{2}{\Lambda} \int_0^\Lambda dz \sin(k_n z) \sin(k_m z) = \delta_{mn} \quad (2.12)$$

to separate the coefficients of  $\Phi(\rho, z)$ . By applying the boundary condition  $\rho = a$ , where  $a$  is the inner radius of the electrode, the solution of the integration derives  $A_n$  as

$$\begin{aligned} \int_0^\Lambda dz \Phi(a, z) \sin(k_n z) &= \sum_{i=1}^5 \int_{z_{2i-2}}^{z_{2i-1}} dz V_i \sin(k_n z) \\ &+ \sum_{i=1}^4 \int_{z_{2i-1}}^{z_{2i}} dz \left( \frac{V_{i+1} - V_i}{z_{2i} - z_{2i-1}} z + \frac{V_i z_{2i} - V_{i+1} z_{2i-1}}{z_{2i} - z_{2i-1}} \right) \sin(k_n z) \end{aligned} \quad (2.13)$$

where  $V_i$  and  $z_i$  are the voltage and the coordinate shown in the left side of Figure 2.3. The first line is from the boundary condition of the electrode surface and the second line is the linear interpolation of the gaps. From solving this equation, the trap potential is

$$\begin{aligned} \Phi(\rho, z) &= \sum_{n=1}^{\infty} \left[ \frac{V_1 \cos(k_n z_0) - V_5 \cos(k_n z_9)}{d} + \sum_{i=1}^4 \frac{V_{i+1} - V_i}{k_n^2 d} (\sin(k_n z_{2i}) - \sin(k_n z_{2i-1})) \right] \\ &\times \frac{2}{\Lambda} \frac{I_0(k_n \rho)}{I_0(k_n a)} \sin(k_n (z + \frac{\Lambda}{2})) \end{aligned} \quad (2.14)$$

which is shown in the right side of Figure 2.3. Here the distance between each electrodes are  $z_{2i} - z_{2i-1} = d$  and  $z = \frac{\Lambda}{2}$  in the Penning trap is fixed to the the trap center.

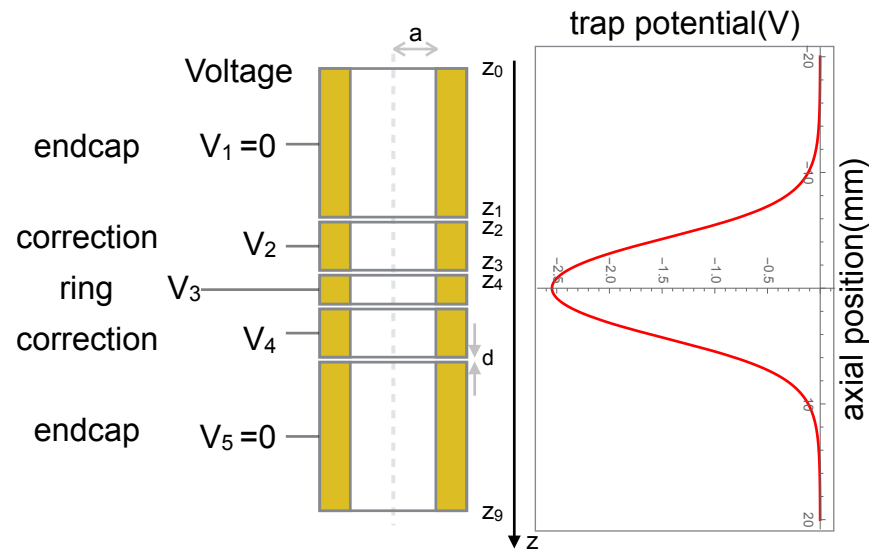


Figure 2.3 The left side is the assembly of the five electrodes of the trap. The graph of the right side is the calculation of the trap potential  $\Phi(\rho, z)$  in ideal Penning trap. Each electrodes are bias in voltage  $V_i$  to stabilize the charged particle to the center of the ring electrode.

To clarify this solution, it is better to expand the trap potential into power-series as

$$\Phi(0, z) = V_3 \sum_{i=0}^m C_i z^i \quad (2.15)$$

where the potential coefficient  $C_i$  is defined as

$$C_i = \sum_{n=0}^{\infty} \left[ \frac{V_1 \cos(k_n z_0) - V_5 \cos(k_n z_9)}{d} + \sum_{i=1}^4 \frac{V_{i+1} - V_i}{k_n^2 d} (\sin(k_n z_{2i}) - \sin(k_n z_{2i-1})) \right] \\ \times \frac{2}{\Lambda V_3} \frac{1}{i! I_0(k_n a)} \left( \frac{n\pi}{\Lambda} \right)^i \sin\left( \frac{n\pi}{2} (n + j) \right). \quad (2.16)$$

Moving back to the setup of the Penning trap, the voltage of the electrode are decided in three values. As the endcap electrode is grounded,  $V_1 = V_5 = 0$ . The correction electrodes has the same voltage and expressed as  $V_2 = V_4 = V_3 \cdot TR$ , where the  $TR$  is called "tuning ratio". All potential coefficients  $C_i$  can be described as  $C_i = E_i + D_i \cdot TR$ . In these units, the criteria "orthogonality" and "compensation" is expressed as  $D_2 = 0$  and  $C_4 = C_6 = 0$ , respectively. Therefore the three free parameters, the tuning ratio ( $TR$ ), the ring electrode length ( $l_3 = z_5 - z_4$ ) and the correction electrode length ( $l_2 = l_4 = z_3 - z_2$ ) define all parameters of the Penning trap potential.

## 2.3 Image current detection

To measure the motional frequencies of the single trapped antiprotons non-destructively, image current detection systems are used [28]. Especially the modified cyclotron frequency  $\nu_+$  and the axial frequency  $\nu_z$  of the single antiproton are directly measured by using highly sensitive superconducting detection systems. The motional frequency is measured from the detection of the image current  $i_p$ , which is induced by the harmonic oscillation of the charged particle. Detection systems are directly connected to the trap electrode to detect and amplify this fA-order image current. The detection system consists of a superconducting resonator and a low noise cryogenic amplifier. Figure 2.4 shows the circuit of the image current detection system. The resonator is equivalent to an inductor  $L$  with a capacitance  $C_p$  and a resistance  $R_p$  connected in parallel.

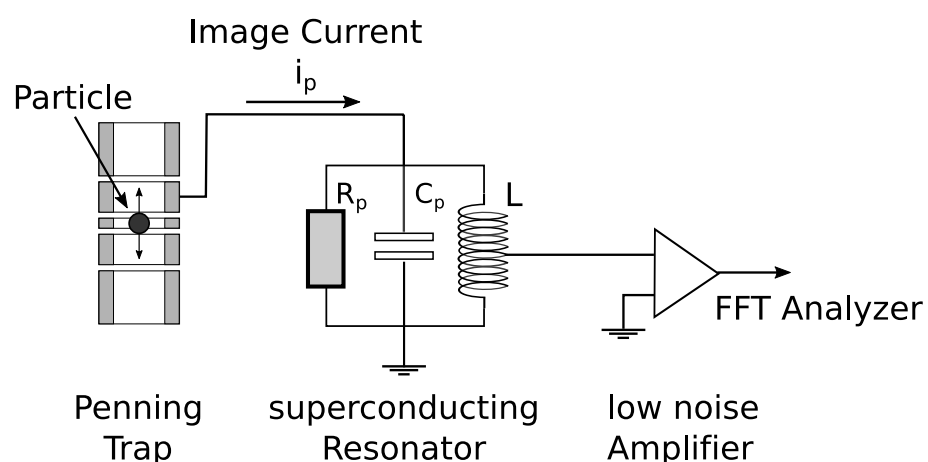


Figure 2.4 The cryogenic image current detection system. The induced image current  $i_p$  which matches to the resonance is amplified at the detection system and is readout by the FFT analyzer.

The two main values to evaluate the resonator are the resonance frequency  $\nu_0$

$$\nu_0 = \frac{1}{2\pi\sqrt{LC_p}} \quad (2.17)$$

and the  $Q$ -value, the dimensionless damping rate of the resonator which is described as,

$$Q = 2\pi \frac{E}{\Delta E} = \frac{\nu_0}{\Delta\nu_0} = \frac{R_p}{2\pi\nu_0 L} \quad (2.18)$$

where  $E$  is the stored energy per cycle,  $\Delta E$  is the energy loss and  $\Delta\nu_0$  is the  $-3$  dB bandwidth compared to the resonance peak, respectively. Eq.(2.17) and Eq.(2.18) can be derived from considering

the total impedance  $Z_p(\omega)$  described as

$$|Z_p(\omega)| = \frac{1}{\sqrt{\frac{1}{R_p^2} + (\frac{1}{\omega L} - \omega C_p)^2}}. \quad (2.19)$$

As the maximum impedance  $Z_p(\omega_0) = R_p$  corresponds to the resonance, the resonance frequency  $\omega_0 = 2\pi\nu_0$  is derived as  $1/\sqrt{LC_p}$ . The impedance of the  $-3$  dB point is

$$|Z_p(\omega)| = \frac{1}{\sqrt{2}} |Z_p(\omega_0)| = \frac{R_p}{\sqrt{2}}. \quad (2.20)$$

From Eq.(2.19) and Eq.(2.20), the  $-3$  dB bandwidth is derived as  $\Delta\nu_0 = 1/C_p R_p$ . Therefore, from the definition of the  $Q$ -value,  $Q = \nu_0/\Delta\nu_0 = R_p/2\pi\nu_0 L$  is derived. From a measurement of the resonance frequency  $\nu_0$  and the  $Q$ -value,  $L$ ,  $C_p$  and  $R_p$  are extracted. This is the main method used for the measurement to evaluate the detection system in Chapter 6.

The induced image current  $i_p$  is described as follows [28]:

$$i_p = \frac{q}{D} \dot{\zeta}_i = 2\pi \frac{q}{D} \nu_i \zeta_i \quad (2.21)$$

where  $\zeta_i$  is the coordinate,  $\nu_i$  is the eigenfrequency of the particle and  $D$  is the trap specific length. When the resonance frequency of the detection system  $\nu_0$  is matched to the particle eigenfrequency  $\nu_i$ , the detection system acts as a simple parallel resistance  $R_p$ . Therefore, a voltage drop occurs as

$$V_p = R_p i_p = 2\pi\nu_0 L Q i_p. \quad (2.22)$$

This voltage drop  $V_p$  is subsequently amplified by the cryogenic amplifier and the transient is recorded by the fast Fourier transform (FFT) analyzer. As the voltage drop is proportional to the parallel resistance, the sensitivity of the image current detection system is defined by the  $Q$ -value. In order to maximize the  $Q$ -value, the detection systems are designed and developed in BASE for each Penning trap [38]. Details of the axial detection system are described in Chapter 5.

### 2.3.1 Dip detection

Together with the trapped particle in the Penning trap, the equivalent circuit of the detection system can be shown in Figure 2.5.

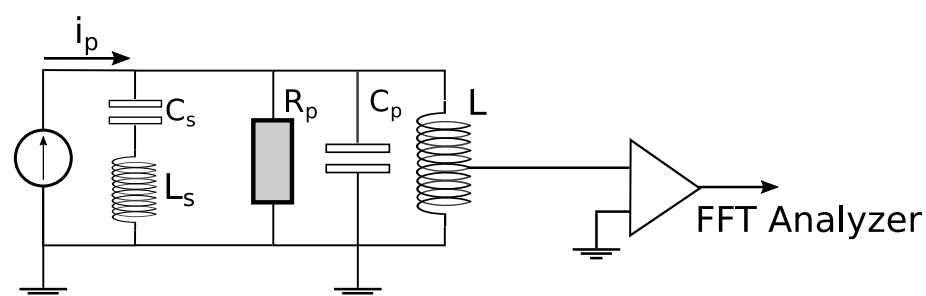


Figure 2.5 The Equivalent circuit of the trapped particle of the detection system. The particle acts as a LC circuit which has a eigenfrequency as a resonance frequency  $\nu_i = 1/(2\pi\sqrt{L_s C_s})$ . The resonance frequency of the detection system is  $\nu_0 = 1/(2\pi\sqrt{L C_p})$ .

The oscillation of the particle can be described as a damped harmonic oscillator. Here, the axial motion is focused only. The equation of the motion is described as

$$m\ddot{z} + m\gamma_z\dot{z} + m\omega_z^2 z = 0 \quad (2.23)$$

where  $\gamma_z$  is the damping constant and  $\omega_z$  is the axial angular frequency. By multiplying  $\dot{z}$  to Eq.(2.23)

$$m\dot{z}\ddot{z} + m\gamma_z\dot{z}^2 + m\omega_z^2 z\dot{z} = 0 \quad (2.24)$$

and time-integrating Eq.(2.24),

$$\frac{1}{2}m\dot{z}^2 + \frac{1}{2}m\omega_z^2 z^2 = - \int m\gamma_z\dot{z}^2 dt = - \int P dt \quad (2.25)$$

is obtained. The left side of the Eq.(2.25) is the total kinetic energy of the particle, while the right side is the dissipation. The power dissipation  $P$  in Eq.(2.25) is due to the image current flow at the parallel resistance as

$$P = R_p i_p^2 = m\gamma_z \dot{z}^2. \quad (2.26)$$

By solving for  $\gamma_z$  and with the definition of the image current in Eq.(2.21), the damping constant is expressed as,

$$\gamma_z = \frac{R_p}{m} \frac{q^2}{D^2}. \quad (2.27)$$

Therefore, the cooling time constant  $\tau_z$  is

$$\tau_z = \frac{1}{\gamma_z} = \frac{m}{R_p} \frac{D^2}{q^2} \quad (2.28)$$

which defines the amount of time required for a particle to dissipate its energy to a fraction  $1/e$  of the initial energy. By combining Eq.(2.23) and Eq.(2.27),

$$m \frac{D^2}{q^2} \frac{d}{dt} i_p + R_p i_p + m \omega_z^2 \int \frac{D^2}{q^2} i_p dt = 0 \quad (2.29)$$

is derived. By introducing the series inductance  $L_s = m \frac{D^2}{q^2}$  and the series capacitance  $C_s = \frac{1}{m \omega_z^2} \frac{q^2}{D^2}$ , Eq.(2.29) is rewritten as

$$L_s q^2 \frac{d}{dt} i_p + R_p i_p + \frac{1}{C_s} \int i_p dt = 0. \quad (2.30)$$

This equation indicates that in the thermal equilibrium, the particle behaves as a series LC circuit with a resonance frequency of  $\nu_z$  (see Figure 2.5). When the axial frequency  $\nu_z = 1/(2\pi\sqrt{L_s C_s})$  is matched to  $\nu_0 = 1/(2\pi\sqrt{L C_p})$ , the series LC circuit acts as a short circuit and the noise is shunted to the ground. Therefore, a dip is observed at the axial frequency  $\nu_z$  of the particle in the noise spectrum [28]. An example of a spectrum is shown in Figure 2.6

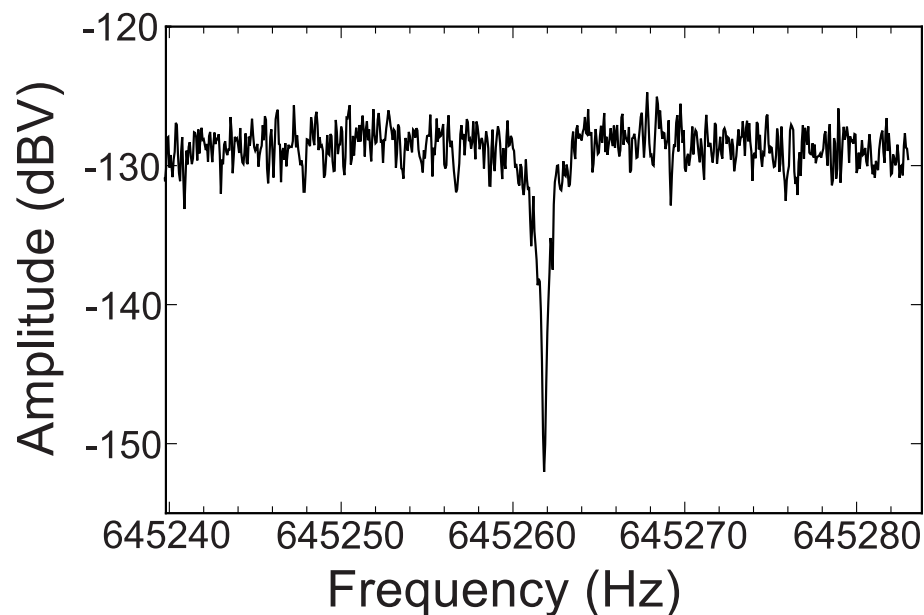


Figure 2.6 The detected dip of the image current signal of the single particle in the BASE Penning trap. In the thermal equilibrium, the particle generates a short at its axial frequency and a dip signal is observed. Cited from [26].

The BASE experiment is using this dip detection to measure the motional frequencies of a single antiproton. The benefit of using the dip detection is that the resonance frequency is measured at thermal amplitudes of about  $10 \mu\text{m}$ , which reduces systematic frequency shifts due to trap imperfections [40]. Moreover the -3 dB dip width can be calculated from the impedance of the

equivalent circuit and this is given as [28]:

$$\Delta\nu_z = \frac{N}{2\pi}\gamma_z = \frac{N}{2\pi}\frac{q^2 R_p}{D^2 m} \quad (2.31)$$

where  $N$  is the number of the trapped particle. From observing the dip width, this provides information on how many particles are actually trapped in a Penning trap.

### 2.3.2 Measurement of the free cyclotron frequency

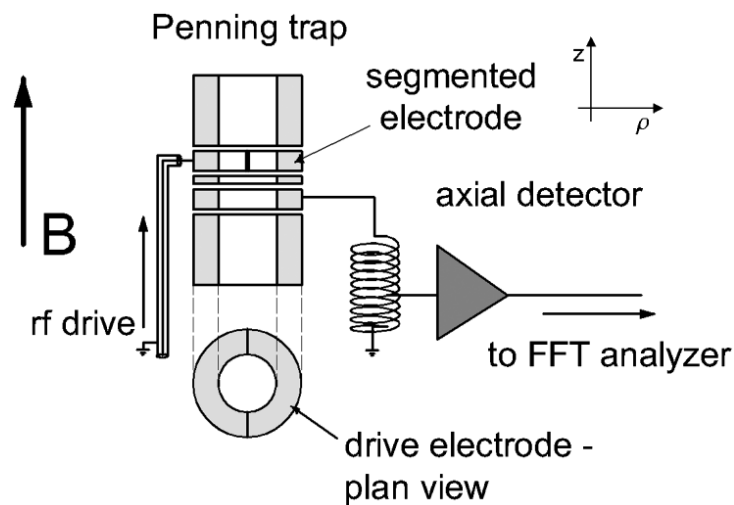


Figure 2.7 The schematic of the sideband coupling method in the Penning trap. A shielded transmission line guides the rf drives to a radially segmented trap electrode. Cited from [41]

The motional frequencies of the radial modes  $\nu_+$  and  $\nu_-$  of the particle are measured by the sideband coupling [42]. Figure 2.7 shows the setup of the sideband coupling method. A radio frequency (rf) drive at a frequency  $\nu_{rf}$  is applied to the radially segmented trap electrodes. The quadrupole rf-drive with an electric field

$$\mathbf{E}_{rf} = E_0 \sin(2\pi\nu_{rf}t)(z\hat{e}_\rho + \hat{\rho}_z) \quad (2.32)$$

is irradiated to the trap.  $E_0$  denotes the electrical field amplitude and  $\nu_{rf} = \nu_\pm \mp \nu_z$  is the drive frequency which couples the modified cyclotron (magnetron) motion to the axial motion. This results in a periodic exchange of energy between the two modes, leading to an amplitude-modulated axial motion [41]:

$$\begin{aligned} z(t) &= z_0 \cos\left(\frac{1}{2}\Omega_0 t\right) \sin(2\pi\nu_z t) \\ &= z_0 \left( \sin\left[2\pi\left(\nu_z + \frac{\Omega_0}{4\pi}\right)t\right] + \sin\left[2\pi\left(\nu_z - \frac{\Omega_0}{4\pi}\right)t\right] \right) \end{aligned} \quad (2.33)$$

where  $\Omega_0$  is the resonant Rabi frequency defined as  $\Omega_0 = qE_0/(4\pi m\sqrt{\nu_{\pm}\nu_z})$  [42]. From Eq. (2.33), the frequency spectrum is a coupled component of two components  $\nu_l = \nu_z - \frac{\Omega_0}{4\pi}$  and  $\nu_r = \nu_z + \frac{\Omega_0}{4\pi}$ . If the drive frequency is detuned by  $\delta_{\pm} = \nu_{rf} - \nu_{\pm} \pm \nu_z$ ,  $\nu_{l,r}$  will become

$$\nu_l = \nu_z - \frac{\delta_{\pm}}{2} - \frac{\Omega_{\pm}}{4\pi} \quad (2.34)$$

$$\nu_r = \nu_z - \frac{\delta_{\pm}}{2} - \frac{\Omega_{\pm}}{4\pi} \quad (2.35)$$

where  $\Omega_{\pm} = \sqrt{\Omega_0^2 + 4\pi^2\delta_{\pm}^2}$  is the off-resonant Rabi frequency. These sideband frequencies are observed as a double dip at  $\nu_l$  and  $\nu_r$ . Combining Eq.(2.35) and the definition of  $\Omega$  and  $\delta$ , the modified cyclotron frequency  $\nu_+$  is extracted as

$$\nu_+ = \nu_{rf} + \nu_l + \nu_r - \nu_z \quad (2.36)$$

The magnetron frequency can be measured by in a separate sideband coupling measurement, or simultaneously by sideband coupling of the "cyclotron-dressed-state" to the magnetron motion described in [41]. Together with the axial frequency measurement by the axial detection system, the free cyclotron frequency  $\nu_c$  is obtained via the invariance theorem in Eq.(2.5).

### 2.3.3 Measurement of the Larmor frequency

As the spin precession of the trapped particle is not accompanied by a detectable image current, the Larmor frequency  $\nu_L$  cannot be directly observed by the image current detection system. A solution for the non-destructive measurement of  $\nu_L$  is provided from the continuous Stern-Gerlach effect, which was introduced for the electron and the positron  $g$ -factor measurements [27]. In this scheme, the inhomogeneous magnetic field of the form

$$B_z(\rho, z) = B_0 + B_2(z^2 - \rho^2/2) \quad (2.37)$$

which is called "magnetic bottle", is superimposed to the trap by introducing a ferromagnetic ring electrode.  $B_0$  is the coefficient of the homogeneous magnetic field,  $B_2$  is the coefficient of the inhomogeneity,  $z$  is the axial coordinate and  $\rho$  is the radial coordinate. Figure 2.8 shows a schematic of the magnetic bottle and its magnetic field.

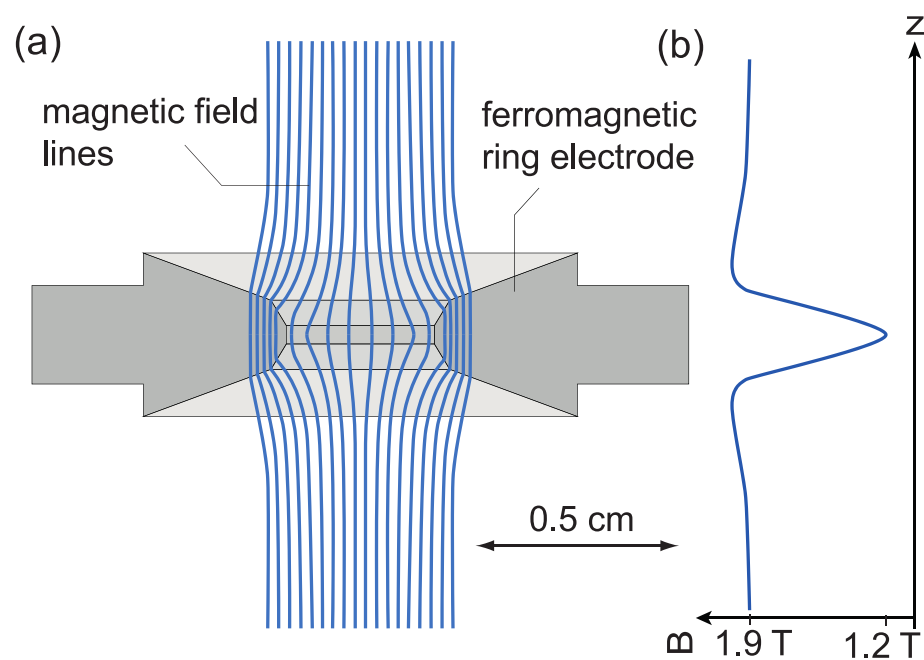


Figure 2.8 Schematic of the magnetic bottle at AT. (a) the ferromagnetic ring electrode and the magnetic field lines formed as Eq.(2.37). (b) On axis magnetic field of the magnetic bottle. Cited from [26].

By the magnetic bottle, a magnetic potential  $\Phi = -\vec{\mu} \cdot \vec{B}_z$  is added to the axial electrostatic potential of the trap. This couples the magnetic moment of the trapped particle to its axial frequency. Therefore, the measurement of  $\nu_z$  enables the non-destructive detection of the spin-eigenstate. Figure 2.9 shows the effective potential and axial frequency difference of spin-up/spin-down states by the magnetic bottle. A spin flip causes an axial frequency shift of

$$\Delta\nu_{z,SF} = \frac{1}{2\pi^2} \frac{\mu_{\bar{p}} B_2}{m_{\bar{p}} \nu_z} \quad (2.38)$$

where  $\mu_{\bar{p}}$  and  $m_{\bar{p}}$  are the magnetic moment and the mass of the antiproton, respectively.

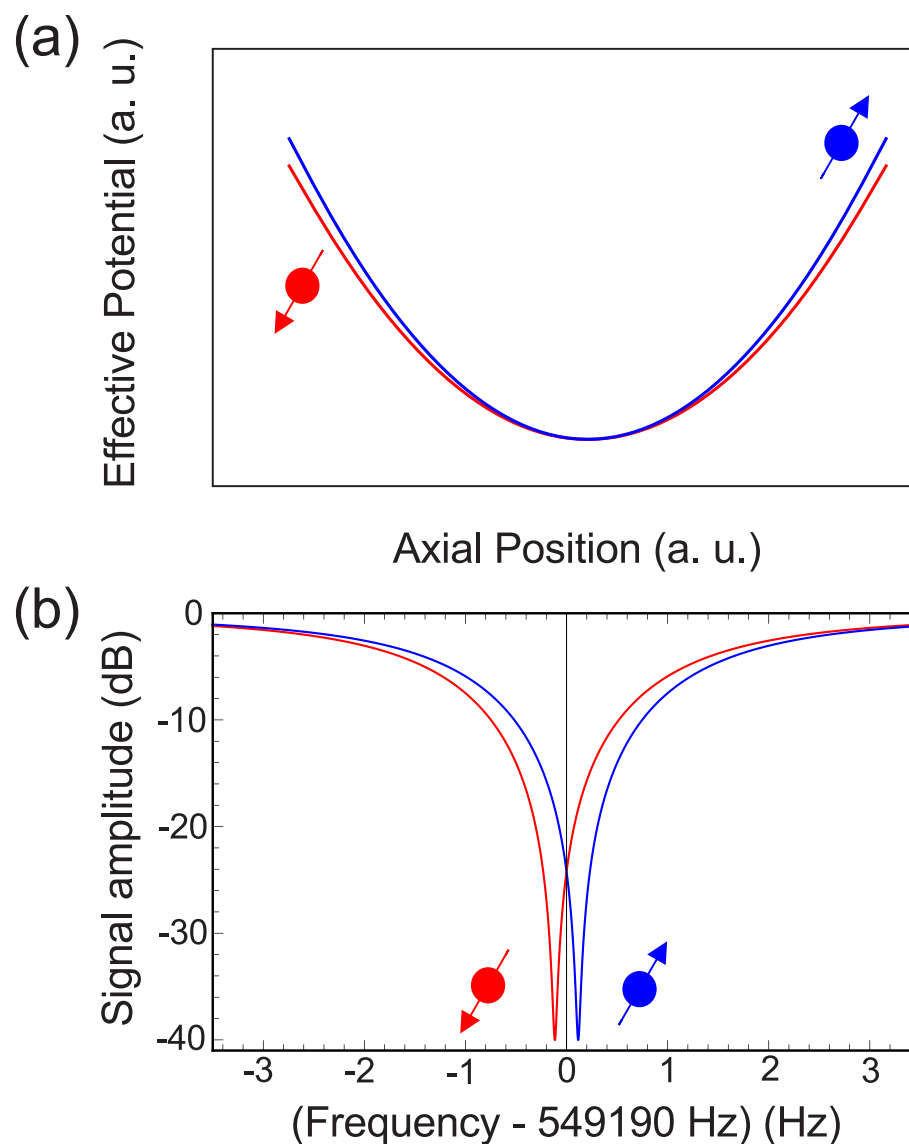


Figure 2.9 Illustrations of the continuous Stern-Gerlach effect. The blue and red line represent the spin-up state and the spin-down state, respectively. (a) The effective potential of the axial motion in the presence of the magnetic bottle is shown. As the magnetic potential  $\Phi = -\vec{\mu} \cdot \vec{B}$  is added to the axial electrostatic potential, the effective potential will be different by the direction of the spin eigenstate. This effective potential difference causes to the the axial frequency difference between spin-up state particle and spin-down state particle. (b) is the calculated signal amplitude related to the noise amplitude of the detection system. In the BASE apparatus, the axial frequency difference due to a spin flip is 180 mHz out of 675 kHz [49]. Cited from [26].

By Eq.(2.38), the axial frequency shift caused by the continuous Stern-Gerlach effect scales linearly with the strength of the magnetic bottle  $B_2$  and the ratio  $\mu/m$ . However the  $\mu/m$  ratio is extremely small for the proton/antiproton system. Comparing to the electron-positron system [5],

the proton magnetic moment is approximately 660 times smaller [26]. Therefore at the BASE experiment a strong magnetic bottle of  $B_2 = 300\,000\text{ T/m}^2$  is superimposed to the trap for the spin state analysis [31]. With this condition,  $\Delta\nu_{z,SF} = 180\text{ mHz}$  out of  $675\text{ kHz}$  is achieved [49].

Once the non-destructive detection of the spin transition is established, the Larmor frequency is obtained by measuring the spin transition probability  $P_{SF}$  as a function of an irradiated spin flip drive  $\nu_{rf,s}$  [43] [44]:

$$P_{SF}(\nu_{rf,s}) = \frac{1}{2} \left( 1 - \exp \left( -\frac{1}{2} \Omega_R t_0 \chi(\nu_{rf,s}) \right) \right) \quad (2.39)$$

where  $\Omega_R = 2\pi\nu_L b_{rf}/B_0$  denotes the Rabi frequency denotes with the magnetic drive amplitude  $b_{rf}$ ,  $t_0$  is the irradiation time,  $\chi(\nu_{rf,s})$  is the line shape of the Larmor resonance. Details are described in [43] [44].

## Chapter 3

# Experimental setup of BASE

### 3.1 AD beamline

The antiproton experiment of BASE is performed at the antiproton decelerator (AD) of CERN, the only facility which provides intense pulses of low energy antiprotons [18]. A pulse of about 30 million antiprotons of 150 ns lengths are provided in a 120 s cycle length, with the energy of 5.3 MeV. This antiproton beam is transferred and distributed to each experiments. Figure 3.1 shows a top view of the AD facility and the BASE experiment zone. Details about the AD ejection beamline for the BASE experimental zone is described in [26].

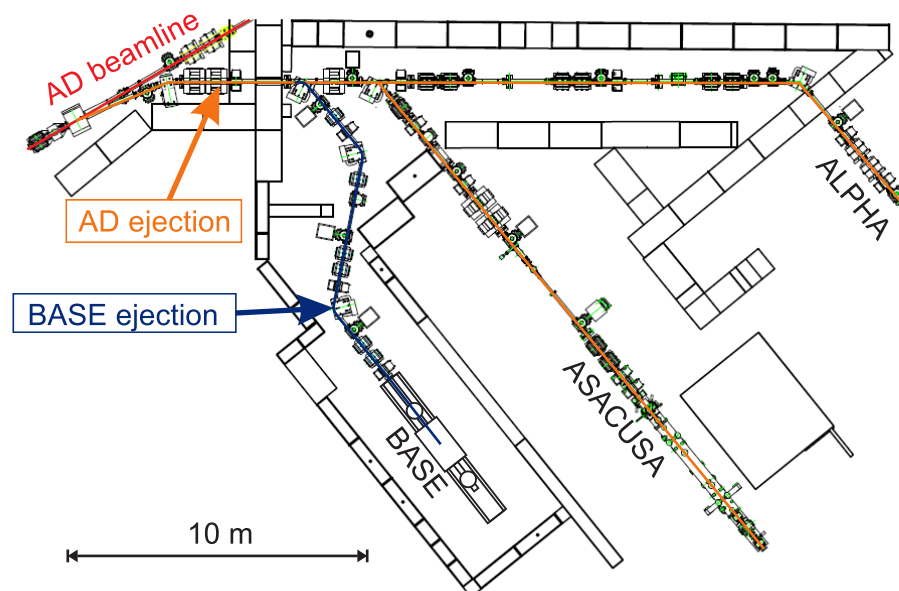


Figure 3.1 The top view of the BASE experimental zone at AD facility. Cited from [26].

## 3.2 Overview of the BASE apparatus

A schematic overview of the BASE experiment is shown at Figure 3.2. The Penning trap chamber is housed inside the horizontal bore of a 1.945 T superconducting magnet (*Oxford instruments*) together with the six detection systems. The trap system is placed inside a hermetically sealed cryogenic vacuum chamber which is cooled to liquid helium temperature ( $\sim 4$  K) by the two cryostats placed upstream and downstream of the magnet. A horizontal support structure anchored on both ends to the cryostats is called liquid helium stage. This holds the trap chamber in the magnet bore inside an isolation vacuum. The detection systems are attached to the liquid helium stage, next to the Penning trap. A segment with cryogenic electronics and filters for the voltage biasing of the trap electrodes are also attached to the liquid helium stage next to the trap chamber. The antiprotons ejected from the AD beamline are injected into the Penning trap through a vacuum-tight degrader foil. At the degrader foil, energetic antiprotons penetrate the degrader material, lose energy in inelastic scattering process, and are eventually stopped at a certain energy range. At 0.0001 fraction of the incident, antiprotons transmit through the thin degrader and can be trapped by high voltage ramps. The technical details of the degrader design is described in [26].

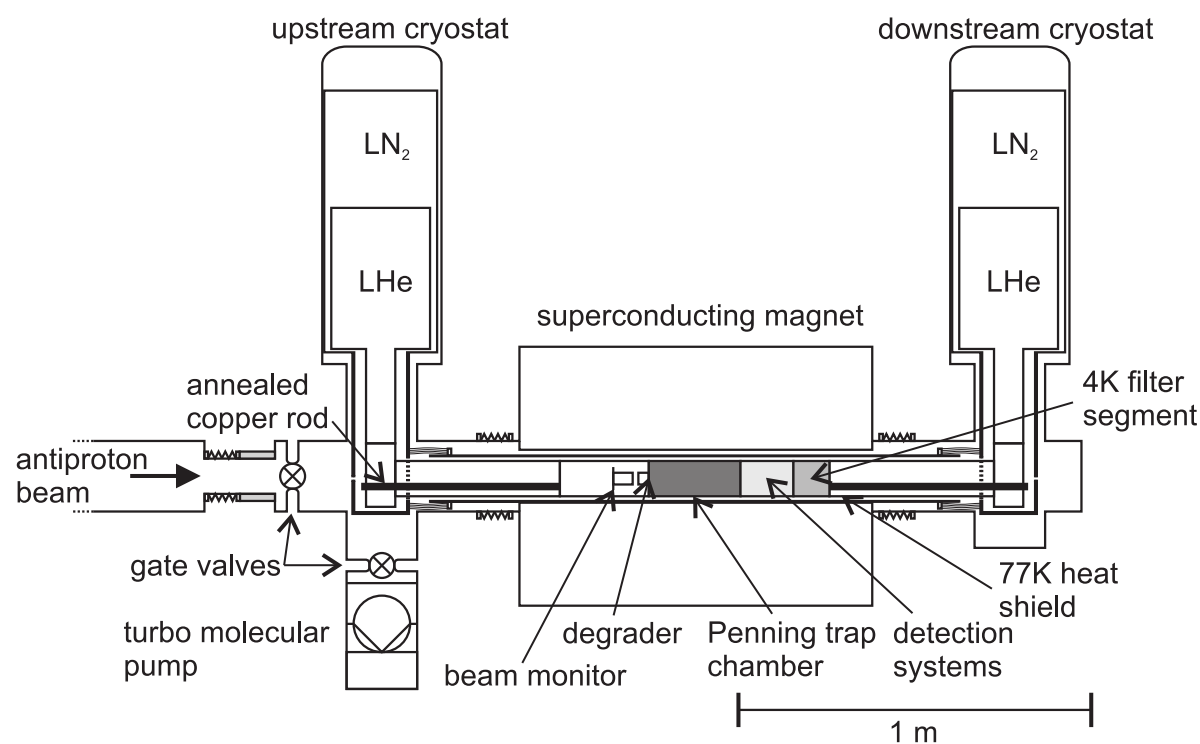


Figure 3.2 The overview of the BASE experimental zone. Cited from [26]

To perform a high precision measurement of the charge-to-mass ratio and the  $g$ -factor, the re-

quirement of the superconducting magnet is to have a highly homogeneous magnetic field with high temporal stability. This is because the magnetic field stability directly defines the precision of the cyclotron and Larmor frequency (see Eq.(1.1) and Eq.(1.4)). Since the BASE experimental zone is located inside the AD facility, external magnetic field noise occurs, which is caused by the AD operation, crane actions and the neighboring experiments. Therefore, it is important to have a self-shielding solenoid coil inside the magnet, which wraps around the trap-can. This suppresses the internal magnetic field fluctuation caused by the external magnetic field noise. Details about the external magnetic field study and the self shielding geometry are described in [29].

### 3.3 The Penning trap assembly

The schematic of the BASE experiment is shown in Figure 3.3. The trap is installed in the homogeneous center of the superconducting magnet. The stack consists of four cylindrical traps in five electrode orthogonal and compensated design [30]. The individual traps are interconnected by transport electrodes in an optimal length-to-diameter, and all electrodes are gold-plated to prevent oxidation. The four cylindrical traps in BASE consist of the *reservoir trap* (RT), the *cooling trap* (CT), the *precision trap* (PT) and the *analysis trap* (AT). RT/PT and CT/AT have inner diameter 9.0 mm and 3.6 mm, respectively.

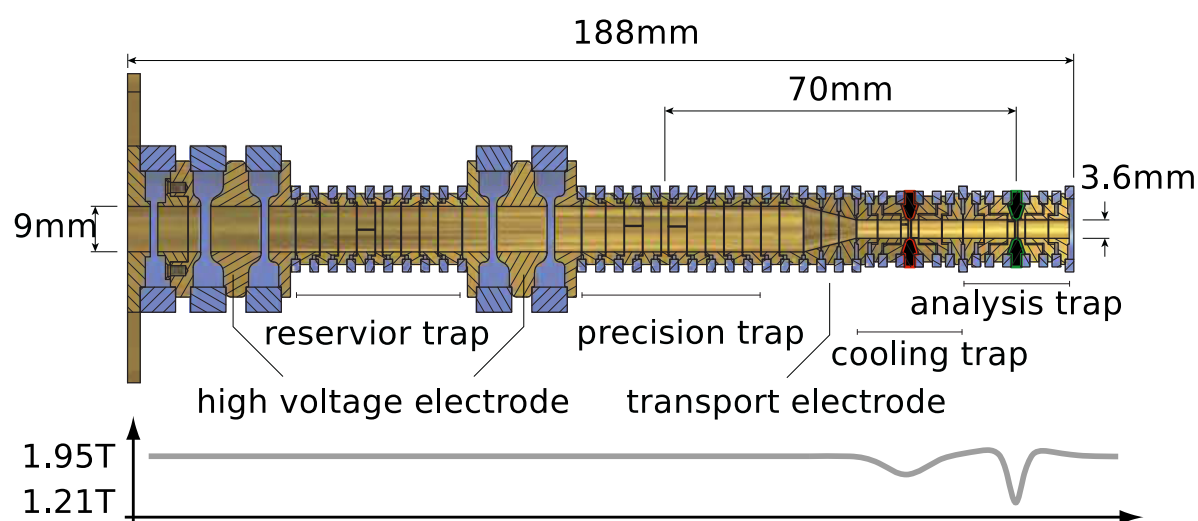


Figure 3.3 The schematic of Penning trap assembly at BASE. It consists of four cylindrical traps interconnected by transport electrodes. The inner diameter of the reservoir trap (RT) and precision trap (PT) is 9.0 mm and that of cooling trap (CT) and analysis trap (AT) is 3.6 mm. The lower graph shows the on-axis magnetic field of the trap assembly. The trap is installed in the homogeneous center of the superconducting magnet. The strong inhomogeneity in the analysis trap is for the spin state analysis, and the smaller inhomogeneity in the cooling trap is for the efficient cooling of the antiproton's cyclotron mode. Cited from [26]

*Precision trap* (PT) and *analysis trap* (AT) are used to measure the magnetic moment by application of the double trap technique [24]. The PT is for the precision frequency measurement and the AT is for the spin state analysis of the antiproton [31]. The layout of the AT is an exact copy of well working analysis trap used for proton experiments at Mainz University [32]. For the requirement of high magnetic field inhomogeneity in AT, a ferromagnetic material Co/Fe is used for the ring electrode as a magnetic bottle [31].

The *reservoir trap* (RT) frequency is operated in online mode as a catching trap to capture and store low energy antiproton from the AD ejection. At the upstream and downstream of the trap high voltage electrodes are placed, which allows applications of catching pulses up to 5 kV. The RT enables long-term storage of antiprotons and allows BASE to operate the measurement even during the accelerator shut-down periods and to perform measurements when the magnetic noise at the AD hall is low. In the offline mode the RT serves as a reservoir for antiprotons. The methods of RT were developed to extract a single particle from a cloud of antiprotons and to shuttle this particle to the precision measurement traps [34]. The PT is placed next to the RT and the antiproton is transported by the transport electrodes connected to these traps. Voltage ramps applied to the transport electrodes allow adiabatic particle shuttling along the trap axis. The entire trap assembly is placed between a degrader system with 224  $\mu\text{m}$  aluminum equivalent thickness on the upstream side [31], and a field emission electron-gun to provide electrons for the sympathetic cooling of antiprotons on the downstream side [33]. The details about the reservoir trap are described at [34].

The *cooling trap* is the trap which is planned to be installed in the future. The purpose of the CT is fast and efficient cooling of the cyclotron mode of trapped antiprotons. This is essential for single spin-flip experiments to prepare particles with low cyclotron energies [35]. The Details are described in [26].

The assembly of the trap is shown in Figure 3.4. The trapped electrodes are pressed together by two plates which are fixed on the upper and lower end of a tripod made out of oxygen-free electrolytic (OFE) copper. The electron gun is connected to the lower plate and the entire assembly is attached to the pinbase flange by three OFE copper spacers. The spin-flip coils to drive spin transitions are placed on PTFE support structures mounted to the tripod. This assembly is placed into the Penning trap chamber.

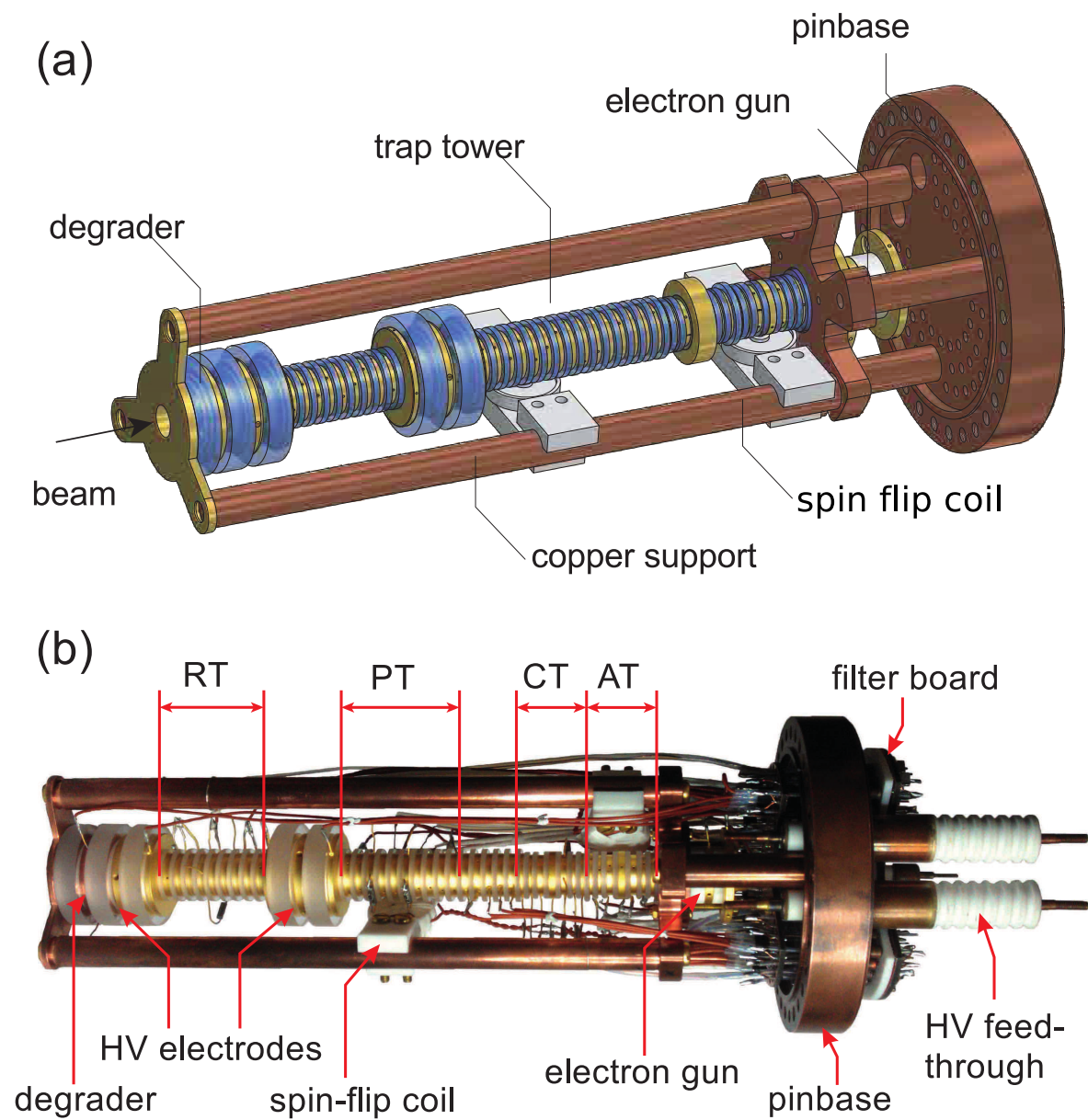


Figure 3.4 Entire assembly of Penning trap system (a) drawn as a 3D model and (b) the picture of the Penning trap assembly. Cited from [26].

## Chapter 4

# Axial frequency tuning

The proton-to-antiproton charge-to-mass ratio was measured by BASE with 69 p.p.t. precision [13]. The major systematic uncertainty in this measurement was caused by the voltage adjustment of the ring electrode which was required to tune the antiprotons and negatively charged hydrogen ions to the resonance with the detection system. This caused a shift of the particle position, and together with a slightly inhomogeneous magnetic field, it induced a systematic frequency shift. Details will be explained in the next section. One strategy to overcome this systematic limitation is the development of a detection system with a tunable axial frequency. This detection system enables to measure the charge-to-mass ratio of the antiproton and the  $\text{H}^-$  ion without changing the potential of the Penning trap.

### 4.1 Concept of the charge-to-mass ratio measurement

Here the charge-to-mass ratio which BASE performed [13] is explained. This measurement was performed by a comparison of the cyclotron frequency of the antiproton and the  $\text{H}^-$  ion, instead of the proton. This was to avoid the systematic shift caused by the polarity switching of the trapping voltage. Figure 4.1 shows the Penning trap setup for the charge-to-mass ratio. A difference to the initial definition is, that the measurement was carried out in the reservoir trap and the precision trap was used for the storage of the antiprotons. The original reservoir trap is far away from the traps with the magnetic gradients, and in this trap the magnetic field was most homogeneous. The measurement trap is adjacent to upstream and downstream park electrodes. This allows to shuttle and park the single antiproton and the single  $\text{H}^-$  ion and measure with each particle continuously. The cloud of the antiprotons is stored at the reservoir trap and the sympathetic cooling is performed by the electron gun.

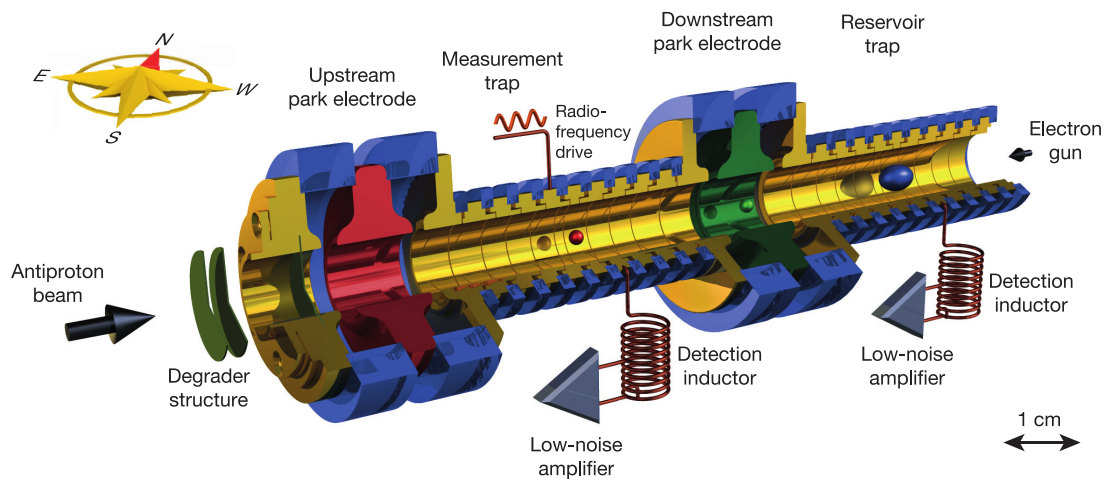


Figure 4.1 The Penning trap setup for the charge to mass ratio measurement in [13]. The measurement is carried out at the *measurement trap* and the antiprotons are stored at the *reservoir trap*. Resonant superconducting detection systems are connected to *measurement trap* and the *reservoir trap*. The radio-frequency drives for the sideband coupling are applied to the upstream side correction electrode of the *measurement trap*. The upstream and the downstream park electrodes are used for the particle shuttling scheme applied in the charge-to-mass ratio comparison. Cited from [13].

While one particle was measured in the *measurement trap*, the other particle was parked in the park electrode. Figure 4.2 shows the experimental cycle of the measurement. **a** shows the measurement cycle which is triggered by the AD beamline ejection, to avoid the systematic shift induced by beats between the measurements and ambient field fluctuations caused by the cycle of AD. **b** and **c** shows the potential configuration at the measurement of each particle. Details of the charge-to-mass ratio measurement is described in [13].

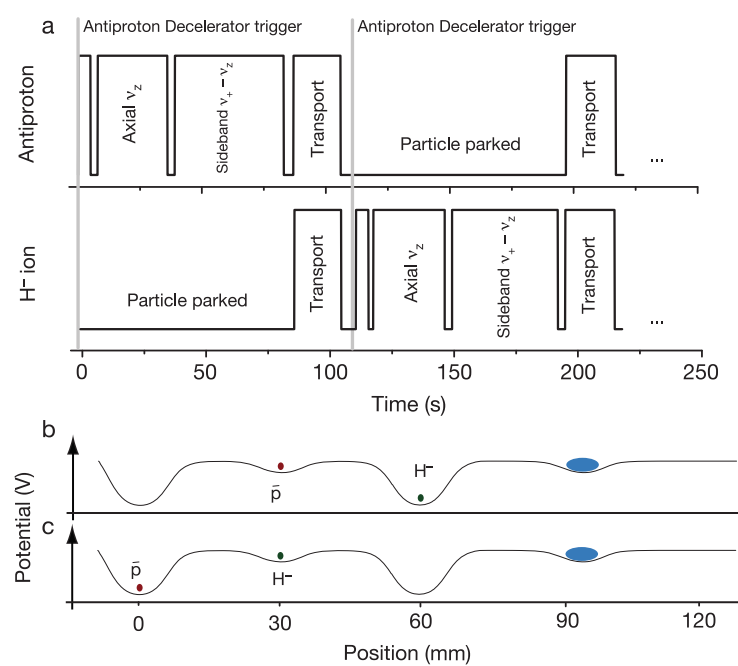


Figure 4.2 The measurement cycle of the charge-to-mass ratio measurement. **a** is the detailed illustration of the measurement cycle. **b** and **c** are the potential configuration of the cyclotron frequency measurement of the antiproton and the H<sup>-</sup> ion, respectively. The blue ellipse represents the reserved particle in the reservoir trap. Cited from [13].

The concept of the measurement was by evaluating the ratio of the individual free cyclotron frequencies  $\nu_c = (q/m) \cdot (B/2\pi)$  as

$$R = \frac{\nu_{c,\bar{p}}}{\nu_{c,H^-}} = \frac{(q/m)_{\bar{p}}}{(q/m)_{H^-}}. \quad (4.1)$$

This concept is based on the assumption that the antiproton and the H<sup>-</sup> ion experience the identical magnetic field. However in a high precision measurement, this assumption needs to be critically investigated. Since tiny technical asymmetries and trap imperfections are present in each trap setup, the magnetic field differs between the measurement of antiprotons and H<sup>-</sup> ions. These systematic effects are discussed in section 4.1.1.

### 4.1.1 Trap asymmetry

The trap potential in the ideal Penning trap is explained at section 2.2 (see Figure 2.3). If the trap is in a perfectly symmetric potential, trapped particles stay at the trap center and there is no systematic effect when the voltage is adjusted. However in reality, by voltage offsets, geometrical offsets and voltage dividers, the trap potential becomes asymmetric. Figure 4.3 shows the major offsets of the Penning trap in the right side. The offset voltages  $\Delta V_i$  are order of 10 mV to 200 mV

which arise from the calibration offset of the power supply, tiny current leaks in the high impedance filters and thermal contact potential build between 300 K area and 4 K area of the setup. The geometrical offsets  $\Delta l_i$  is caused by machining errors and mounting tolerances of the apparatus. The magnitude of voltage divider  $F_4$  is caused by the parallel resistance of the detection system connected to the correction electrode. By considering these offsets, the potential loses its symmetry and this causes the axial position shift of the particle.

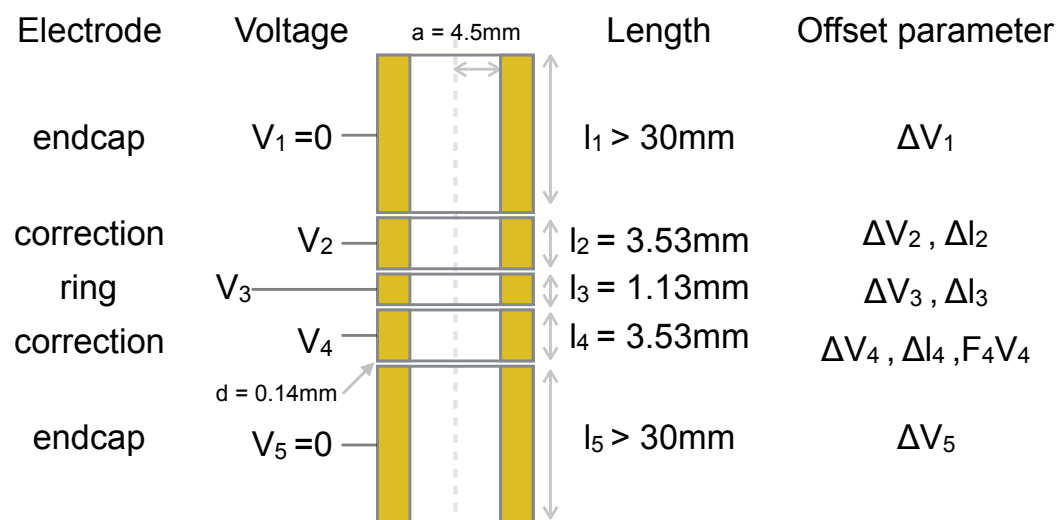


Figure 4.3 The penning trap for the cyclotron detection system consists of one ring electrode at the center, two correction electrodes adjacent to both sides and two grounded endcap electrodes at both ends.  $V_i$  is the applied voltage and  $l_i$  is the length of each electrode. The trap diameter is  $2a = 9$  mm and each electrodes are spaced by sapphire rings to fix the inner distance of the electrode to  $d = 0.14$  mm. The offset parameter corresponds to the voltage offset  $\Delta V_i$ , geometrical offset  $\Delta l_i$  and the magnitude of voltage divider  $F_i$ . Since the length of the endcap is more than 30mm, the the geometrical offsets  $\Delta l_1$  and  $\Delta l_5$  are negligible. Furthermore, most of the voltage divider are known as negligible by the leak current measurement, except  $F_4$  caused by the detection system. [13]

### 4.1.2 Voltage adjustment

In BASE, the free cyclotron frequency  $\nu_c$  is measured by tuning the axial frequency of the particle  $\nu_z$  to resonance with the axial detection system  $\nu_0$  and performing sideband coupling spectroscopy [13], explained at section 2.3.2. Here the tuning of the axial frequency is discussed. The axial

frequency of the trapped particle is defined as

$$\nu_z = \frac{1}{2\pi} \sqrt{2C_2 V_3 \frac{q}{m}} \quad (4.2)$$

where  $V_3$  is the voltage applied to the ring electrode and  $1/\sqrt{C_2}$  is a trap specific length. This axial frequency is tuned to the resonance frequency ( $\nu_0 = 645\,262$  Hz [13]) and therefore it requires the voltage adjustment for different particles, practically the voltage difference between antiproton and  $H^-$  ions is at 5 mV out of about 5 V. At the measurement of BASE, the  $H^-$  ion, a proton combined with two electrons, is used instead of proton for the the charge-to-mass ratio measurement comparing to the antiproton. This is to match the polarity and to avoid large change of the voltage adjustment.

When comparing charge-to-mass ratio of  $H^-$  ion to the antiproton, the mass difference need to be considered which is

$$m_{H^-} = m_p \left( 1 + 2 \frac{m_e}{m_p} - \frac{E_b}{m_p} - \frac{E_a}{m_p} + \frac{\alpha_{pol,H^-} B_0^2}{m_p} \right). \quad (4.3)$$

$m_e/m_p$  is the mass ratio of electron to proton [45],  $E_b$  is the binding energy [46],  $E_a$  is the electron affinity of Hydrogen [47], and  $(\alpha_{pol,H^-} B_0^2)$  is the term of polarizability shift [48]. From this mass difference and Eq.(4.2), the adjustment of the ring voltage for each particle is required. Therefore, considering with the trap potential asymmetry, the axial positions of the proton and  $H^-$  shift from the center and the position difference is about 30nm. Details are illustrated in Figure 4.4.

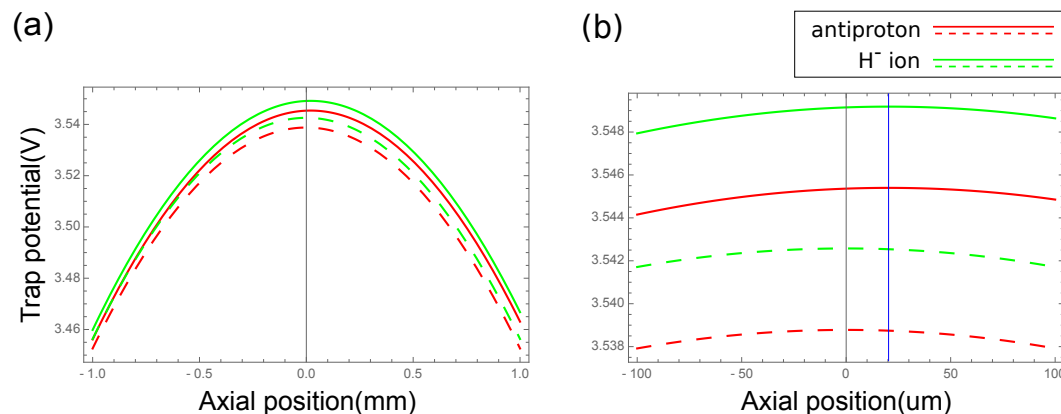


Figure 4.4 The trap potential difference which is tuned for the antiproton and the  $H^-$  ion. For the ring electrode,  $V_3 = 4.664499$  V is used at the  $q/m$  measurement for antiproton, and for the  $H^-$  ion the voltage was adjusted as  $H^-$  ion as  $(V_{3,H^-} - V_{3,\bar{p}}) = \Delta V_3 = 0.005003$  V [13]. From the negative polarity of the particle, the positive potential maximum decides the position of the particle. The dashed lines are the ideal trap potentials which is calculated by Eq.(2.14) and the solid lines are the potentials which the offsets are added. (a) is the trap potential graph of the scale of  $\pm 1$  mm and (b) is a expansion of that at  $\pm 100$   $\mu\text{m}$  scale. The blue line ( $z \sim 20$   $\mu\text{m}$ ) corresponds to the shift of the potential maximum when the offsets are considered, comparing to the ideal potential. From further calculation, the axial position difference of antiproton and  $H^-$  ion is  $(z_{\bar{p}} - z_{H^-}) \sim 30$  nm.

### 4.1.3 Homogeneity of the magnetic field

From the beginning assumption of the completely identical magnetic field and from Eq.(4.3), the ratio of cyclotron frequency of antiproton and  $H^-$  ion is theoretically calculated as

$$R_{theory} = \frac{\nu_{c,\bar{p}}}{\nu_{c,p}} = \frac{(q/m)_{\bar{p}}}{(q/m)_{H^-}} = 1.001089218754(2). \quad (4.4)$$

However in reality the magnetic field is inhomogeneous, and moreover the axial positions of the antiproton and the  $H^-$  ion are different, which was discussed in the previous subsection. Therefore, by considering the magnetic field as a function of the axial position, the experimental value needs to be evaluated as

$$R_{exp} = \frac{(q/m)_{\bar{p}}}{(q/m)_{H^-}} \frac{B(z_{\bar{p}})/2\pi}{B(z_{H^-})/2\pi}. \quad (4.5)$$

The inhomogeneous magnetic field can be described in linear approximation as  $B(z) = B_0 + B_1 z$  which  $B_0 = 1.945$  T and  $B_1 = -7.58(42)$  mT/m and higher order coefficients can be negligible [13].

Therefore the the systematic shift of the cyclotron frequency ratio can be calculated as

$$\left(\frac{\Delta R}{R}\right) = \frac{B_1 \Delta z (\Delta V_3)}{B_0}. \quad (4.6)$$

In previous BASE charge-to-mass ratio measurement the  $B_1$  and  $\Delta V_3$  was determined and the systematic correction of the  $R_{exp}$  was -114 p.p.t.. However the uncertainty of the systematical correction still remained as 26 p.p.t. [13], which is impossible to suppress in any statistics. Therefore to measure the charge-to-mass ratio with higher precision, a tunable axial detection system will be an alternative and desirable. This is discussed in the next section.

## 4.2 Tunable axial detection system

The idea of the voltage adjustment of the ring electrode was to tune the axial frequency  $\nu_z$  of the particle to a certain resonance frequency  $\nu_{res}$  of the axial detection system, and the systematic shift of the charge-to-mass ratio measurement was mainly caused by this voltage adjustment  $\Delta V_3$  between antiprotons and  $H^-$  ions. The concept of the tunable axial detection system is do the opposite procedure, which means to tune the resonance frequency to each axial frequency without adjusting the voltage. From this idea the effective axial position will not be changed by the ring voltage adjustment ( $\Delta z (\Delta V_3) = 0$ ) and therefore the systematic shift which was discussed will be suppressed by this method.

The resonance frequency is decided by the inductance and the effective parallel capacitance of the detection system

$$\nu_{res} = \frac{1}{2\pi} \sqrt{\frac{1}{LC_{eff}}} \quad (4.7)$$

which  $L$  is the inductance of the resonator and  $C_{eff}$  is the effective parallel capacitance. As the inductance is a constant due to the resonator, the effective parallel capacitance can be the only variable to tune the resonance frequency. Figure. (4.6) shows how the whole setup of the tunable axial detection system will be. The main point of this setup is, the varactor is connected parallel to the axial detection system so that the effective parallel capacitance of the whole detection system is tunable as

$$C_{eff} = C_p + \frac{C_v C_{in,v}}{C_v + C_{in,v}} \quad (4.8)$$

when considering only the capacitance of resonator and the varactor circuit, for simplicity.  $C_p$  is the parallel capacitance of the resonator,  $C_v$  is the tuned capacitance of the varactor itself and  $C_{in,v}$  is the input capacitance applied mandatory to the varactor circuit. By tuning the  $C_v$  and

selecting the proper  $C_{in,v}$ , the resonance frequency  $\nu_{res}$  can be tuned to the range which matches to the axial frequency of the antiproton and the  $H^-$  ion.

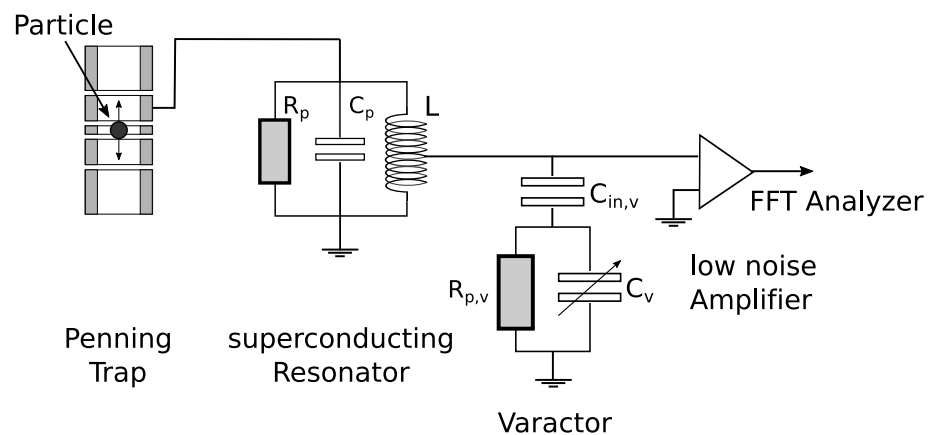


Figure 4.5 The whole setup of the tunable axial detection system.

The important component of this system, the varactor, is a p-n junction diode which acts as a voltage-controlled variable capacitor. In general the equation of the capacitance between two plates with area  $S$  distance  $d$  between the material with permittivity  $\epsilon$  is

$$C = \epsilon \frac{S}{d} \quad (4.9)$$

and this is also applicable to the varactor. When the varactor is reversed-biased, the distance of the p-channel area and the n-channel area will be separated and the thickness of the depletion layer  $d$  will increase and the varactor capacitance  $C_v$  will decrease by this. Once such a varactor is connected in parallel to the detection system, this makes its overall resonance frequency adjustable.

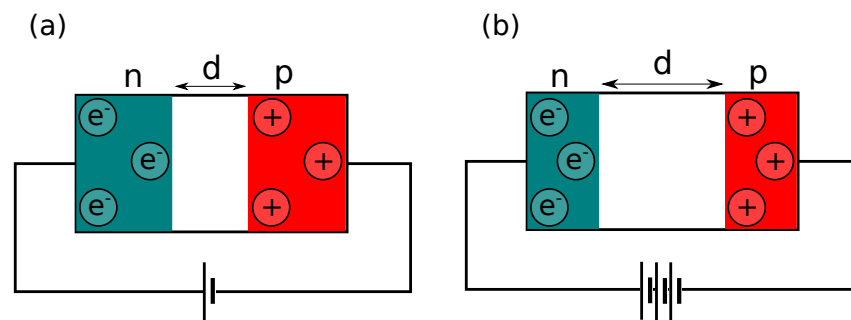


Figure 4.6 The p-n junction of the varactor. When the reversed-biased voltage increase, the free electron in the n-channel and the holes in p-channels will be separated. In that way the depletion layer  $d$  increases and the capacitance decreases by increasing the voltage.

For the detection system, a gallium arsenide (GaAs) hyperabrupt junction varactor MA46H072

(*MACOM*) is selected because of the wide capacitance tuning range and the high quality factor. In fact MA46H072 is used for the cyclotron detection system of the BASE apparatus [49]. However the problem is that the effective parallel resistance of the entire detection system will decrease due to the varactor as

$$R_{eff} = \frac{R_p R_{p,v} / \kappa_l^2}{R_p + R_{p,v} / \kappa_l^2} \quad (4.10)$$

where  $R_p$  is the parallel resistance of the resonator,  $R_{p,v}$  is the parallel resistance of the varactor and  $\kappa_l$  is the coupling factor due to the inductance (explained in Chapter 5). This resistive loss is harmful in high precision measurement because it will lead to the Q-value loss

$$Q = \frac{R_{eff}}{2\pi\nu_0 L}, \quad (4.11)$$

which relates to a loss of sensitivity of the detection system.

Therefore, to proof the feasibility of using the MA46H072 varactor for the axial detection system, this should fulfill the requirements as follows:

- The tuned resonance frequency range covers the axial frequency of antiproton and  $H^-$  ion ( $\Delta\nu_z \sim 340$  Hz difference out of  $\nu_z \sim 645$  kHz, calculated from the mass difference)
- It should induce small resistive losses compared to the setup without varactor
- Appropriate and reliable functioning at cryogenic temperature ( $\sim 4$  K) should be demonstrated

By considering these factors, the varactor is tested with the resonator in cryogenic temperature and the results are written in Chapter 6.

## Chapter 5

# The principles of the axial detection system

Besides the traps and a stable superconducting magnet, highly-sensitive superconducting detection systems form the major part of each high precision Penning trap experiment. Such detection systems are formed of a superconducting resonator and low-noise amplifiers, with the purpose of amplifying the fA-order image currents and extract the eigenfrequency information with high sensitivity and low noise. Moreover for the tunable axial detection system, suggested in the previous chapter, the varactor is installed in parallel to the detection system. Here the mechanism and the development of the axial detection system are explained from parts. The main principle of the axial detection system is based on [38], [50] and [51].

### 5.1 Resonator

#### 5.1.1 Equipment

For the axial frequency measurement an axial detection resonator is attached in each trap. In BASE we use two small resonators ( $d = 41$  mm) and two big resonators ( $d = 48$  mm), located in the cryogenic region of the experiment, outside of the trap can but as close to the trap as possible. Figure 5.1 shows the schematic of the detection electronics segment, which is installed in the cryogenic part of the experiment. Details of the resonator designs are described in [38]. The axial resonator which is used for the measurement in this thesis is the big size resonator with  $d = 48$  mm diameter.

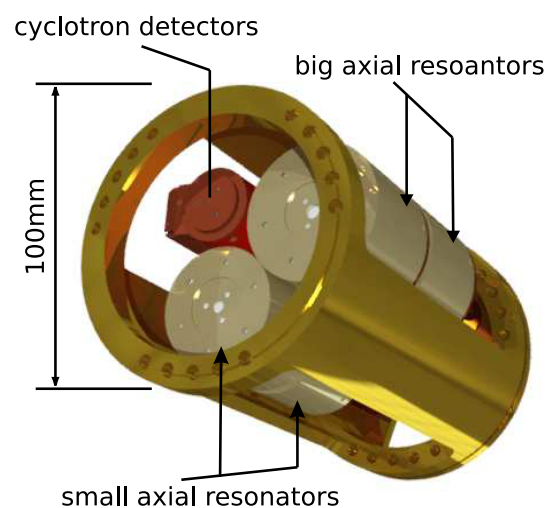


Figure 5.1 The electronic segment so called "trap can", which houses two small size ( $d = 41$  mm) and two big size ( $d = 48$  mm) detection systems for the axial frequency measurement, and two detection system for the modified cyclotron frequency measurement [26].

Figure 5.2 shows the schematic of the big axial resonator. The axial resonator is composed of a toroidal superconducting coil, a polytetrafluoroethylene (PTFE) core, two PTFE holders and a cylindrical metal housing. The toroidal geometry of the coil is to confine the magnetic field within the inductor and to reduce resistive losses induced by the stray magnetic field. The coil is made out of type II superconducting NbTi wire because of its superconductivity in cryogenic temperature ( $T_c = 9.3$  K) and this material has high critical field strength, which enables to install the resonator inside the 1.945 T superconducting magnet at the BASE apparatus. The coil is wound on the PTFE core and the winding number is  $N = 1200$ . The windings are covered by tightly fixed PTFE tapes which has a low dielectric loss tangent  $\tan(\delta) = 10^{-4}$ . This enables good thermalization, which is critical for superconducting devices. The most specific part of the axial resonator is the existence of a third end branched from the coil, which is called *tap end*. The position of the tap is crucial for the final parameters of the detection system, as explained in section 5.1.2.

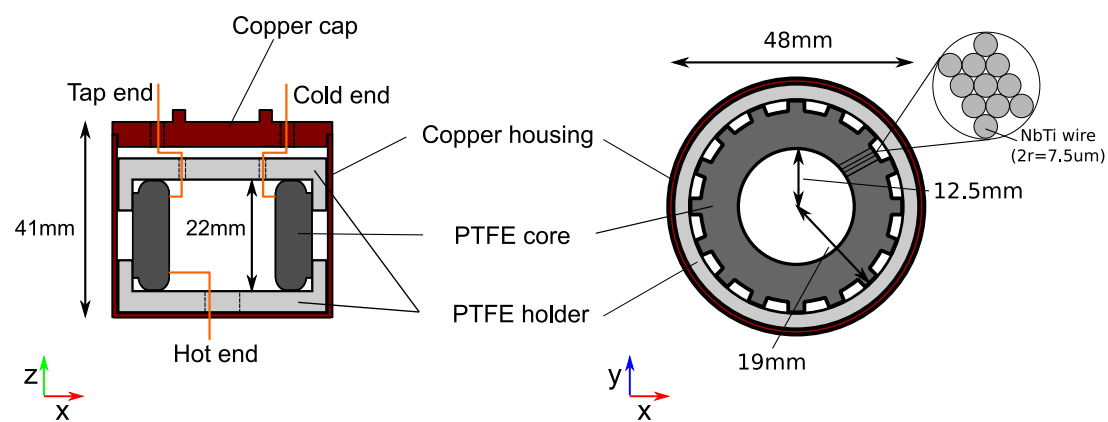


Figure 5.2 The schematic of the resonator composed of coil, PTFE holder, and the metal housing. The NbTi coil is packed inside the PTFE holder and the metal housing to make a good thermal contact. The coil has three ends, hot and cold end at the terminal and the tap end branched from the coil. The ends of the coil has a good soldering joint connected to the copper wires by the lead solder which makes a good thermal contact in cryogenic temperature.

### 5.1.2 Mechanism

The superconducting coil for the axial resonator is composed of three ends, *hot*, *cold* and *tap*. The hot end, the input part of the resonator, is connected to the Penning trap. The cold end is connected to the ground. The most important part, the tap end is branched from the coil and connected to the amplifier. Figure 5.3 is the equivalent circuit of the resonator and shows the positions of its three ends. The equivalent LCR parallel circuit consists of inductance of the coil  $L$ , the parallel capacitance  $C_p$  and the parallel capacitance  $R_p$ .  $N_1$  and  $N_2$  are the winding numbers of the coil between cold-tap ends and tap-hot ends.

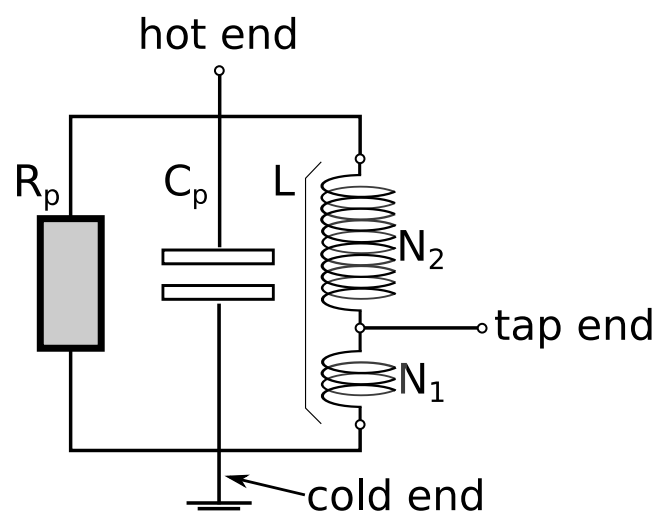


Figure 5.3 The resonator can be expressed equivalent as a LCR parallel circuit of an inductance  $L$  with a parallel capacitance  $C_p$  and a parallel resistance  $R_p$ . In the axial detection system, the branched tap end divides the coil as  $N_1$  times winding between cold-tap ends and  $N_2$  times winding between tap-hot end. This provides a coupling factor of the inductor as  $\kappa_l = N_1/(N_1 + N_2)$ .

As the resonator acts as a LCR circuit, the resonance frequency can be expressed as

$$\nu_0 = \frac{1}{2\pi\sqrt{LC_p}} \quad (5.1)$$

with the quality factor of the resonator, Q-value as

$$Q = \frac{R_p}{2\pi\nu_0 L}. \quad (5.2)$$

The reason of making a tap end on the resonator is to set a coupling factor between the resonator and the amplifier, and to tune the performance parameters of the detection system. The coupling factor of the inductor due to the tap position is expressed as

$$\kappa_l = \frac{N_1}{N_1 + N_2}. \quad (5.3)$$

As the position of the tap matters to the performance parameters of the detection system, this should be selected carefully and already be considered when manufacturing the device. The coil which is used for the measurement in Chapter.6 had the coupling factor  $\kappa_l = 0.24$ .

### 5.1.3 Q-value loss by the metal housing

The Q-value in the Eq.(5.2) represents the loss mechanism of the parallel resistance dissipation. However the loss mechanism also exists between the coil and the metal housings of the resonator.

The resonator used in the axial detector is made of the toroid coil, however when the turn of the wire is uneven, some magnetic field lines will leak out of the coil. This magnetic field leak induces the eddy current in the metal housing. Therefore the energy and the Q-value loss by the eddy current are due to the resistance of the housing material. Details of the loss mechanism of the resonator are described in [53].

In the experiment in Chapter 6, superconducting NbTi housing and oxygen-free copper housing are tested. In BASE experiment NbTi housings were used for the axial detection system by low Q-value loss due to the eddy current, however the thermal conductivity of NbTi is low that it is difficult to cool to liquid helium temperature without additional thermal conducting material, such as copper braids. One solution to the thermal conductive problem is to use the OFH copper housing. This has a high thermal conductivity, however the inertial resistance is higher than superconducting NbTi housing. Therefore, to install the resonator with the copper housing, this needs to be evaluated whether it possess a sufficient Q-value for the detection system.

## 5.2 Amplifier

As the axial detection system is required to detect and amplify the fA-order image current induced by the charged particle oscillation, the amplifier should work in cryogenic temperature with high sensitivity and low equivalent input noise from  $e_n$ .

### 5.2.1 Dual-gate MES-FET

For the requirement of the low equivalent input noise, n-channel dual-gate GaAs Metal Semiconductor Field Effect Transistors (MES-FET) are appropriate and used for the cryogenic amplifier circuit of all detection systems for the BASE experiment [50]. Figure 5.4 shows the schematic. the gate electrodes and the semiconductor of MES-FETs form a Schottky junction. In particular, GaAs MES-FETs are known as they work under cryogenic temperature due to the small band gap of GaAs [54] [59] [60].

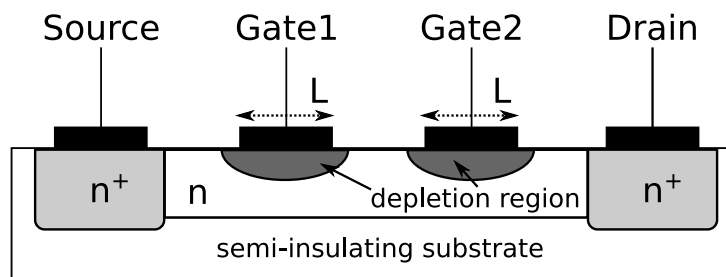


Figure 5.4 The schematic of n-channel dual-gate MES-FET. The gate electrodes and the semiconductor form a Schottky junction. By the application of a negative voltage to the gates, the depletion regions are formed and therefore the drain-source current is controlled.  $L$  is the length of the gate channel. The schematic is not based on proper scale.

In the operation of the n-channel FET, the drain-source current is controlled by the negative gate voltage. When the gate voltage is 0 V and the drain is biased, a current will flow from drain to source. When a negative voltage is applied to the gate, the depletion layer of the Schottky junction increases, and thereby the drain current decreases. Therefore the n-channel MES-FET behaves like a voltage controlled resistor with a large transconductance.

The reason of MES-FET which has dual-gate is used to reduce the  $1/f$  noise  $S_{1/f}$  [ $V^2/Hz$ ] which is expressed as follows [55]:

$$S_{1/f} = \frac{q\mu_n\alpha_H I_D V_{DS}}{g_m^2 L^2} \frac{1}{f} = A_f \frac{1}{f} \quad (5.4)$$

where  $q$  is the electron charge,  $\mu_n$  is the electron mobility,  $\alpha_H$  is the experimental Hooge's factor,  $I_D$  is the drain current,  $V_{DS}$  is the drain-source biased voltage,  $g_m$  is the transconductance, and  $L$  is the gate length [55][56][57]. This equation shows that the  $1/f$  noise depends inverse to the gate length of the FET. Moreover, the interconnection of the Gate is known that this will make the FET equivalent to the single gate FET which has a doubled gate length  $2L$  and reduce the equivalent input noise of the FET [55]. From the Equation (5.4), this method will reduce the coefficient of the  $1/f$  noise in theory. To introduce this to the axial detection system at the BASE setup, the MES-FET with gate1-gate2 shorted and disconnected amplifier circuit is tested in cryogenic temperature. The results and evaluation are discussed in Chapter 6.

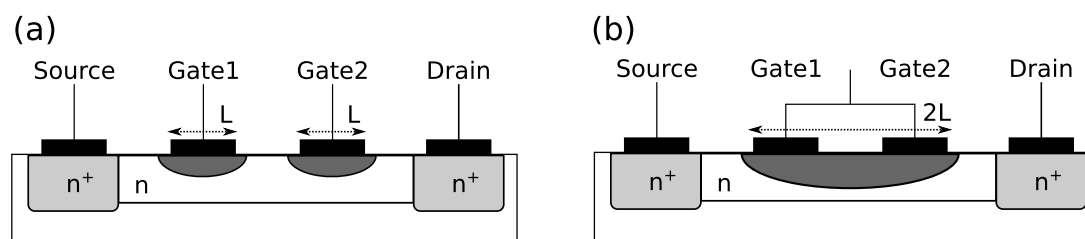


Figure 5.5 The schematic of n-channel dual-gate FET with (a) Gate1-2 disconnected and (b) Gate1-2 shorted. By the interconnection of the gates, the device becomes equivalent to single-gate FET with a doubled gate length  $2L$ . In this way, the equivalent input noise due to the  $1/f$  noise is less than (a). Again the schematic is not based on proper scale.

### 5.2.2 Common-source and source-follower circuit

The amplifier is based on two stages, a common-source circuit for the input stage and a source-follower circuit for the output stage. Figure 5.6 shows schematics of the two different circuit types.

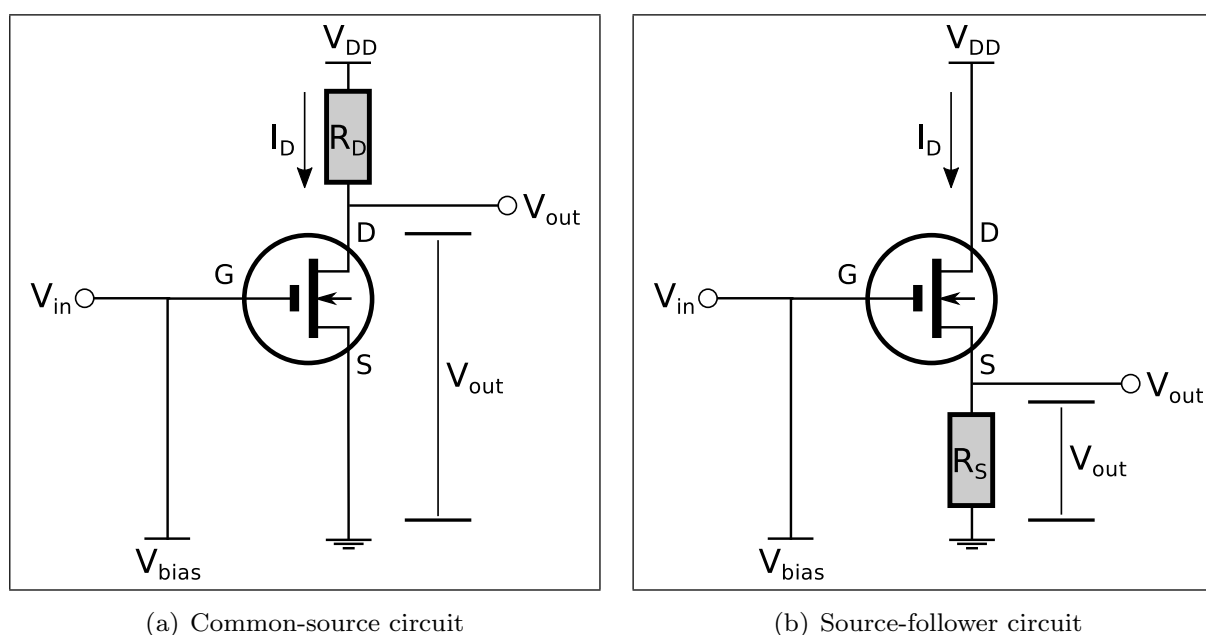


Figure 5.6 The schematics of the input and output FET stages of the amplifier. (a) is the common-source FET circuit used in the input stage which has a high gain but high output impedance. (b) is the source-follower FET circuit used in output stage which has no gain but low output impedance. By the connection of the circuit (a) and (b), the amplifier enables to have a high gain with low output impedance which can match the impedance to the FFT analyzer. For easiness, single gate FETs are used in this schematic.

The common-source circuit is a FET circuit with a input signal and a output signal connected

to the gate and the drain, respectively while the source is usually grounded. As the FET is n-channel MESFET, the gate biased voltage ( $V_G$ ) needs to be negative to operate the FET. By the character of the FET, the drain current ( $I_D$ ) can be expressed by the gate-source voltage ( $V_{GS}$ ) and transconductance ( $g_m$ ) as

$$I_D = g_m V_{GS}. \quad (5.5)$$

In this case, the gate-source voltage is same as input voltage ( $V_{GS} = V_{in}$ ). As the output phase is opposite to the input, the output signal can be expressed as

$$V_{out} = R_D I_D = -R_D g_m V_{in} \quad (5.6)$$

and the gain of the circuit is derived as

$$A = V_{out}/V_{in} = -R_D g_m \quad (5.7)$$

Therefore, this circuit can obtain a high gain, which is essential for detecting the fA-order image current. However this circuit also has an output impedance ( $V_{out}/I_{out} = R_D$ ). From Eq.(5.6), R needs to be a big resistance to obtain a high gain, and as a result this disables the impedance matching to the FFT analyzer which has the 50Ω input impedance.

The source-follower circuit, which is also called the common drain circuit, is a FET circuit which input connected to the gate and output connected to the source while the drain is biased by a stable voltage. In this circuit, the output voltage is expressed as

$$V_{out} = R_S I_D. \quad (5.8)$$

By Equation (5.5) the drain current in this case is

$$\begin{aligned} I_D &= g_m V_{GS} \\ &= g_m (V_{in} - V_{out}) \end{aligned} \quad (5.9)$$

Therefore, the gain of the source-follower circuit is derived from Eq.(5.8) (5.9)

$$\begin{aligned} A &= V_{out}/v_{in} \\ &= \frac{R_S g_m}{R_S g_m + 1} \sim 1 \quad (R_S g_m \gg 1) \end{aligned} \quad (5.10)$$

which means that there is no gain by the source-follower circuit. However, this also has a low output impedance. This can be shown explicitly by considering a signal ( $v$ ) applied to the output with the grounded gate as Figure 5.7.

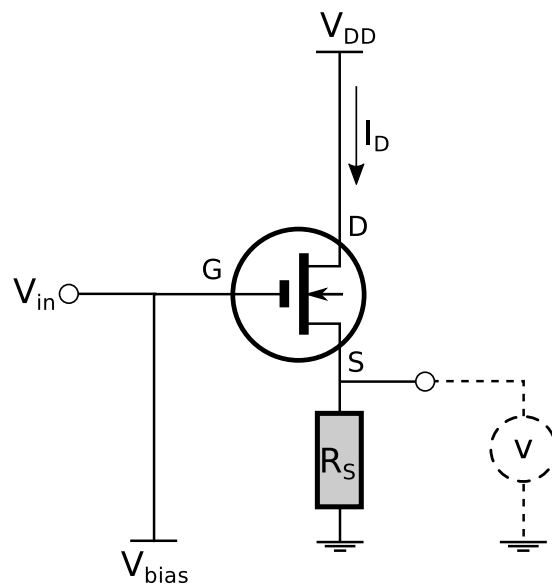


Figure 5.7 The source-follower circuit with a signal ( $v$ ) applied to the output.

As the drain current is  $I_D = g_m V_{GS} = g_m v$ , the output impedance becomes

$$R_{out} = v/I_D = \frac{1}{g_m} \quad (5.11)$$

and this enables to match the impedance with the  $50\Omega$  input impedance of the FFT analyzer. The idea is referred from [58]. Therefore, the combination as the common-source circuit for the input stage and the source-follower circuit for the output stage is efficient to obtain a high gain with a low input impedance matches to the FFT analyzer.

### 5.2.3 Amplifier circuit

The amplifier is based on the input stage FET for the amplification and the output stage FET for the source following. The schematic of Figure 5.8 is assembled on a high quality PTFE based laminated printed board. This printed board has a low loss tangent  $\tan \delta \sim 10^{-4}$  at cryogenic temperature [61]. The specific points of this amplifier are following.

- NE25139 (*NEC*) or 3SK164 (*SONY*) is used for the common-source circuit in the input stage FET, and CF739 (*Infineon*) are used for the source-follower circuit in the output stage FET.
- $100\text{M}\Omega$  resistance is for preventing the reduction of the effective parallel resistance  $R_{eff}$ .
- The drains are biased with small resistor to provide a necessary drain current.
- At the input port, a coupling capacitance  $C_{in}$  is applied. This capacitance decides the coupling factor  $\kappa_c$ .
- At the input stage FET, gate2 (G2) can be selected as shorted to Gate1 (G1) or disconnected.

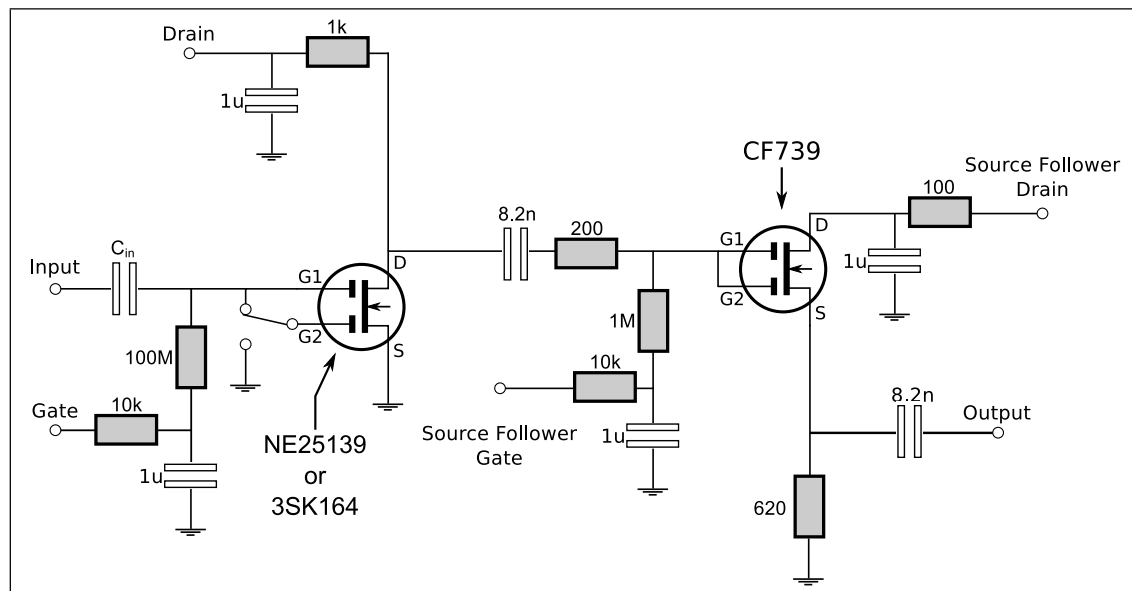


Figure 5.8 Amplifier circuit schematic for the axial detection system. The circuit has 2 signal ports and 4 biasing ports for the amplification. FET is formed of input stage FET which can choose the Gate1-Gate2 shorted or disconnected, and output FET act as the source follower. The circuit design is modified from the original design [50].

As an equivalent circuit, this can be represented as an ideal amplifier with an parallel resistance ( $R_{amp}$  and an capacitance  $C_{amp}$  with a coupling capacitance  $C_{in}$ . The equivalent circuit of the axial detection system is described at Figure 5.9. The coupling capacitance is to decide the value of the coupling factor, the factor which is related to the capacitance of the amplifier which is expressed as

$$\kappa_c = \frac{C_{in}}{C_{in} + C_{amp}}. \quad (5.12)$$

With this coupling factor and the coupling factor by the inductance in Equation (5.3), the effective parallel resistance can be described as

$$R_{eff} = \frac{R_p R_{amp} \kappa_l^{-2} \kappa_c^{-2}}{R_p + R_{amp} \kappa_l^{-2} \kappa_c^{-2}} \quad (5.13)$$

and the signal-to-noise ratio  $SNR$  [dB]

$$[SNR]_{dB} = 20 \log_{10} \left( \frac{\sqrt{4k_B T R_{eff}} \times \kappa_l \kappa_c}{e_n} \right) \quad (5.14)$$

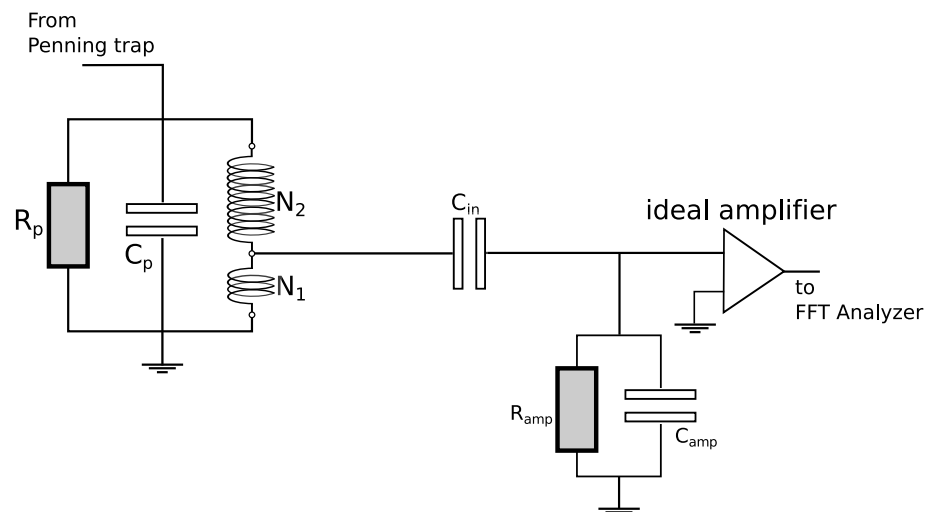


Figure 5.9 The equivalent circuit of the resonator and amplifier. The resonator is equivalent to LCR parallel circuit and the amplifier can be expressed as an ideal amplifier with a parallel resistance  $R_{amp}$ , a parallel capacitance  $C_{amp}$  and a coupling capacitance  $C_{in}$ . The position of the tap and the coupling capacitance effects to the coupling capacitance and decides the value of effective parallel resistance and the signal-to-noise ratio as Eq.(5.13) and (5.14).

### 5.3 Varactor system

To tune the resonance, the varactor board is connected parallel to the detection system. This board behaves as a variable parallel capacitance  $C_{p,v}$ . This relates to the tuning of the resonance frequency as

$$\nu = \frac{1}{2\pi\sqrt{L(C_p + C_{p,v})}}. \quad (5.15)$$

The parallel capacitance is decided by the varactor capacitance  $C_v$  and the equivalent input capacitance  $C_{in,v}$  as

$$C_{p,v} = \frac{C_{in,v}C_v\kappa_l^2}{C_{in,v} + C_v\kappa_l^2} \quad (5.16)$$

By selecting the equivalent input capacitance carefully, The range of the resonance frequency can be controlled. Also the coupling capacitance can decide the coupling factor due to the varactor capacitance as

$$\kappa_{c,v} = \frac{C_{in,v}}{C_{in,v} + C_v} \quad (5.17)$$

In the measurement at the next chapter,  $C_{in,v} = 4.7$  pF and  $2.2$  pF are used.

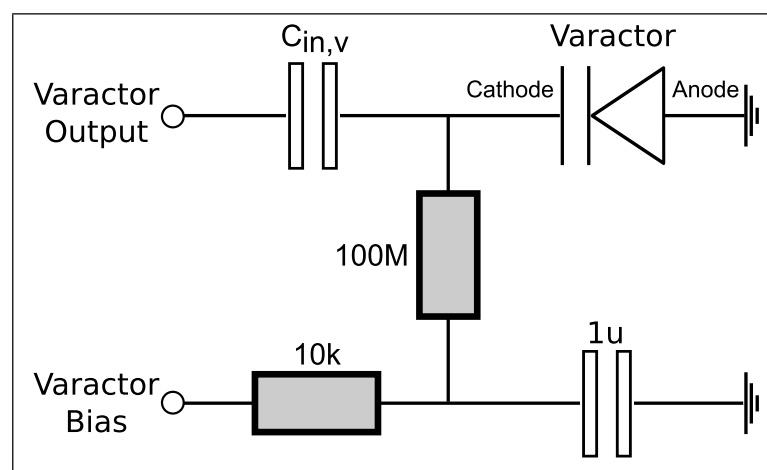


Figure 5.10 The schematic of the varactor board. "Varactor Output" is connected to the detection system parallel and "Varactor Bias" is connected to the outer voltage source. As the varactor anode is grounded, the varactor behaves as a tunable capacitance by the reversed positive biased voltage. 100 M $\Omega$  resistance is connected to the varactor bias to prevent the reduction of the effective parallel resistance  $R_{eff}$ .

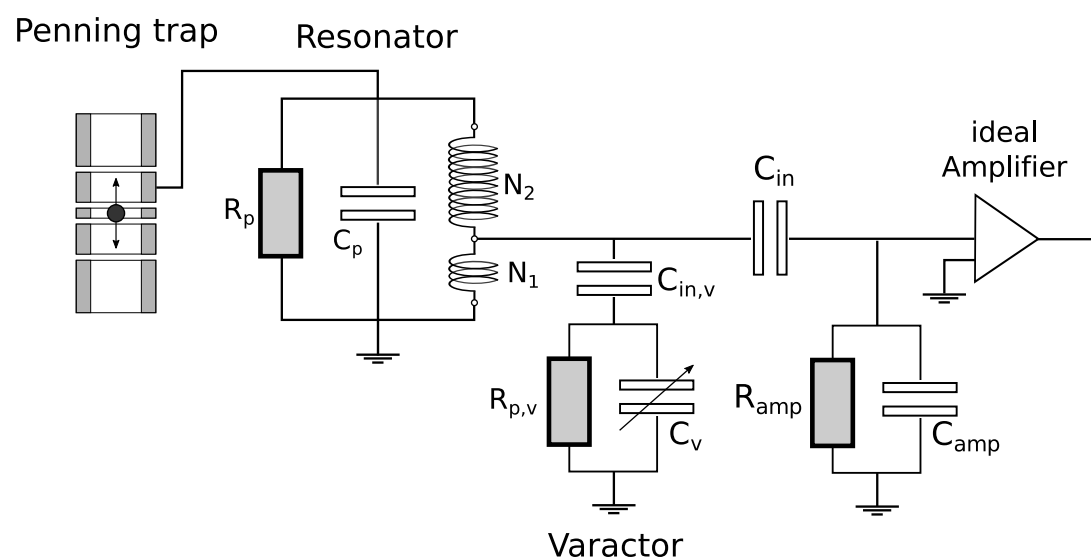


Figure 5.11 The equivalent circuit of the tunable axial detection system, which the Penning trap, resonator, varactor and the amplifier is connected.

By the parallel connection of the varactor to the axial detection system, the overview of the axial detection system will be as Figure 5.11. In this setup, the effective parallel resistance is decided by the parallel resistances of the components and the coupling factors  $\kappa_l$ ,  $\kappa_c$  and  $\kappa_{c,v}$  as

$$\frac{1}{R_{eff}} = \frac{1}{R_p} + \frac{1}{R_{p,v}} \kappa_l^2 \kappa_{c,v}^2 + \frac{1}{R_{amp}} \kappa_l^2 \kappa_c^2 \quad (5.18)$$

The one of the criteria to introduce the varactor in the axial detection system is to have a less  $R_{eff}$  loss by the parallel resistance  $R_{p,v}$ , which is sufficient to the measurement.

## Chapter 6

# Evaluation of the tunable axial detection system

Before installing the new axial detection system to the BASE experimental setup, it needs to be characterized under a condition which is identical to that of the main experiment. The main issue is the feasibility at cryogenic temperature, which is not self-explanatory from the room temperature measurement. In this chapter, first the setup for the cryogenic test is explained, and then the results and the evaluations of the cryogenic tests are discussed from each part, and finally the measurement of the whole detection system setup is discussed in the last section.

### 6.1 Setup for the cryogenic test

All parts of the detection system are tested at cryogenic temperature by using a cryogenic test setup which is driven by a pulse tube cooler (*Sumitomo GM*) (see Figure 6.1). For data-taking, different radio-frequency instruments are used, such as a network analyzer (*E5061B, Agilent*) and a spectrum analyzer (*FSVR2, R&S*). The biasing voltage are supplied by a controllable BS1-10 precision voltage source (*Stahl-electronics*). From the next section, the results of the cryogenic test for the resonator, the amplifier and the varactor are presented and the entire setup of the tunable axial detection system is discussed in the last section.

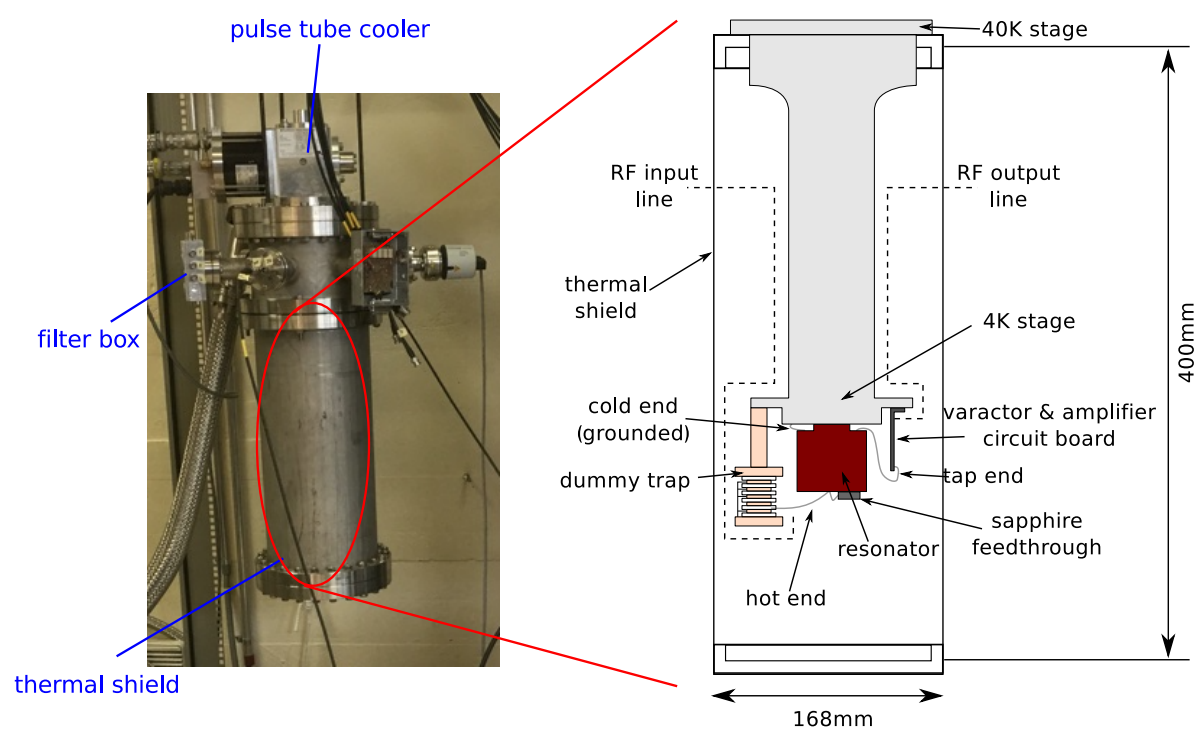


Figure 6.1 The equipment for the cryogenic temperature test, so called coldhead. The left picture is the overview of the coldhead. The right side schematic is the overview of the cryogenic test setup inside the thermal shield. A pulse tube cooler with two stages, RF lines, a bias voltage pinbase are mounted inside the vacuum chamber. At outside the connection lines for the RF, voltage bias, thermometer and filter boards are attached.

## 6.2 Resonator test

### 6.2.1 Material of housing

In the beginning of my master project, resonator housings in different materials have been tested, one made out of niobium titanium (NbTi) and another one made out of oxygen-free copper. The benefit of using the NbTi is the superconductivity which appears below the critical temperature of  $T_c = 9.1$  K which has small resistive losses and a high  $Q$ -value. However the thermal conductivity is low that it is difficult to cool down below the phase transition. So far in BASE experiment, superconducting resonator housings are used [38]. However, because of the low thermal conductivity, these housings require additional thermal conducting material, such as copper braids, which are wrapped around the housings. This approach takes space inside the cryogenic setup which could be available for additional cryogenic electronics. Moreover it complicates the assembly, which might increase a possibility to cause an electrical short by the parts of the braids. Therefore, constructing the housings without wrapping copper braids would facilitate the assembly of the

cryogenic experiment and would free the space for additional cryogenic electronics. Therefore, one strategy to avoid the low thermal conductivity of NbTi housing is changing the housing to a high thermal conductive material, the oxygen-free copper instead. By using the copper housing, the cooling problem will be solved by its high thermal conductivity. However, one of the reason of the energy loss is by eddy currents at the housing skin, the resistance of the housing material matters to the  $Q$ -value loss [53]. As copper is a conductor the  $Q$ -value loss will be bigger than the superconducting NbTi housing in cryogenic temperature, which means there is a possibility to reduce the precision of the experiment. Therefore, to install the copper housing to the BASE experiment, the copper housing resonator needed to be tested to prove that the  $Q$ -value is sufficiently high to achieve single particle detection efficiently.

The resonator is tested as Figure 6.2 in the cryogenic test setup and read-out by the network analyzer. Since a resonator is equivalent to a parallel LCR circuit, the inductance ( $L$ ), the parallel capacitance ( $C_p$ ) and the parallel resistance ( $R_p$ ) are derived by the resonance frequency ( $\nu_0$ ) and the  $Q$ -value ( $Q$ ) as

$$\nu_0 = \frac{1}{2\pi\sqrt{LC_p}} \quad (6.1)$$

$$Q = \frac{R_p}{2\pi\nu_0 L}. \quad (6.2)$$

At the test,  $\nu_0$  and the  $Q$  of the both NbTi and copper housing resonators are measured with the same NbTi toroid coil inside.

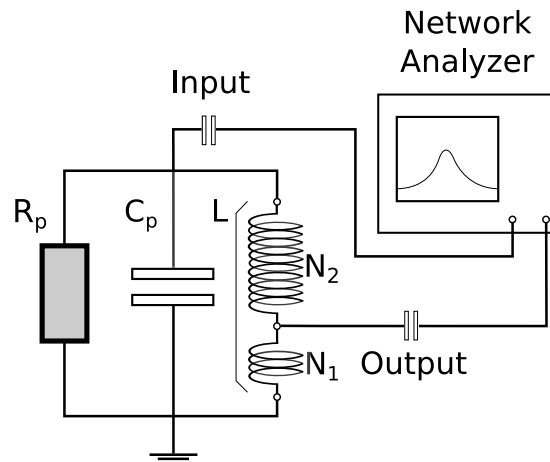


Figure 6.2 The setup of the test of the resonator measured by the network analyzer. The signal from the network analyzer is sent to the RF input line, which is coupled to the resonator's hot end. The resonated signal is picked up from the RF output line coupled to the tap end and sent back to the network analyzer. In this way the resonance frequency and the  $Q$ -value is measured.

To measure the inductance and the effective parallel capacitance of the resonator, the resonance of the free resonator and the resonator with an additional capacitance ( $C'$ ) is measured. By solving the simultaneous equation

$$\begin{aligned}\nu_0 &= 1/\sqrt{LC_p} \\ \nu'_0 &= 1/\sqrt{L(C_p + C')}.\end{aligned}\quad (6.3)$$

For the additional capacitance,  $C' = 10$  pF was used. From this measurement, the Inductance of the resonator  $L = 2.98$  mH was obtained. This value is consistent to the calculation of the inductance of toroid coil with a total winding number  $N \approx 1200$  as  $L \simeq 3.0$  mH which the equation is

$$L = \mu_0 \frac{h(R-r)}{2\pi a} N^2 \quad (6.4)$$

where  $\mu_0$  is the permeability of vacuum,  $h$ ,  $R$  and  $r$  are the height, outer radius and inner radius of the toroid, and  $a$  is the distance from the center of the toroid to the center of the tube, respectively. Subsequently, the parallel resistance is decided by the  $Q$ -value information and the known inductance. The results of the measurement are summarized in Table 6.1

Table 6.1 Results of the resonator with NbTi and copper housing

Material	Resonance (kHz)	$Q$ -value	$C_p$ (pF)	$R_p$ (M $\Omega$ )
NbTi	700	70000	17.1	959
Cu	840	61000	11.9	917

By comparing the results of  $Q$ -values and parallel resistances, the effect of the resistive loss caused by the copper housing comparing to the NbTi housing can be evaluated. However this was small compared to the losses which will eventually be induced by coupling resonator to the amplifier. Also the parallel capacitance difference was observed. The parallel capacitance of the resonator is caused by the stray capacitance between wires of the coil, the coil to the PTFE core, and the coil to the housing. From these evaluations, copper housing satisfied the requirement for the axial resonator. Therefore, since the easiness of thermalization and the sufficient  $Q$ -value, copper housing resonator is used for the new axial detection system. After this test, every following test is performed with the copper housing resonator.

## 6.2.2 Installation of the dummy trap

Next the copper housing resonator is tested with the dummy trap, which is a cylindrical Penning trap, similar to the ones used in the main experiment. This trap adds an additional parallel

capacitance  $C_{trap}$  with high intrinsic quality factor of the system. Figure 6.3 shows the setup of the resonator test and its equivalent circuit. This leads to a reduction of the resonance frequency as  $\nu_0 = 1/2\pi\sqrt{L(C_p + C_{trap})}$ .

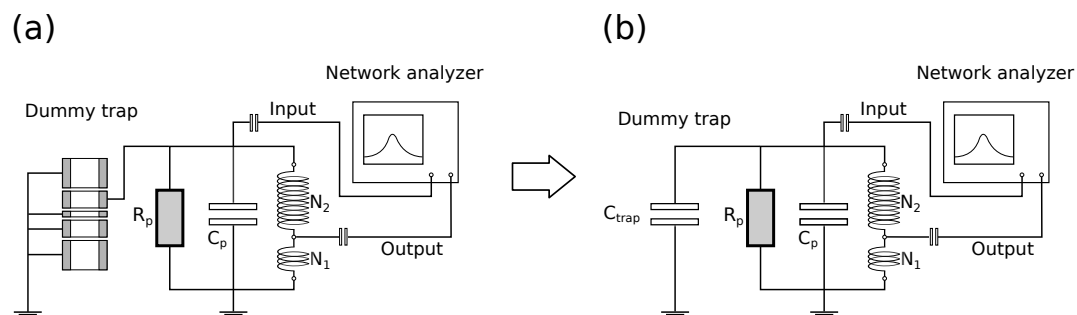


Figure 6.3 The equivalent circuit of the resonator test with the dummy trap. The trap installed resonator (a) can be interpret as (b) an additional capacitance  $C_{trap}$  with a high intrinsic quality factor.

The measured resonance and the  $Q$ -value are summarized in Table 6.2. From the result of the resonance frequency, the capacitance of the Dummy trap is calculated as 12.6 pF. Also the  $Q$ -value

Table 6.2 Results of the copper housing resonator with the dummy trap

Setup	Resonance (kHz)	$Q$ -value	$C_p$ (pF)	$R_p$ (G $\Omega$ )
Resonator	840	61800	11.9	0.98
Resonator + Dummy trap	589	117900	24.5	1.30

had a remarkable change. This is caused by the almost ideal trap capacitance with an extremely high quality factor, which means a capacitor with a negligibly small residual resistance. This causes the current flow to the trap and the residual resistance of the capacitance has less resistive loss and eventually leads to the increase of the  $Q$ -value. Figure 6.4 shows the principle.

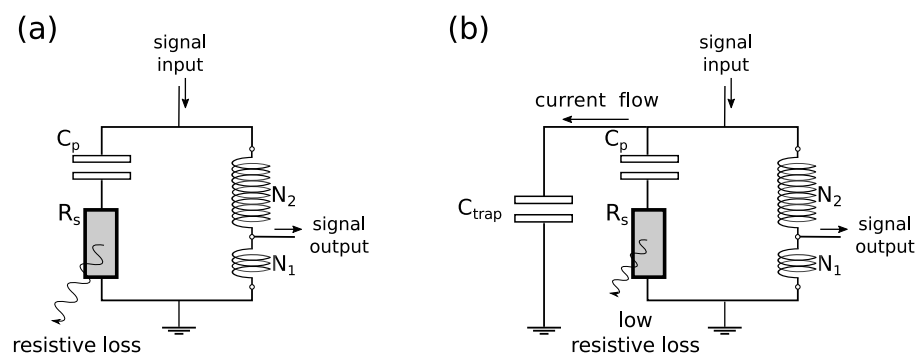


Figure 6.4 The resonator can be considered as a inductance and a capacitance with a series resistitance  $R_s$  as the Figure (a). By considering as this, the resistive loss is decided by the series resistance and the current flowing to the resistance. However by installing dummy trap, a capacitance with a negligibly small series resistance like Figure (b), the current flows to dummy trap and the resistive loss by the resonator will decrease. Therefore, the  $Q$ -value increases at the measurement by installing the dummy trap.

### 6.3 Varactor test

The varactor is tested with the resonator and the dummy trap, and measured by the network analyzer (see Figure 6.5). The resonance frequency  $\nu_0$  is tuned by the parallel capacitance of the varactor  $C_{p,v}$ , the coupling capacitor  $C_{in,v}$  and the varactor capacitance  $C_v$  as

$$\nu_0 = \frac{1}{2\pi\sqrt{L(C_p + C_{p,v}\kappa_l^2)}} \quad (6.5)$$

$$C_{p,v} = \frac{C_{in,v}C_v}{C_{in,v} + C_v}$$

where  $\kappa_l = N_1/(N_1 + N_2)$  is the coupling factor of the inductor defined by the tap position. The biased voltage is controlled by the voltage supply at  $-1 \text{ V} \sim 10 \text{ V}$  range and the input capacitance is tested with 4.7pF and 2.2 pF.

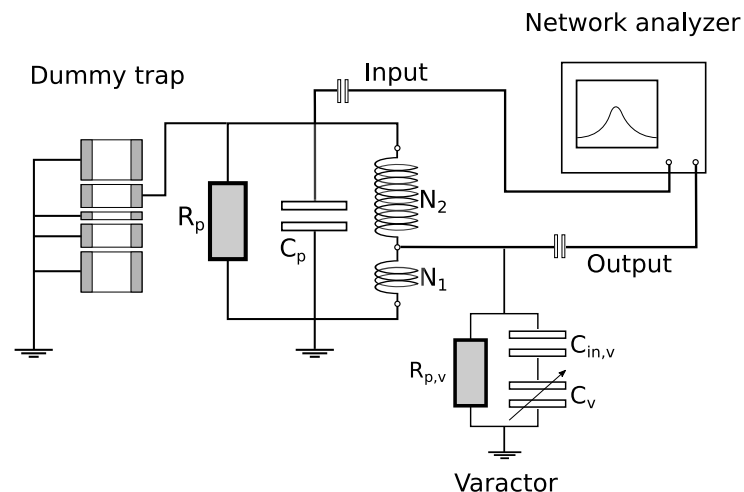


Figure 6.5 The system of the varactor test with the resonator and the dummy trap, measured by the network analyzer.

The requirements of the performance are following.

- Sufficient tuning range ( $\Delta\nu_0$ ) for the charge-to-mass ratio measurement
- Less resistive loss by the parallel resistance of the varactor  $R_{p,v}$
- Appropriate and reliable functioning at cryogenic temperature

Since every detection system for the Penning trap is working at cryogenic temperature, the first is criteria is of course necessary. The sufficient tuning range for the second criteria is  $\Delta\nu_0 > 340 \text{ Hz}$  out of 645 kHz resonance frequency, which is the value of the axial frequency difference between antiproton and  $\text{H}^-$  ion. The third criteria is also significant since the resistive loss in the varactor

causes a  $Q$ -value loss in the detector and in that way the sensitivity of the detection system is reduced. Considering these three requirements, the varactor board is first tested only with the free resonator, in order to characterize its effective parallel resistance, and then tested with the resonator and the dummy trap.

### 6.3.1 Component testing

The varactor was tested first by connecting it to the copper housing axial resonator. This is to check the range of the frequency shift by the applied voltage and to estimate its resistive loss. The coupling capacitance of the varactor circuit  $C_{in,v}$  was also evaluated to choose the frequency tuning range. Two capacitance values, 4.7 pF and 2.2 pF were tested. Figure. 6.6 shows the result of the resonance frequency shift. The initial resonance frequency in this measurement before loading the varactor was 849 kHz.

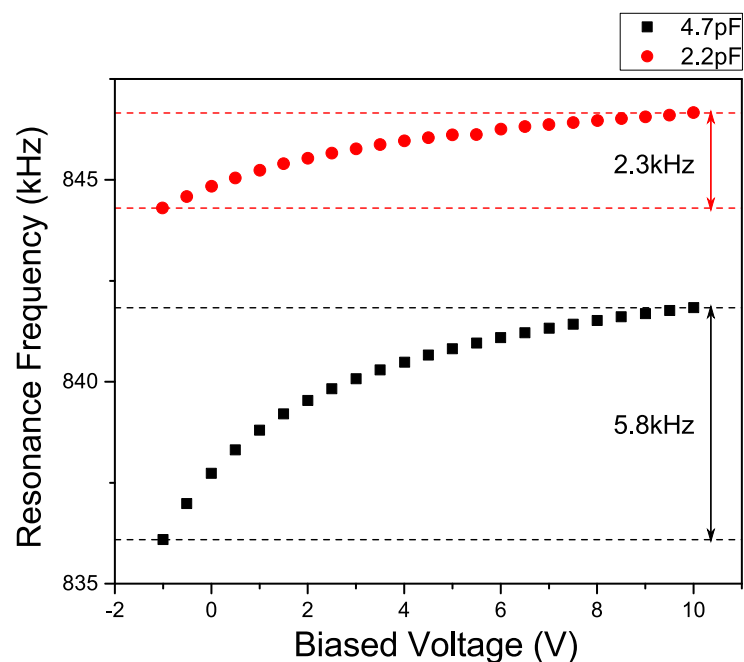


Figure 6.6 As the resonance frequency is dependent to the effective parallel capacitance, this shifts by the shift of the varactor capacitance which is tuned by the biased voltage. Therefore, the resonance frequency is also tuned as a function of bias voltage. The black points show the results of the 4.7pF coupling capacitance and the red dots show the results of the 2.2 pF.

From the result, the resonance frequency  $\nu_0$  varies by the varactor capacitance and the coupling capacitance. By comparing the value of  $\nu_0$ , the result of  $C_{in,v} = 4.7$  pF had a smaller value and wide range of the  $\Delta\nu_0$  than the case of  $C_{in,v} = 2.2$  pF. This is consistent to the Eq.(6.5). From the measurement, the capacitance of the varactor  $C_v$  varied from 7.6 pF to 0.1 pF by increasing

the varactor bias voltage from  $-1$  V to  $10$  V. This result is also consistent to the explanation of section 4.3.

In the case of the experiment, there are other components which possess additional parallel capacitance such as the trap, sapphire feedthroughs, etc.. Table 6.3 shows the results of the tuning range  $\Delta\nu_0$  measured by the test and the estimation including the other capacitances. By considering other capacitances, the resonance tuning range at both coupling capacitances wide enough to cover the minimum required axial frequency difference  $(\nu_{z,\bar{p}} - \nu_{H^-}) = 340$  Hz.

Table 6.3 The results of the varactor testing

$C_{in,v}$ (pF)	Tuning range $\Delta\nu_0$ (kHz)	estimated $\Delta\nu_0$ (kHz)
4.7	5.8	1.4
2.2	2.3	0.6

Next, the  $Q$ -value of the resonance was measured. From that result, the effective parallel resistance  $R_{eff,v}$  are evaluated as,

$$R_{eff,v} = 2\pi\nu_0 LQ \quad (6.6)$$

Figure 6.7 shows the results of the effective parallel resistance.

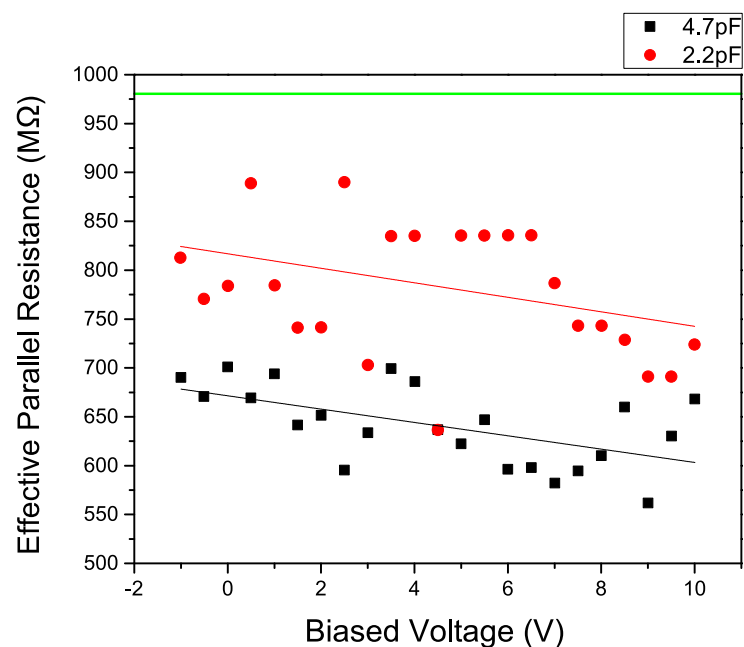


Figure 6.7 The effective parallel resistance of the circuit which resonator and varactor are connected parallel. The effective parallel resistance is decided by the measurement of resonance frequency and the  $Q$ -value as  $R_{eff} = 2\pi\nu_0 LQ$ . The black plots and line represent to the result of the 4.7 pF coupling capacitance and the red plots and lines are those of the 2.2 pF input capacitance. The red and black lines are the linear fitting of the effective parallel resistance and the green line is the parallel resistance of the resonator which the varactor is unloaded. Here the resolution is bad because of the bad resolution of the  $Q$ -value measurement, however a linear fitting slope of the  $R_{eff}$  were observed in both cases.

The effective parallel resistance of the resonator with the varactor is described as,

$$R_{eff,v} = \frac{R_p R_{p,v} \kappa_l^{-2} \kappa_{c,v}^{-2}}{R_p + R_{p,v} \kappa_l^{-2} \kappa_{c,v}^{-2}} \quad (6.7)$$

where  $R_{p,v}$  is the parallel resistance of the varactor and  $\kappa_{c,v}$  is the coupling factor due to the varactor

$$\kappa_{c,v} = \frac{C_{in,v}}{C_{in,v} + C_v}. \quad (6.8)$$

The results of Figure 6.7 can be interpreted by Eq.(6.7) and Eq.(6.8). When the coupling capacitance  $C_{in,v}$  is increased, the coupling factor  $\kappa_{c,v}$  increases and eventually  $R_{eff,v}$  decreases. This is shown as  $R_{eff,v}$  reduction of  $C_{in,v} = 4.7$  pF case comparing to 2.2 pF case. On the other hand, the negative slope of the  $R_{eff,v}$  is due to the decreased  $C_v$  which increases the coupling factor  $\kappa_{c,v}$ .

From the result of the effective parallel resistance, the dip width of the single antiproton can be

estimated as

$$\Delta\nu_{dip} = \frac{1}{2\pi} \frac{R_{eff}}{m_{\bar{p}}} \frac{q^2}{D^2} \quad (6.9)$$

where  $m_{\bar{p}}$  and  $q$  are mass and charge of the antiproton and  $D$  is the geometrical scale of the trap. Here the total effective parallel resistance  $R_{eff}$  is the resistance adding the parallel resistance of the amplifier  $R_{amp}$  to  $R_{eff,v}$ , in that case this will be as follows,

$$R_{eff} = \frac{R_{eff,v}R_{amp}/\kappa^2}{R_{eff,v} + R_{amp}/\kappa^2} \quad (6.10)$$

where  $\kappa$  is described by the coupling factor of the inductor and the amplifier's capacitance

$$\kappa = \kappa_l \kappa_c = \left( \frac{N_1}{N_1 + N_2} \right) \left( \frac{C_{in}}{C_{in} + C_{amp}} \right) \quad (6.11)$$

and the dip width is calculated as 5.7 Hz in 4.7 pF input capacitance and 6.1 Hz in 2.2 pF input capacitance, comparing to 6.5 Hz in the varactor unloaded case. In the table below the results and the evaluations are summarized.

Table 6.4 The results of the varactor testing

$C_{in,v}$ (pF)	Estimated $\Delta\nu_0$ (Hz)	$Q$ -value	$R_{eff,v}$ (M $\Omega$ )	dip width (Hz)
unloaded	-	61700	980	6.5
4.7	1.4	40800	640	5.7
2.2	0.6	49100	777	6.1

From these result, both 4.7 pF and 2.2 pF input capacitance are sufficient to tune the resonance. However when comparing the resistive loss, 2.2 pF input capacitance had a smaller result. From those reasons 2.2 pF is selected for the input capacitance.

### 6.3.2 Setup with the dummy trap

Next the resonator and the varactor was tested with a cylindrical dummy trap, of similar shape as the precision trap which is in the same way as the previous test. In this test the setup is similar to the actual experimental setup, therefore the information on the resonance frequency shift and the  $Q$ -value is important for the evaluation of the detection system whether it satisfies the requirement of the  $q/m$  measurement. For this measurement, the 2.2 pF coupling capacitance is used. The results of the test are shown in Figure 6.8 and Figure 6.9.

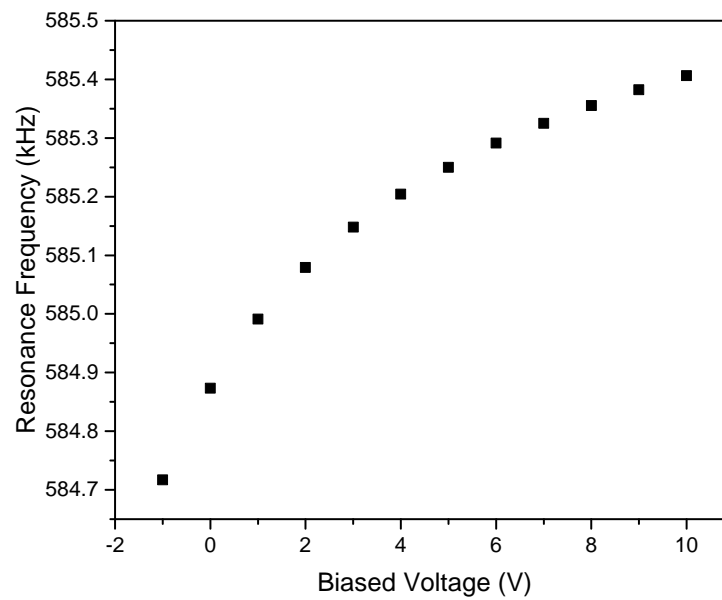


Figure 6.8 The resonance frequency shift by adjusting the biased voltage of the varactor installed with a dummy trap. As the parallel capacitance of the dummy trap, the resonance frequency decreased to 585kHz and the tuning range is 700 Hz, which is sufficient for the charge-to-mass ratio measurement.

The result of the resonance shift was  $\Delta\nu_z \approx 700$  Hz out of  $\nu_0 = 585$  kHz. This is more or less consistent with the calculation from the previous measurement as  $\Delta\nu_z \sim 600$  Hz. This shows that the result of the resonance frequency tuning range is consistent to the calculation and sufficient to the charge-to-mass ratio measurement. The  $Q$ -value is also measured as a function of the biased voltage. At this measurement an obvious linear scaling of a function of biased voltage was observed. Figure 6.9 shows the result of this measurement. Comparing to the previous measurement, the precision of this  $Q$ -value measurement improved by making rigid antennas and made a stable coupling between the RF lines and the resonator. From the results of the fitting, the  $Q$ -value and the effective parallel resistance scaled negatively, same as the measurement without the dummy trap.

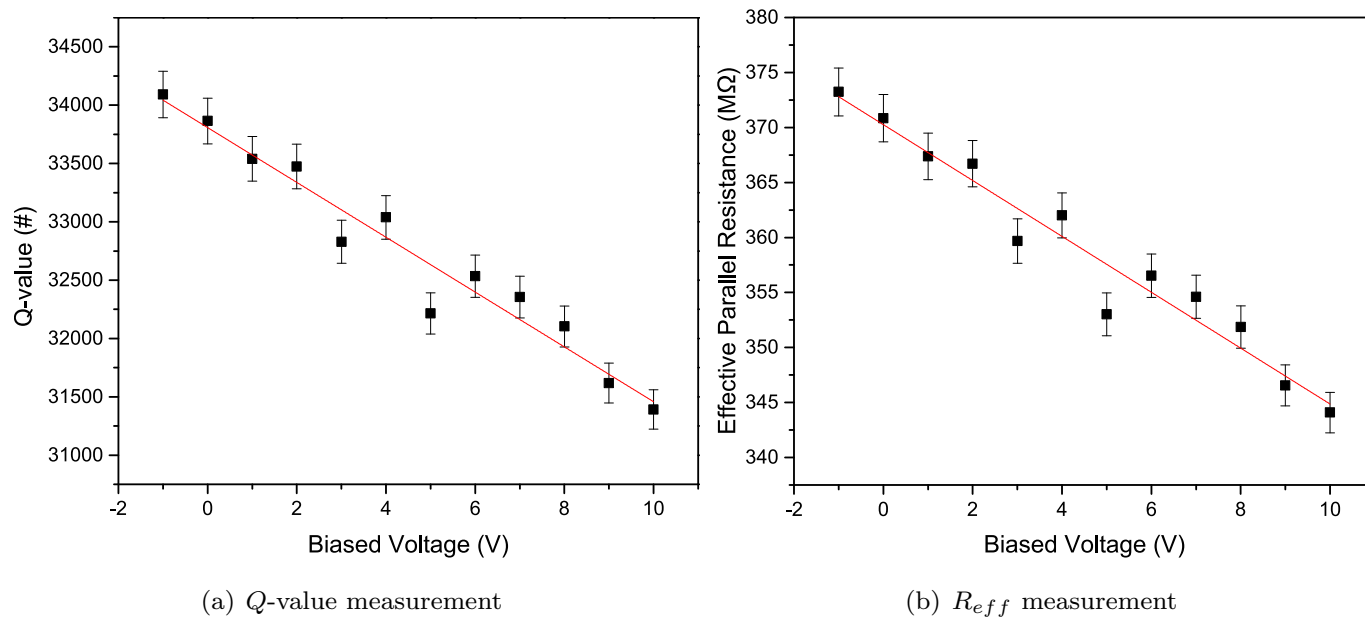


Figure 6.9 The (a)  $Q$ -value and (b) effective parallel resistance calculated from  $R = 2\pi\nu_0 LQ$  as a function of the varactor biased voltage. The red line is the linear fitting of the data points and this shows an obvious correlation between resistive loss and biased voltage.

## 6.4 Amplifier test

For the amplifier, GaAs dual-gate MES-FETs are used for the input and the output stage FET (See Figure 5.8). The idea of using MES-FETs which have dual-gates is for the reduction of the equivalent input noise such as  $1/f$  noise, since the gate lengths of the FET correlates to the equivalent input noise of the amplifier [54]. Moreover explained in the previous chapter, some previous researches show that the gate shorted dual-gate FETs function as single-gate FET with a doubled gate length, and thereby reduces the equivalent input noise [55]. To prove this effect, (a) a amplifier with a gate1-gate2 disconnected and gate2 grounded FET in the first stage, the "disconnected amplifier", and (b) a amplifier with a gate1-gate2 shorted FET in the first stage, the "shorted amplifier" were tested. Figure 6.10 shows the simple schematic of the shorted and disconnected amplifier.

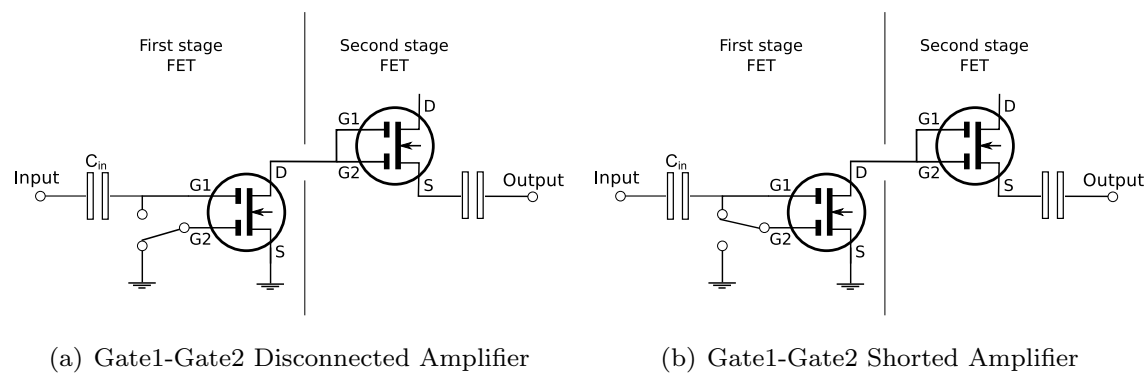


Figure 6.10 Simple schematic of the amplifier circuit with the Gate1-Gate2 disconnected and Gate2 grounded FET in the first stage as (a), and Gate1-Gate2 shorted FET as (b). At the second stage FET, both (a) and (b) have the shorted gate.

For the first stage two types of FETs, NE25139 (*NEC*) and 3SK164 (*SONY*) were tested, while CF739s (Infineon) were used for the second stage FET consistently. These amplifiers were tested in gate1-gate2 shorted and disconnected amplifiers. The values of the voltage adjusted to the amplifier were fixed in an optimum point of the amplifier gain and gate1 voltage is the variable, which is summarized in Table 6.5.

Table 6.5 The parameters of the voltage adjustment for the amplifier test.

Gate1[V]	Drain [V]	Source Follower Gate [V]	Source Follower Drain[V]
-1 ~ 0	3	1	3

The amplifier test is performed in two processes, first the measurement of the gain  $G_{amp}$  with a network analyzer (Figure 6.11), and second, the measurement of the equivalent input noise  $e_n$  with a spectrum analyzer (Figure 6.12). The amplifier gain in this context means the ratio of the increased output power by the amplifier compared to the input power. The gain is measured by adjusting the gate1 voltage to find an optimum point with the highest gain.

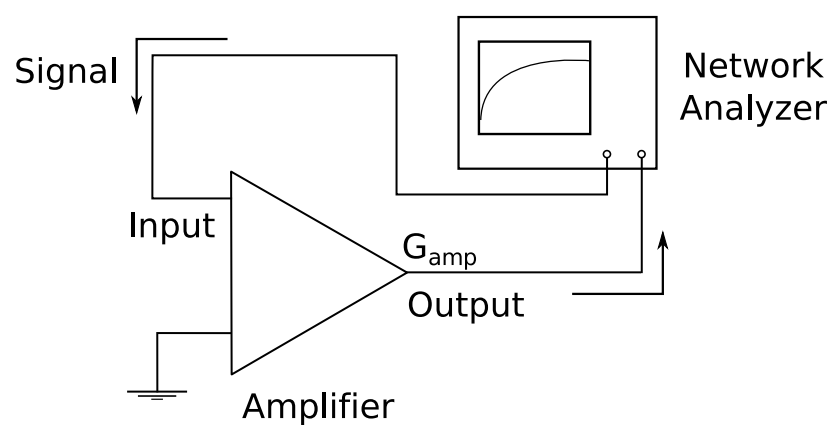


Figure 6.11 The gain measurement of the amplifier tested with a network analyzer. The network analyzer sends the signal to the amplifier and the output signal the gain  $G_{amp}$  is readout from the network analyzer.

The results of the highest gain and the adjusted gate1 is summarized in Table 6.6.

Table 6.6 The optimum gain of the amplifiers.

Amplifier	Gate1 Voltage [V]	$G_{amp}$ [dB]
NE25139 disconnected	-0.85	16.9
NE25139 shorted	-0.65	11.1
3SK164 disconnected	-0.60	14.5
3SK164 shorted	-0.40	13.9

The amplifier has two stages of FET, a common source input stage and a source follower output stage. Assuming that the equivalent input noise and the gain of the input FET as  $e_{n,1}$  and  $G_{n,1}$  and those of the output FET as  $e_{n,2}$  and  $G_{n,2}$ , the total amplified equivalent input noise is derived as

$$e_n^2 G_{amp}^2 = (e_{n,1}^2 G_{n,1}^2 + e_{n,2}^2) G_{n,2}^2 \quad (6.12)$$

As the output FET is a source follower FET, its gain is  $G_{n,2} = 1$ . Therefore, the gain of the whole amplifier can be assumed as equivalent to the gain of the input stage, and the equivalent input noise of the amplifier is derived as

$$e_n = \sqrt{e_{n,1}^2 + \frac{e_{n,2}^2}{G_{amp}^2}} \quad (6.13)$$

This equation shows that the lowest equivalent input noise is measured at the optimum point of the highest gain. For the measurement of the equivalent input noise of the amplifier itself, the input of

the amplifier is grounded by the connecting a  $50\Omega$  terminator to prevent the interference from the outer signal. The output of the amplifier is connected to the ZFL500LN amplifier (*Mini Circuits*) outside the coldhead to increase the signal in the amplitude of  $G_{ZFL} \approx 30$  dB. This amplified signal is then readout at the spectrum analyzer. Figure 6.12 shows the schematic of the equivalent input noise measurement of the amplifier.

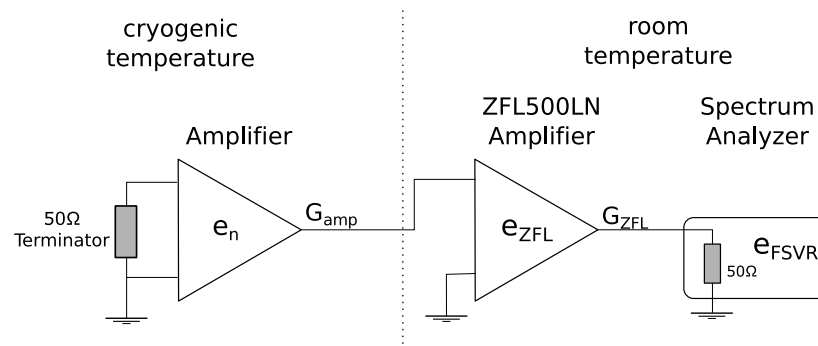


Figure 6.12 The equivalent input noise of the amplifier is tested with the  $50\Omega$ , the ZFL500LN amplifier and the spectrum analyzer. The equivalent input noise of the amplifier  $e_n$  is first amplified by the amplifier gain  $G_{amp}$ . Next, the amplified signal  $e_n G_{amp}$  is transmitted to the ZFL500LN amplifier with an additional equivalent input noise  $e_{ZFL}$ , then the signal is amplified by  $G_{ZFL}$ . When the signal arrives to the spectrum analyzer, its equivalent input noise  $e_{FSVR}$  is added. Eventually the total noise can be described as Eq.(6.14).

From this measurement, the total equivalent input noise  $e_{tot}[\text{nV}/\sqrt{\text{Hz}}]$  of the setup is measured. The equivalent input noise of the amplifier  $e_n$  is extracted by the following equation,

$$e_{tot}^2 = (e_n^2 G_{amp}^2 + e_{ZFL}^2) G_{ZFL}^2 + e_{FSVR}^2 \quad (6.14)$$

which  $G_{amp}$  and  $G_{ZFL}$  are the gain of the amplifier and the ZFL amplifier,  $e_{ZFL}$  and  $e_{FSVR}$  are the equivalent input noise of the ZFL amplifier and the spectrum analyzer. From the results of  $G_{amp}$ ,  $e_{tot}$  and individual measurements of  $e_{ZFL}$ ,  $G_{ZFL}$  and  $e_{FSVR}$ , the equivalent input noise of the amplifier  $e_n$  is extracted. The table below shows the result of the highest gain and the lowest equivalent input noise of the NE25139 amplifier and 3SK164 amplifier in gate1-gate2 shorted and disconnected circuit. These data are the results at the 600kHz frequency measurement.

Table 6.7 The table of the gain and equivalent input noise of the amplifier at 600 kHz.

Amplifier	Gate1 Voltage [V]	$G_{amp}$ [dB]	$e_n$ [nV/ $\sqrt{\text{Hz}}$ ]
NE25139 disconnected	-0.85	16.9	0.94
NE25139 shorted	-0.65	11.1	0.72
3SK164 disconnected	-0.60	14.5	0.88
3SK164 shorted	-0.40	13.9	0.51

From these results, the shorted amplifier had a reduction of the gain compared to the disconnected circuit. However it had a lower equivalent input noise, which is consistent to the previous research [55]. Especially the 3SK164 shorted amplifier had the lowest equivalent input noise  $e_n = 0.51\text{nV}/\sqrt{\text{Hz}}$  with a sufficient gain, this amplifier is used for the the tunable axial detection system. This is also an improvement from the previous development [50], which had the lowest equivalent input noise as  $e_n = 0.7\text{ nV}/\sqrt{\text{Hz}}$  in 600 kHz.

To discuss the physical interpretation of the equivalent input noise further, the results need to be considered in details. Figure 6.13 shows the equivalent input noise of amplifiers as a function of frequency.

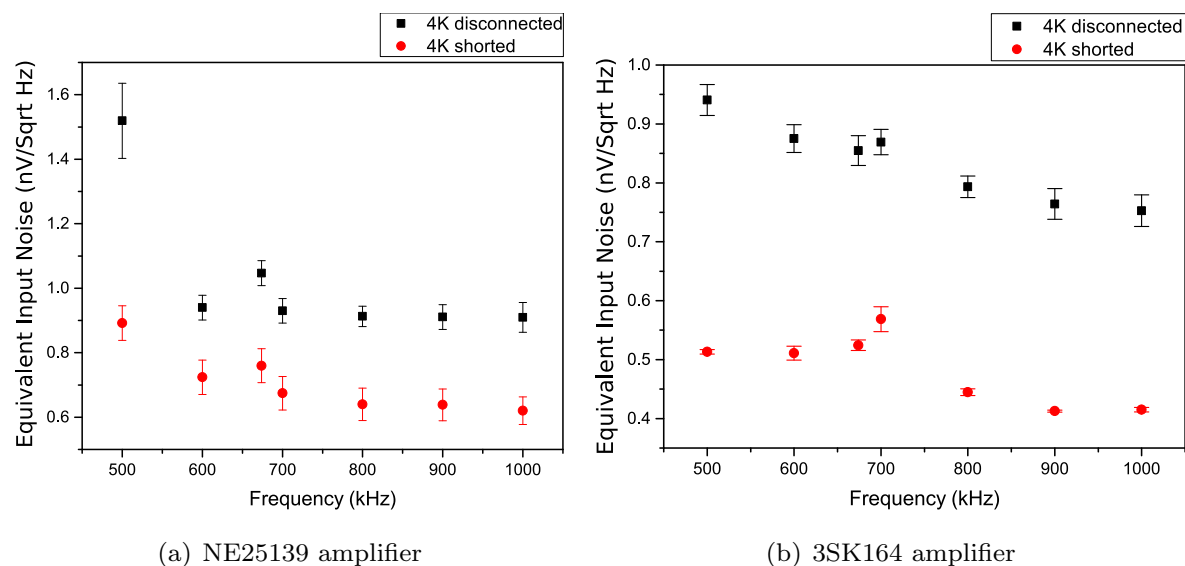


Figure 6.13 The results of the equivalent input noise measurement as a function of frequency from 500kHz to 1MHz in cryogenic temperature. (a) is the result of the amplifier using NE25139 FETs and (b) is that of using 3SK164 FETs. The black dots are the results of the Gate1-Gate2 disconnected amplifier and red dots are the results of the Gate1-Gate2 shorted amplifier.

There are several noise sources for GaAs MES-FETs: thermal noise, shot noise due to the gate

leakage current, generation-recombination noise (GR noise) in the depletion region, and the 1/f noise due to the drain current [55]. As the FET is tested in cryogenic temperature, the shot noise becomes negligible, and, GR noise and 1/f noise become dominant. The GR noise is expressed as

$$S_{GR} = 4kT \sum_i \frac{\rho_{GR}(\tau_i/\tau_0)}{1 + (2\pi f)^2 \tau_i^2} \quad (6.15)$$

where  $\rho_{GR}$  is effective resistance depending inversely on the gate area, and directly on the deep-level trap concentration in the depletion region,  $\tau_i$  is the characteristic time constant of the  $i$ th trap and  $\tau_0$  is a normalizing value [57]. The importance of this equation is that GR noise scales to the temperature and the effective resistance  $\rho_{GR}$  related to the depletion region. The 1/f noise is generated by the Drain-Source current of the FET which scales inverse to the frequency and can be expressed as

$$S_{1/f} = \frac{q\mu_n\alpha_H I_D V_{DS}}{g_m^2 L^2} \frac{1}{f} = A_f \frac{1}{f} \quad (6.16)$$

[55][56][57]. The coefficients are discussed in previous chapter. From the interconnection of the gates of the FET, the amplifier can be recognized as the gate length doubled, and applying to Equation (6.16), the noise density due to 1/f noise  $S_{1/f}$  and the constant  $A_f$  is assumed to be as one fourth of those of disconnected amplifier. Generally, the equivalent input noise  $e_n$  will be described by the spectral power density of the GR noise  $S_{GR}$  [V<sup>2</sup>/Hz] and the spectral power density of 1/f noise  $S_{1/f}$  [V<sup>2</sup>/Hz] as

$$\begin{aligned} e_n^2 &= S_{GR} + S_{1/f} \\ &= S_{GR} + A_f S_{1/f}. \end{aligned} \quad (6.17)$$

The results are fitted by this equation as a function of the frequency and Figure 6.14 and Table 6.8 shows the result of the square root of the equivalent input noise and the fitted result.

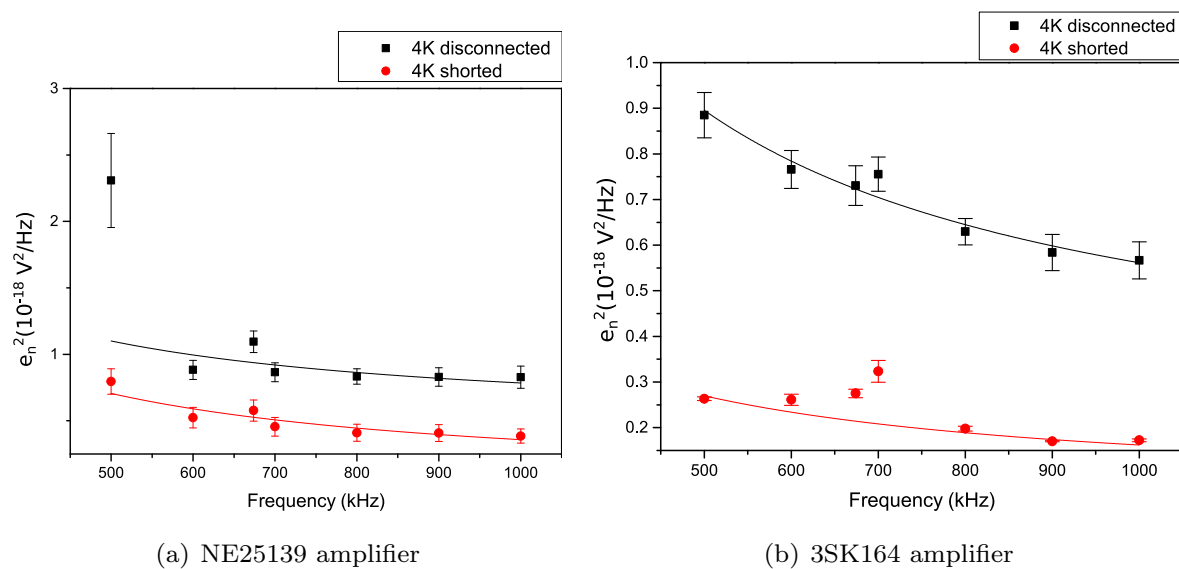


Figure 6.14 The noise spectral power density  $e_n^2$  are extracted from the results of equivalent input noise in the range from 500 kHz to 1 MHz. (a) is the result of NE25139 amplifier and (b) is the result of 3SK164 amplifier. The black dots are the result of the Gate1-Gate2 disconnected amplifier and red dots are the result of the Gate1-Gate2 shorted amplifier. The lines are the fitting lines based on constant GR noise and the  $1/f$  noise scales inverse to the frequency.

Table 6.8 The fitting results of the equivalent input noise measurement.

Amplifier	$S_{GR}[10^{-18}\text{V}^2/\text{Hz}]$	$A_f[10^{-12}\text{V}^2]$
NE25139 disconnected	0.46(0.34)	0.316(0.255)
NE25139 shorted	0.010(0.096)	0.348(0.071)
3SK164 disconnected	0.227(0.052)	0.334(0.037)
3SK164 shorted	0.053(0.024)	0.108(0.019)

From the results of Figure 6.14, the fitting shows that the GR noise factor of the equivalent input noise reduced about  $0.3 \sim 0.4 \text{ nV}/\sqrt{\text{Hz}}$  by shorting the gates. Moreover, the correlation of the  $1/f$  noise in the 3SK164 amplifier had a reduction of  $1/3$  by the shorting of the gates. Since data points are few to have a proper fitting and the  $1/f$  noise is rather dominant in low frequency ( $\sim 300 \text{ kHz}$ ), it is hard to characterize completely of the equivalent input noise from these data sets. However, still this result shows the effect of noise reduction by shorting the gates.

## 6.5 Test of the the axial detection system

For the final measurement, the whole setup of the tunable axial detection system is tested. Figure 6.15 shows the full setup of the tunable axial detection system, composed of the superconducting resonator, the varactor and the amplifier. In this measurement, the dummy trap, the copper housing resonator, the varactor with  $C_{in,v} = 2.2$  pF coupling capacitance, and the 3SK164 shorted amplifier with  $C_{in} = 6.8$  pF were used.

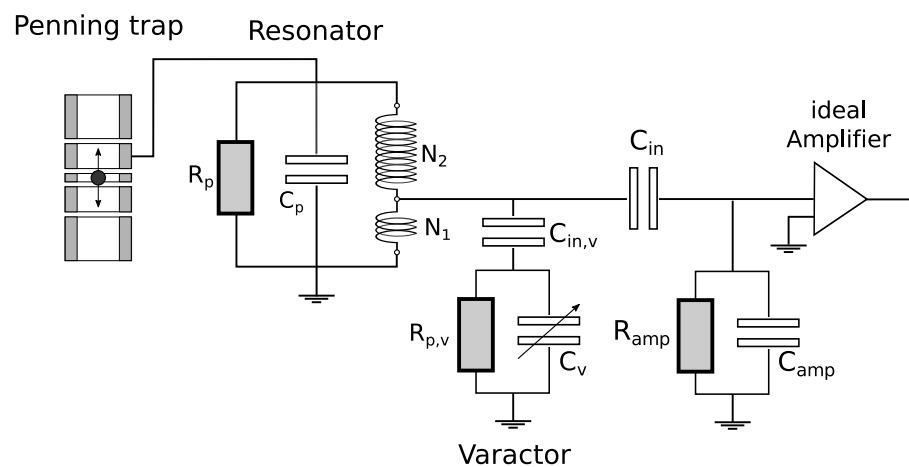


Figure 6.15 The equivalent circuit of the tunable axial detection system.

The adjusted parameter of the biased voltage is at the table below.

Table 6.9 The parameter of the biased voltage.

Varactor Bias [V]	Gate1 [V]	Drain [V]	Source Follower Gate [V]	Source Follower Drain [V]
-1 ~ 10	-1~0	3	1	3

At the measurement, first the amplifier was tested to measure the resonance frequency  $\nu_0$ ,  $Q$ -value and the signal-to-noise ratio (SNR). This measurement was performed with the condition that the varactor is unbiased. After searching the optimum tuning point of the amplifier with the highest signal-to-noise ratio, the varactor was tested to measure the shift of the resonance frequency  $\Delta\nu_0$  and the  $Q$ -value.

### 6.5.1 Amplifier analysis

The measurement of the resonance frequency and the  $Q$ -value were measured in the same way as the evaluation of the resonator. The measurement of the signal-to-noise ratio, which is defined by

the power of the signal  $P_S$  [W] and the power of the noise  $P_N$  [W] as

$$SNR = \frac{P_S}{P_N} \quad (6.18)$$

was measured by from the spectrum analyzer. Figure 6.16 shows the setup for the signal-to-noise measurement.

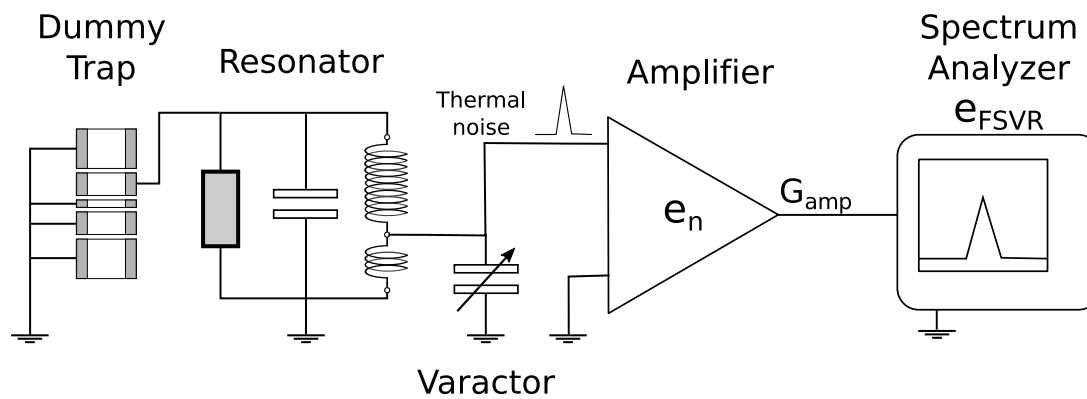


Figure 6.16 The setup of the signal-to-noise ratio measurement. In this setup, the thermal noise induced by the resonator is amplified by the amplifier, and the amplitude is measured by the spectrum analyzer. Thereby, the power of the signal  $P_S$  [dB] and the noise level  $P_N$  [dB] are measured, and signal-to-noise ratio  $[SNR]_{dB} = P_S - P_N$  is decided.

Figure.6.17 is the broad and rough screenshot of the thermal noise shifting by the gate1 voltage adjustment. From this screenshot, the highest signal-to-noise ratio is obtained at gate voltage  $V_G = -0.5V$ .

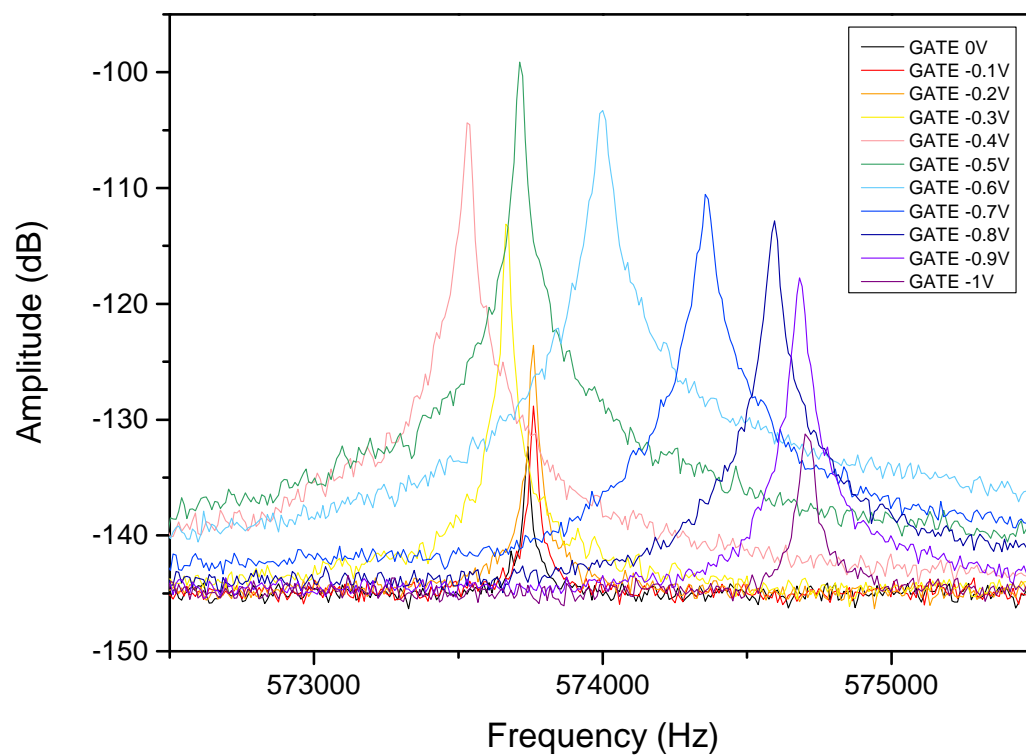


Figure 6.17 The resonance shift by adjusting the gate voltage of the amplifier. The noise level is around -140 dB and the peak is sensitive to the gate voltage. The highest SNR was observed in  $V_G = -0.5$  V. The results of the SNR measurement in higher resolution are shown in Figure 6.20.

The signal-and-noise ratio also can be calculated by the information of the effective parallel resistance ( $R_{eff}$ ) and the equivalent input noise ( $e_n$ ). In this experimental setup, the power of the signal can be expressed as

$$P_S = \frac{\Delta B}{R} (4k_B T R_{eff} \times \kappa^2 \times G_{amp}^2 + e_{FSVR}^2) \quad (6.19)$$

where  $R$  is the input impedance of the spectrum analyzer,  $\Delta B$  is the bandwidth of the input filter inside the analyzer,  $k_B$  is the Boltzmann constant,  $T$  is the temperature,  $\kappa$  is the coupling factor of the detection system,  $G_{amp}$  is the gain of the amplifier, and  $e_{FSVR}$  is the equivalent input noise of the spectrum analyzer, respectively. On the other hand the noise level is decided by the equivalent input noise of the amplifier and the spectrum analyzer as

$$P_N = \frac{\Delta B}{R} (e_n^2 \times G_{amp}^2 + e_{FSVR}^2). \quad (6.20)$$

When  $G_{amp}$  is large enough that  $e_{FSVR}$  can be negligible, the signal-to-noise ratio [dB] can be calculated from  $R_{eff}$  and  $e_n$  as

$$\begin{aligned} [SNR]_{dB} &= 10 \log_{10} \left( \frac{P_S}{P_N} \right) \text{ [dB]} \\ &\simeq 20 \log_{10} \left( \frac{\sqrt{4k_B T R_{eff}} \times \kappa_l \kappa_c}{e_n} \right) \text{ [dB]} \end{aligned} \quad (6.21)$$

where  $\kappa_l$  and  $\kappa_c$  is the coupling factor due to the inductor and the capacitance of the amplifier. These values are fixed as  $\kappa_l = 0.24$  and  $\kappa_c = 0.86$  in this measurement. Figure 6.18 shows the result of the  $Q$ -value measurement and the effective parallel resistance. The reduction below  $-0.4$  V is considered as a dominated effect of the positive feedback of the amplifier.

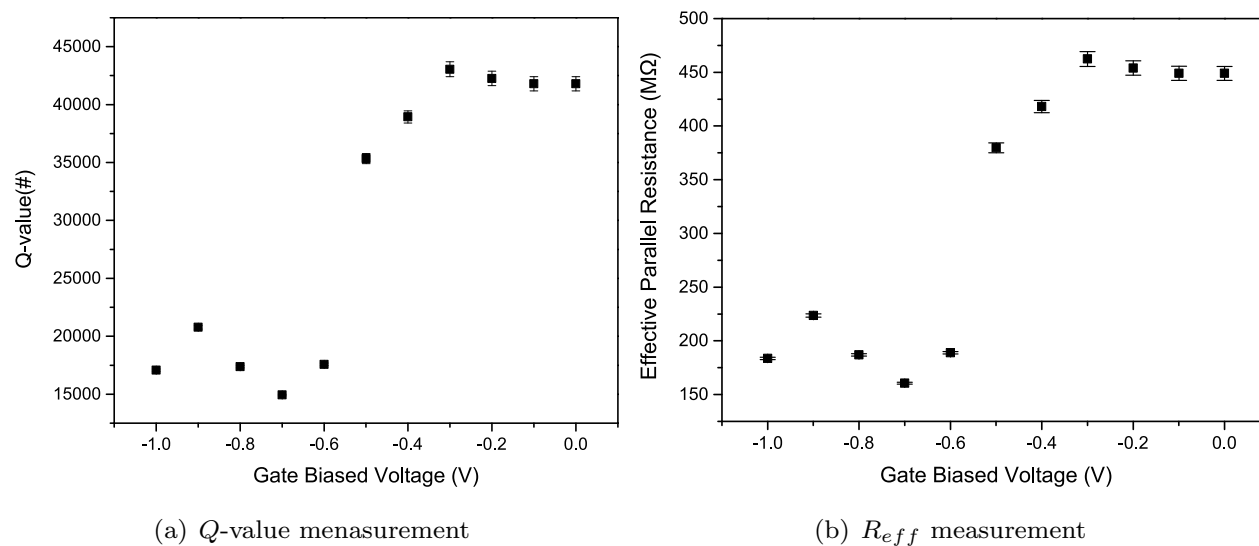


Figure 6.18 The results of the  $Q$ -value measurement and the effective parallel resistance as  $R_{eff} = 2\pi\nu_0 LQ$ .

Regarding the equivalent input noise, Figure.6.19 shows the results by an independent measurement. Together with the  $R_{eff}$  results, the calculated value of the signal-to-noise measurement is shown in Figure.6.20.

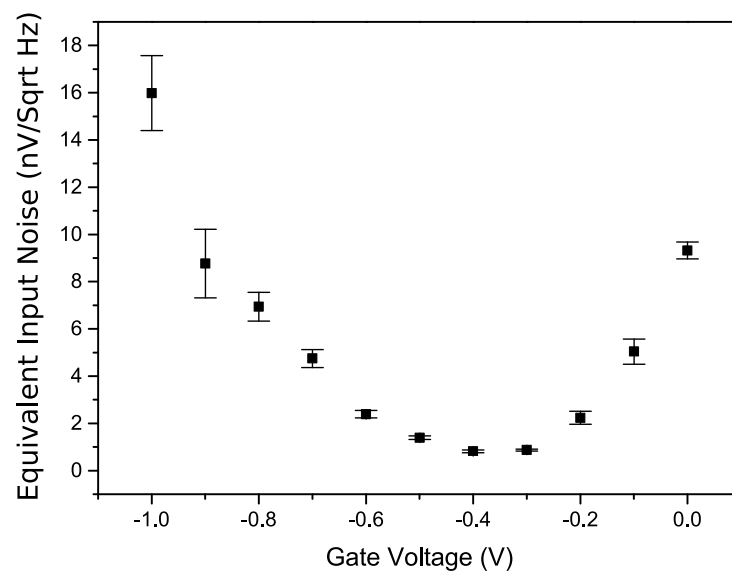


Figure 6.19 The equivalent input noise of the amplifier as a function of gate voltage. Here the 3SK164 amplifier with gate1-gate2 shorted is used.

The SNR which is measured directly by the spectrum analyzer and calculated by the result of the equivalent input noise  $e_n$  measurement shown in Figure 6.20.

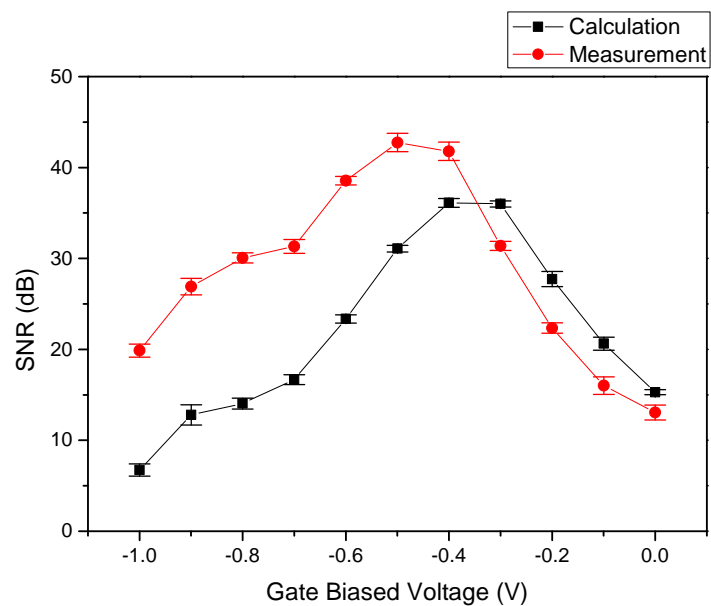


Figure 6.20 The signal-to-noise ratio (SNR) shift by the amplifier by adjusting the gate Biased Voltage. The black plots are the calculated value from the results of  $Q$ -values and the equivalent input noise of the amplifier. The red line is the measured value directly from the spectrum analyzer. The dropping at the calculation value is due to the  $Q$ -value drop which is due to the positive feedback from the amplifier.

At the calculation the declining value is due to the reduction of the  $Q$ -value, which is the effect from the positive feedback of the amplifier. The effective temperature of the amplifier is assumed as  $T = 2.8\text{K}$  from the calculation, which is measured by the thermometer. However from the result of the SNR direct measurement, the effective temperature was extracted as  $5(2)\text{ K}$  at gate1 voltage  $-0.4\text{V}$ . In BASE we have consistently measured resonator temperatures which are about a factor of 1.5 above the physical temperature. The  $5\text{K}$  temperature which is achieved here is by about a factor of 1.75 higher than the physical temperature, which has yet to be understood. However, this particle temperature with this detection system is still acceptable for the experiment. From this result, the axial frequency can obtain a high signal-to-noise ratio with maintaining a high  $Q$ -value at the gate1 voltage from  $-0.4\text{ V}$  to  $-0.5\text{ V}$  and the optimum point was  $SNR = 43\text{dB}$  with the  $Q$ -value of 41500, at  $V_{G1} = -0.47\text{ V}$ . This result is improved from the previous development of the axial detection system [50] which recorded  $SNR = 34.5\text{ dB}$  at a  $Q$ -value of about 21000.

### 6.5.2 Varactor analysis

The varactor was tested with the optimum point of the amplifier, at gate1 voltage  $-0.47\text{ V}$ . The measurement is done at the same routine as the previous section. Figure 6.21 shows the result of the resonance frequency shift  $\Delta\nu_0$ . From this result, the resonance frequency decreased to  $\nu_0 = 578\text{ kHz}$  by the effect of the amplifier's parallel resistance. However the tuning range was still  $\Delta\nu_0 = 680\text{Hz}$  and it is sufficient to the charge-to-mass ratio measurement.

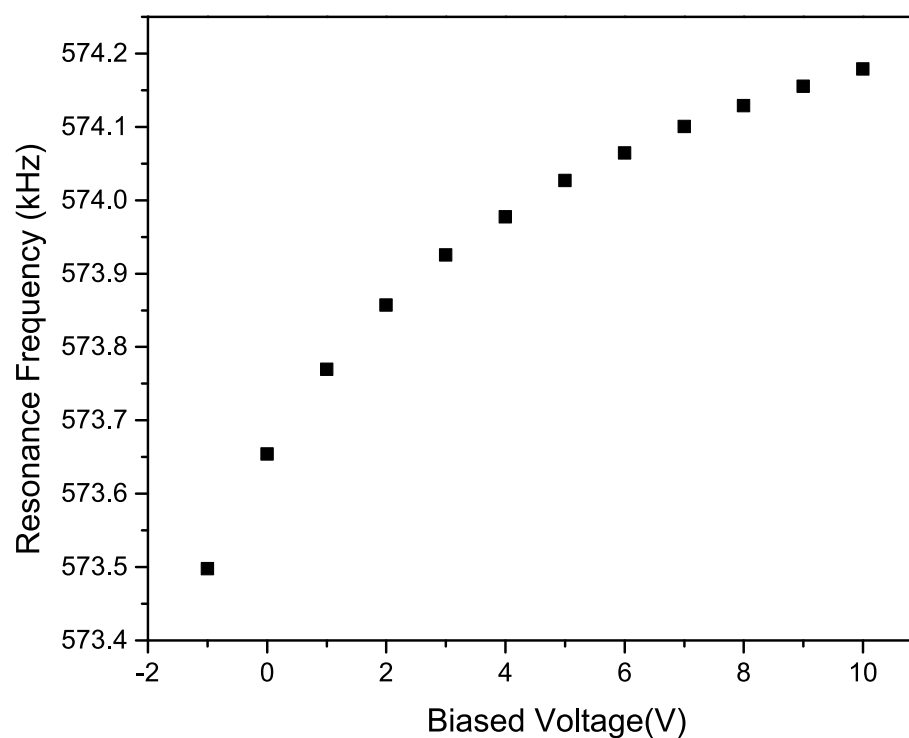


Figure 6.21 The resonance frequency shift by the varactor tuning at the whole setup of the tunable axial detection system. Compared to the result without the amplifier the resonance frequency dropped  $\sim 1.3$  kHz, however still the resonance shift is  $\Delta\nu_0 = 680$  Hz and sufficient to the charge to mass ratio measurement.

The  $Q$ -value measurement and effective parallel resistance is measured in the same routine. From the results in Figure.6.22, also the clear linear scaling was observed in the measurement of  $Q$ -value and effective parallel resistance.

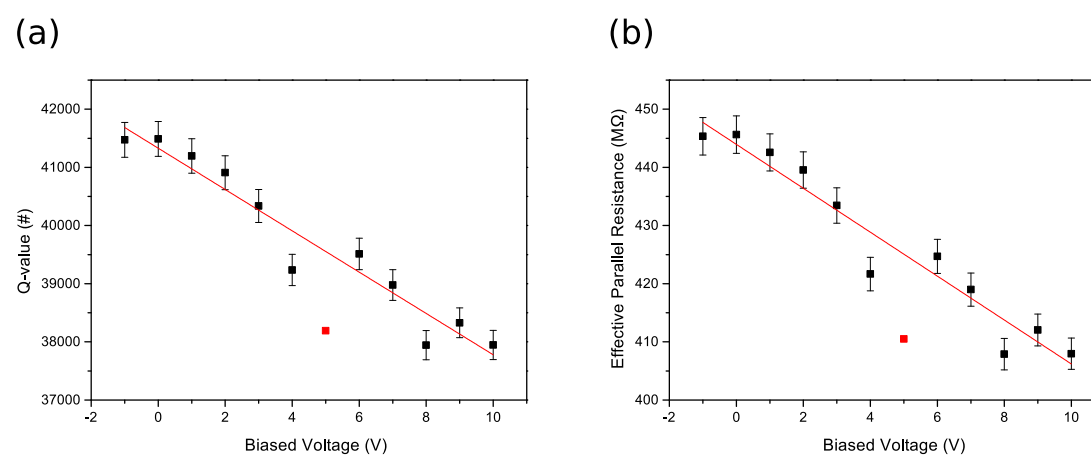


Figure 6.22 (a)  $Q$ -value and the (b) effective parallel resistance shift which is tested with the resonator and the dummy trap. Both figures (a) and (b) shows a linear correlation of  $Q$ -value and effective parallel resistance as a function of the biased voltage. The red line is the linear fitting line and red dots are the excluded points at the fitting.

From the result of the effective parallel resistance in Figure.6.22, the dip width is estimated as 10.9Hz in -1V biased voltage and 10.0Hz in 10V biased voltage. This dip line width is rather large compared to the value (1.5Hz) which is usually used in BASE experiment. However, it is the result of several components coupled to the unperturbed detector and means practically, that the losses of the components are small enough to operate the detector at even such high cooling efficiency. The line width can be easily reduced by an application of feedback cooling or the  $Q$ -tuning, which was recently developed by BASE [49]. The signal-to-noise ratio measurement was also performed by adjusting the varactor bias voltage in the amplifier optimum working point. The value was stable around 43 dB.

The ability of tuning range and the sufficient  $Q$ -values are positive improvements by tuning axial detection system. However the  $Q$ -value and the effective parallel resistance scales to the biased voltage, which can affect to the precision of the charge-to-mass ratio measurement. To know the significance of this effect, this requires further evaluation.

## Chapter 7

# Conclusions and overview

In this thesis, a new design of an axial detection system is introduced for the improved measurement of the proton-to-antiproton charge-to-mass ratio. In the previous measurement performed by BASE [13], the major systematic uncertainties were caused by the different tuning parameters in the Penning trap for the antiproton and the  $\text{H}^-$  ion, to fix each axial frequency to the resonance of the axial detection system. The idea of the new axial detection system is to make the resonance frequency tunable to the axial frequencies for each particle. By this strategy, the charge-to-mass ratio can be measured without tuning the voltage potential. Therefore the 26 p.p.t. systematic uncertainty out of 69 p.p.t. total uncertainty [13] will be dramatically suppressed and will contribute to the improvement of the precision.

To install this tunable axial detection system to the main experiment, I have tested and characterized the potential limitations and evaluated whether this meets the requirements for the charge-to-mass ratio measurement. In the cryogenic test of the tunable axial detection system, the tuning range of the resonance frequency  $\Delta\nu_0 = 680$  Hz out of  $\nu_0 = 578$  kHz was recorded. This is sufficient for the axial frequency measurement of the antiproton and the  $\text{H}^-$  ion, which requires a tuning range  $\Delta\nu_0 = 340$  Hz. This indicates that the new tunable axial detection system satisfies the requirement of the charge-to-mass ratio of the BASE measurement.

Moreover, other optimizations of the new axial detection system were performed. To solve the thermalization problem, the material of the housing was replaced from NbTi to OFE copper and recorded less  $Q$ -value loss and sufficient results to install in the main experiment. On the level of the cryogenic amplifier, optimizations are performed to improve the noise level from the previous development [50]. Shorting gates in the input stage FET made a reduction of equivalent input noise from  $0.65$  nV/ $\sqrt{\text{Hz}}$  to  $0.51$  nV/ $\sqrt{\text{Hz}}$ . As the equivalent input noise reduced, also a higher signal-to-noise ratio  $SNR = 43.0$  dB with a high  $Q$ -value of 41500 were obtained, improved from  $SNR = 34.5$  dB with a  $Q$ -value of 21000.

---

From these results, the new tunable detection system has a clear improvement and has also the potential to be installed to the main experimental setup. This upgrade will be implemented in one of the future BASE charge-to-mass ratio comparisons, and therefore the developments made in this thesis will contribute to improve in one of the future runs the fractional precision in this important number.

# Bibliography

- [1] P. A. M. Dirac, Proc. R. Soc. Lond. A **117** (1928).
- [2] M. Dine and A. Kusenko. Rev. Mod. Phys. **76**(1) (2003).
- [3] B. Schwingenheuer et al., Phys. Rev. Lett. **74** 4376 (1995).
- [4] K. A. Olive et al., Chin. Phys. C **38**, 090001 (2014).
- [5] R. S. Van Dyck et al., Phys. Rev. Lett. **59** 26 (1987).
- [6] H. Dehmelt et al., Phys. Rev. Lett. **83**, 4694 (1999).
- [7] G. W. Bennett et al., Phys. Rev. D **73**, 072003 (2006).
- [8] G. W. Bennett et al., Phys. Rev. Lett. **100**, 091602 (2008).
- [9] H. Davoudiasl et al., Phys. Rev. D **89**, 095006 (2014).
- [10] N. Arkani-Hamed et al., Phys. Rev. D **79**, 015014 (2009).
- [11] J. Grange et al., arXiv:1501.06858 [physics.ins-det], (2015).
- [12] T. Mibe et al., Chin. Phys. C **34**, 745 (2010).
- [13] S. Ulmer, et al., Nature **524**, 196 (2015).
- [14] G. Gabrielse et al., Phys. Rev. Lett. **82**, 3198 (1999).
- [15] G. Gabrielse et al., Phys. Rev. Lett. **74**, 3544 (1995).
- [16] J. K. Thompson et al., Nature **430**, 58 (2004).
- [17] G. Gabrielse et al. Int. J. Mass Spectr. **251**, 273 (2006).
- [18] S. Maury, Hyp. Int. **109**, 43-52 (1999).
- [19] C. G. Parthey et al., Phys. Rev. Lett. **107**, 203001 (2011).
- [20] M. Ahmadi et al., Nature, Accelerated Article Preview, published online in 19th December 2016.
- [21] L. Essen et al., Nature **229**, 110 (1971).
- [22] C. Amole et al., Nature **483**, 439 (2012).
- [23] N. Kuroda et al., Nature Comm. **5**, 3089 (2014).
- [24] A. Mooser, et al., Physics Letters B **723**, 78-81(2013).
- [25] A. Mooser, et al., Nature **509**, 596 (2014).
- [26] C. Smorra et al., The European Physics Journal volume **224**, number 16, November (2015).

- [27] H. Dehmelt and P. Ekström, *Bull. Am. Phys. Soc.* **18**, 72 (1973).
- [28] D. J. Wineland and H. G. Dehmelt, *J. Appl. Phys.* **46**, 919 (1975).
- [29] H. Takashi, High precision measurement of the cyclotron frequency of the single-trapped antiproton. Master thesis, The University of Tokyo (2015)
- [30] G. Gabrielse et al., *Int. J. Mass Spec.* **88**, 319 (1989)
- [31] S. Ulmer et al., *J. Phys. Conf. Ser.* **488**, 012033 (2014).
- [32] C. C. Rodegheri et al., *N. J. Phys.* **14**, 063011 (2012).
- [33] G. Gabrielse et al., *Phys. Rev. Lett.* **63**, 1360 (1989).
- [34] C. Smorra et al. *Int. J. Mass Spectrom.* **389**, 10 (2015).
- [35] A. Mooser et al., *Phys. Rev. Lett* **110**, 140405 (2013).
- [36] S. Ulmer, First Observation of Spin Flips with a Single Proton Stored in a Cryogenic Penning Trap, Ph.D thesis, University of Heidelberg (2011).
- [37] G. Shneider, Development of a Penning trap system for the high precision measurement of the antiprotons magnetic moment, Master thesis, Mainz University (2014).
- [38] H. Nagahama, *Rev. Sci. Instrum.* **87**, 113305 (2016).
- [39] L. S. Brown and G. Gabrielse, *Phys. Rev. A* **25**, 2423 (1982).
- [40] L. S. Brown and G. Gabrielse, *Rev. Mod. Phys.* **58**, 233 (1986).
- [41] S. Ulmer et al., *Phys. Rev. Lett.* **107**, 103002 (2011).
- [42] E. A. Cornell et al., *Phys. Rev. A* **41**, 312 (1990).
- [43] L. S. Brown, *Phys. Rev. Lett.* **52**, 2013 (1984).
- [44] L. S. Brown, *Ann. Phys.* **159**, 62 (1985).
- [45] S. Sturm. et al., *Nature* **506**, 467-470 (2014).
- [46] C. G. Parthey. et al., *Phys. Rev. Lett.* **107**, 203001 (2011).
- [47] A. K. Bhatia, R.J. Drachmann, *J. Phys. At. Mol. Opt. Phys.* **27**, 1299-1305 (1994).
- [48] J. K. Thompson, S. Rainville, D.E. Pritchard, *Nature* **430**, 58-61 (2004).
- [49] H. Nagahama, Ph.D thesis submitted in December 2016, University of Tokyo
- [50] H. Nagahama, Development of Low Noise Electronics for the Measurement of the Magnetic Moment of the Antiproton, Master Thesis, University of Tokyo (2014).
- [51] S. Ulmer, First Observation of Spin Flips with a Single Proton Stored in a Cryogenic Penning Trap, Ph.D thesis, University of Heidelberg (2011).
- [52] Y. Shapira, L. J. Neuringer, *Phys. Rev. A* **140**, 1638.
- [53] R. N. V. Nyugen, Bachelor Thesis at Massachusetts Institute of Technology (1998) .
- [54] R.K. Kirshman, J.A. Lipa *SPIE Vol. 1946 Infrared Detectors and Instrumentation*, 350-364 (1992).
- [55] A. Alessandrello, et al., *Nuclear Instruments and Methods in Physics Research, A* **289**, 426-437

- (1990).
- [56] F. H. Hooge, Phys. Lett A **29** 139 (1969).
- [57] M. B. Das, Proc.Symp .on Low Temperature Electronics and High T, Superconductors, vol.**88-9** p.464 Electrochemical Soc.,New Jersey (1988).
- [58] P. Horowitz and W. Hill, The Art of Electronics, Cambridge University Press; 2nd edition (1989).
- [59] A. Lee, Rev. Sci. Inst. **64**, 2373 (1993).
- [60] A. Robinson, V. Talyanskii, Rev. Sci. Inst. **75**, 3169 (2004).
- [61] Rogers corporation, RT/duroid 5870/5880 data sheet.

# Acknowledgement

修士課程の間にお世話になった全ての方々に対して、この場を借りて深く感謝いたします。指導教員の松田恭幸准教授には学部三年の頃からお世話になっていました。修士課程で研究室に配属されたのちは CERN の BASE 国際共同グループに関わる機会を与えてくださり、感謝しております。また研究、進路やプライベートに関する相談にも親身に接していただきました。CERN での研究活動と修士論文を最後までやり遂げられたのはそんな先生の支えがあったからこそだと考えております。鳥居寛之助教は、日本での放射線に関する手続きに関してのサポートをしていただきました。またご自身の放射線教育の講義にも招待していただき、大変勉強になりました。黒田直史助教は、CERN での生活に関する知識を教えてください、また ASACUSA のミーティングにも参加する機会を与えていただきました。

先輩である田中香津生博士、神田聡太郎博士、田島美典さん、石川彰一郎さん、小林立人さん、上野恭裕さん、東芳隆さんからは、右も左もわからなかった僕に対して様々なことを優しく指導していただき、会話や議論から多くの知見を頂きました。また博士から MuSEUM 実験に移行する際に、下村浩一郎准教授、神田博士、上野さんには早期から相談に乗っていただき、大変お世話になりました。同期の松館拓也くんとは、僕が CERN に滞在していたときに日本での手続きから下らない話まで付き合ってくれて、CERN での研究生活をする上での大変心強く感じました。実験グループと研究内容は異なるものの、お互いに切磋琢磨し合える友に出会えて良かったと思っております。後輩の瀬尾俊くん、八木大介くんには、帰国の際に日々彼らの成長を感じ、良い刺激を受けるようになりました。理化学研究所の和田ひとみ様、森田めぐみ様、倉持千加子様、そして山崎泰規博士には、理研研修生としての手続きや CERN 出張の手配、そして一年間にも及ぶ CERN での生活支援にご尽力くださいました。

During my master term, I was going back and forth between CERN and Japan. This was not possible without support by all of the the BASE member. I would like to thank first to Dr Stefan Ulmer, the team leader of the BASE collaboration. Thank you for giving me the opportunity and the financial support to participate in BASE. You also suggest me a exciting theme for my master project and give me many constructive comments about my thesis, even until the end of the submission date. I was also impressed that how eager you are devoting to the experiment. I would also like to thank to Dr Christian Smorra. Your kindly and humous character were impressive and

make me easy and to join in BASE. And also thank you giving me advice about my work and publishing a great textbook about BASE. The European Physics Journal textbook you wrote was very helpful to understand about BASE from scratch and also for writing my thesis. Dr Stefan Sellner also welcomed me kindly to BASE. By your advice about programming it was helpful to getting those knowledge. And by offering your homemade cakes, I was very glad to have a good time even at social life at CERN. I would also like to thank to Dr Hiroki Nagahama, one of the PhD student of Mastuda lab. You advised me any time when I asked about question about my thesis or even silly things. You also supported me for my thesis when I was in Japan. And your attitude towards physics, measurements and writing was a good role model for me. I would also like to thank to Mr Takashi Higuchi, also the PhD student of Matsuda lab. You kindly advised me about not only about the work, but also about how to live at France. I would like to thank to Mr James Harrington, the PhD student of BASE. You supported me for my experiment both with advices and LabVIEW programs. Also your great passion about physics and especially about Dirac equation were very impressive and stimulated me to study physics further. I would also like to thank to Mr Matthias Borchert, a master student of BASE. You didn't hesitate to helping my work and filling the liquid helium and nitrogen when I cannot help for that while I was writing my thesis.

I would like to thank again all the colleagues of BASE. I was working at BASE about a year, but it was the most precious time for me and influenced me to be enthusiastic towards physics. Finally I would like conclude the acknowledgement by thanking to my friends and family who supported and encouraged me for the entire master term.